2022

Multimodal Ultrasound Imaging for Improved Metastatic Lymph Node Detection

Sidhartha Jandhyala
Sidhartha.Jandhyala.TH@Dartmouth.edu

Multimodal Ultrasound Imaging for Improved Metastatic Lymph Node Detection

A Thesis
Submitted to the Faculty
in partial fulfillment of the requirements for the
degree of

Doctor of Philosophy

in

Engineering Sciences

by Sidhartha Jandhyala

Thayer School of Engineering
Guarini School of Graduate and Advanced Studies
Dartmouth College
Hanover, New Hampshire

April 2022

Examining Committee:

Chairman _____
Geoffrey Luke, PhD

Member _____
Kimberley Samkoe, PhD

Member _____
Jonathan Elliott, PhD

Member _____
Stanislav Emeilianov, PhD

_____
F. Jon Kull, Ph.D.
Dean of Guarini School of Graduate and Advanced Studies

ABSTRACT

Head and neck squamous cell carcinoma (HNSCC) is the sixth most common cancer worldwide and is complex in nature due to the variety of organs located in the head and neck region. Knowing the metastatic state of the lymph nodes is paramount in accurately staging and treating HNSCC patients. Currently, metastatic lymph node detection involves the use of magnetic resonance imaging and/or x-ray computed tomography, followed by biopsies for histological confirmation. The main diagnostic criteria is the size of the nodes; however, current imaging methods are not 100% accurate due natural lymph node variability. Ultrasound imaging is able to provide additional biological information in addition to lymph node size such as the hilus state, presence of necrosis and vascular information, but it is hindered by poor resolution and limited contrast. Augmenting ultrasound for metastatic lymph node detection has clinical potential due to the availability of ultrasound in the clinic, reduced radiation exposure and minimized patient morbidity. This thesis focuses on augmenting ultrasound with photoacoustic imaging or with nanoparticle contrast agents for improved detection of lymph node metastasis. First, the development of an ultrasound-photoacoustic (USPA) imaging system is described. The USPA system is capable of imaging blood oxygen saturation (sO_2), a promising criteria to differentiate between metastatic and healthy lymph nodes. To correct for tissue-dependent attenuation of light in tissue, a deep neural network was developed and trained using Monte-Carlo simulated and experimentally acquired photoacoustic data for better sO_2 predictions. Secondly, to improve ultrasound sensitivity to metastatic cells, molecularly targeted phase change perfluorohexane nanodroplets conjugated to epidermal growth factor receptor (EGFR) antibodies (PFHnD-Abs) were developed. It is shown that the PFHnD-Abs are able to specifically bind to HNSCC cells and improve the ultrasound contrast of the cells, opening the door to targeted metastatic lymph node detection. Lastly, to validate the use of the PFHnD-Abs *in-vivo*, a paired agent imaging approach was adopted by using using a perfluoropentane core nanodroplet (PFPnD) as a non-targeted imaging agent to enable multiplex ultrasound

imaging *in vivo*. Overall, this work expands the potential of ultrasound for metastatic lymph node detection.

Acknowledgements

I would like to take this opportunity to thank my advisor, Dr. Geoffrey Luke, for believing in me and guiding me through this journey. He created a great lab environment conducive to learning. I would like to thank my lab mates Dr. Austin Van Namen, Catalina Paula-Spatarelu, Dr. Tomas Jordan, Dr. Ruibo Shang and Kathy DiAntonio for their support with experiments, lab management and contributing to a great time in the lab.

I would like to specifically acknowledge Jason Gunn, Rendall Strawbridge, Dr. Phuong Vincent, Dr. Cheng Wang and Dr. Kimberly Samkoe for their help with animal work and lab practices. I would like to thank Dr. Aravindhan Sritharan for help with pathological analysis.

This would not have been possible without the support of my Mom, Dad, Sister, Guru and all of my friends that I have made here, thank you so much and I feel blessed to have made these lasting relationships.

Last but not least, I would like to dedicate this thesis to both of my grandmothers, Smt. Lakshmi Anasuya Jandhyala and Smt. Lalita Devi Kuchibhotla, both of whom I lost during my time here.

Contents

List of Figures

Chapter 1

Introduction, Background and Purpose

1.1 Importance of Lymph Nodes in Head and Neck Squamous Cell Carcinomas (HNSCCs)

Head and neck squamous cell carcinoma (HNSCCs) is the sixth most common cancer worldwide with 890,000 cases and 450,000 deaths in 2018 [1]. The incidence of HNSCC is projected to increase by 30% by 2030 [1]. HNSCCs can be derived from the mucosal epithelium of a variety of organs located in the head and neck region such as the oral cavity, nasopharynx, oropharynx, pharynx and larynx [1]. The causes of HNSCC have been correlated to tobacco use, alcohol consumption, environmental pollutants and viral infections, mainly human papillomavirus (HPV) and Epstein-Barr virus (EBV) [1]. Proper staging of the disease state is needed to accurate treatment and management of the cancer. The tumor, node and metastasis (TNM) staging system is used to determine the state of the cancer [2]. The tumor size or depth (T), the lymph node spread (N) and metastatic status (M) are used to predict survival, choose the initial treatment and attempt to standardize communication among healthcare providers and outcomes reporting [2]. While the TNM system is constantly being evolved to incorporate new criteria [3], the importance of nodal status has been constant.

The spread of head and neck cancer occurs in multiple ways. The first is direct growth from the primary site into adjacent areas, second is the spread through the lymphatic channels to the lymph nodes [4]. Another method of spread is through the bloodstream to distant sites in the body [4]. The spread of cancer to the lymph nodes in the neck is relatively common in head and neck cancer, highlighting the importance of determining the metastatic state of cervical lymph nodes. The accumulation of cancer cells in the lymph nodes indicates metastasis. The lymph system is a part of the immune system and is intended to fight and kill the cells, indicating that the metastatic cells that accumulate in the lymph nodes have mutated, are resistant and have overcome the immune defenses [5]. Thus, the presence of metastatic cells in the lymph nodes is an early predictor of survival outcomes. Determining nodal metastases is performed by medical imaging or biopsy and histology, the latter leading to higher patient morbidity.

Specific tumor biomarkers have been identified that promote proliferation of HNSCCs. Human papilloma virus (HPV) has shown to induce HNSCCs which is a biologically distinct disease compared to HPV negative tumors [6]. It has been shown that HPV induced HNSCC has a better prognosis and treatment than HPV negative HNSCCs [6]. P16 overexpression has been used as a surrogate clinical biomarker to determine if the tumor is HPV induced [6]. Epidermal growth factor receptor (EGFR), a cell surface membrane receptor, is over-expressed in 90% HNSCCs, which corresponds to tumor growth and therapy resistance [7]. The EGF ligand has shown to activate a multitude of signal transduction pathways, which has led to drive cell proliferation and resist apoptosis [8]. Cetuximab, a monoclonal anti-EGFR antibody, is the first FDA approved molecular agent widely used clinically and has shown improvement in survival rates with patients exposed to combined antibody and radiotherapy [7]. The use of antibodies to bind to EGFR has shown downregulation of the signaling pathways, promoting cell apoptosis [8].

The current standard of care in clinical practice for HNSCCs depends on the location of the tumor. Treatment strategies are dependent on accurate staging of the tumors, which

involved determining if the tumor has metastasized. Initial screening involves the use of magnetic resonance imaging (MRI) and/or x-ray computed tomography (CT) to determine the extent of the primary tumor [9, 10]. For early stage tumors (stage I and II), single modality treatment with surgery or radiation therapy (RT) is used to remove the primary for approximately 30%-40% of patients [10]. Later stage tumors are often treated with a combination of RT and chemotherapy. The results of surgery and RT as single modalities have been similar, however the choice of modality is dependent on the location of the tumor. Combined therapy has been recommended for 60% of patients with local or regionally advanced diagnosis [10]. Determining the metastatic state of cervical lymph nodes is crucial to determining the stage of the tumor and ultimately the prognosis of the disease. Imaging is used first to locate the lymph nodes followed by biopsies to allow for histological assessment of the tissue. However, biopsies are limited to a certain subsection of the node and is an invasive procedure, leading to patient morbidity. In contrast, improvements in current imaging modalities have been advantageous due to their non-invasive nature and ability to image the whole node, however each imaging modality has an array of limitations. Through the use of new imaging techniques, the sensitivity and specificity of detecting metastatic lymph nodes has been improving, with the ultimate goal of alleviating the need for lymph node biopsies.

1.2 Imaging of lymph nodes

The detection and confirmation of metastatic lymph nodes includes the use of different imaging modalities such as CT, MRI, fludeoxyglucose positron emission tomography (FDG-PET), ultrasound, fluorescence and photoacoustic imaging. However, none of the imaging modalities have shown to be 100% accurate, indicating the need for better methods [11]. MRI and CT rely on the lymph node size and shape to identify malignant lymph nodes, while ultrasound is able to provide size and shape information in addition to inner nodal

criteria such as the hilus state, presence of necrosis, and vascular information with the use of Doppler [12]. FDG-PET measures the metabolic activity of lymph nodes to determine the metastatic state. By relying predominantly on size, MRI and CT still face challenges in determining borderline metastatic lymph nodes and nodes harboring micro-metastases, explaining the decreased specificity and sensitivity compared to ultrasound [12]. Advances in camera systems and better understanding of cancer biology has allowed for targeted fluorescence imaging using fluorescent tagged bio-markers [13]. With recent advances in imaging, FDG-PET/CT has been regarded as the main method of imaging lymph nodes during tumor staging due to the high anatomical accuracy from CT and the metabolic activity from PET. [10, 14]. However, the potential drawbacks of FDG-PET/CT include limited resolution and partial volume effects resulting in inaccurate diagnosis of small lymph nodes [14]. Benign lymphadenopathy also results in metabolism similar to metastatic lymph nodes leading false positives[14]. Interestingly, the inflammatory response to the COVID-19 vaccine has shown similar lymph node metabolism comparable to metastatic lymph nodes, indicating a need for a secondary confirmation [15]. The use of ultrasound as a secondary confirmation modality has been shown to improve detection efficiency [14]. Ultrasound is able to detect nodal features invisible to PET/CT such as necrosis, an automatic indicator of metastasis [14, 12]. Improving ultrasound for lymph node detection has many advantages mainly zero exposure to ionizing radiation, widespread clinical availability and cost effectiveness.

1.2.1 Ultrasound detection of metastatic lymph nodes

Ultrasound has been shown to have a better sensitivity and specificity than MRI and CT [12, 16, 17]. The use of ultrasound in assessing lymph nodes for metastasis has been well established due to the increased feature information compared to other modalities and the enhanced clinical availability. Additionally, ultrasound can be used to acquire two times of images, grayscale and Doppler, each providing different assessment criteria. Grayscale ultrasound provides spatial, size, shape, border and internal node information (echogencity,

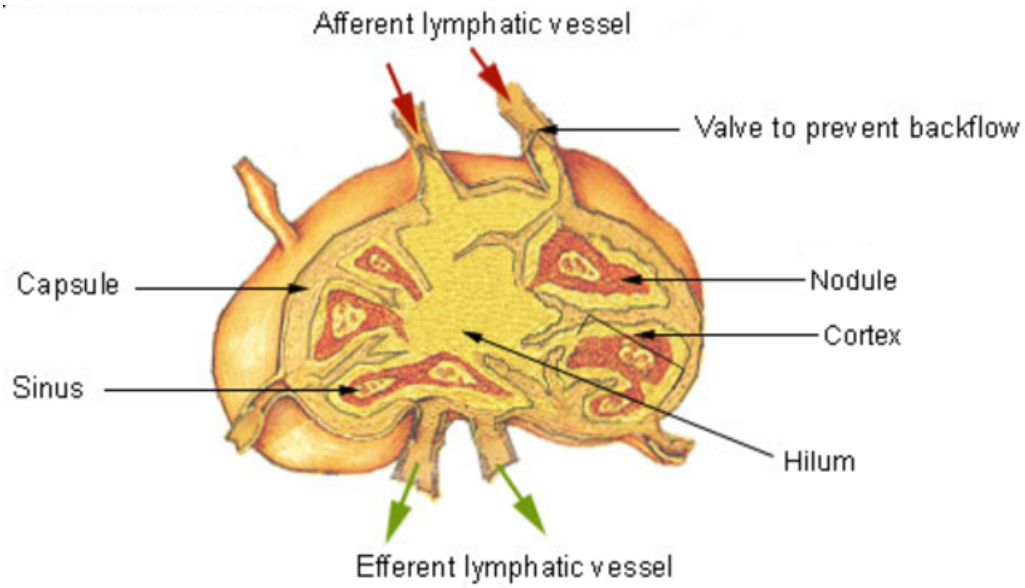

Figure 1.1: a) Schematic of a healthy lymph node. The echogenocity of the hilum is reduced in metastatic lymph nodes [16].

echogenic hilus, calcification and necrosis) [16]. Doppler can be used to determine the vascular patterns of lymph nodes [16].

The size, shape and border are external factors used to identify metastatic lymph nodes from benign nodes. Typically, the size of metastatic nodes are larger than benign nodes with the size threshold criteria ranging from greater than 5-10 mm [16]. The shape of metastatic nodes tend to be more round with the short to long (S/L) ratio greater than 0.5, where benign nodes are more elliptical in shape with a S/L ratio less that 0.5 [16]. This ratio is easy to measure because the border of metastatic lymph nodes tend to be sharp due to the intranodal tumor acoustic impedance mismatch compared to the surrounding tissue [16].

Internal factors used to assess nodal metastasis include intranodal necrosis, calcification, echogenic state of the hilus and vascular distribution. Metastatic lymph nodes typically do not show any echogencity in the hilus, compared to benign nodes of the same size [16, 18]. The presence of necrosis should be considered metastatic [16, 19]. Calcification found in the nodes also indicates metastasis, but mainly has been shown to be related to

thyroid cancer specifically [16]. The vascular distribution within the node can be assessed using Doppler ultrasound. Normal lymph nodes with a diameter greater than 5 mm will display hilar vascularity within the node [16]. Metastatic lymph nodes display peripheral vasculature due to the tumor cells inducing angiogenesis, recruiting new vessels [16].

The use of grayscale and Doppler ultrasound provide information on different lymph node characteristics to determine metastatic state. The specificity and sensitivity of ultrasound have shown to be better than MRI and CT [17, 12]. However, one of the major limitations of ultrasound is the dependence on the sonographer. Compared to MRI and CT which are much more standardized and reduce inter-observer variation, ultrasound is a hand-held live imaging modality where sonographer experience introduces inter-observer variation [12, 20]. Additionally, ultrasound is limited to superficial structures, as it faces attenuation deeper in tissue [20]. The augmentation of ultrasound through the use of hybrid imaging modalities and contrast agents to overcome these limitations is needed to improve the specificity (ranging from 67-97% [12]) and sensitivity (ranging from 74-100% [12]) of the imaging modality.

1.2.2 Fluorescence imaging

The advances in camera technology and deeper understanding of cancer biology and biomarkers enabled fluorescence imaging in head and neck cancer imaging [13]. The optimal wavelengths for fluorescent dyes used in fluorescence imaging are in the near-infrared (NIR) spectrum (650-1350 nm), which allows for deeper light penetration several millimeters deep compared to hundreds of micrometers for other wavelengths [21]. Fluorescent imaging is also a real-time modality, making it attractive for surgical guidance and detection of tumor margins [22], with many contrast agents currently undergoing clinical trials [23]. Fluorescent dyes are conjugated to molecular targeting antibodies or affibodies designed to target molecules over-expressed in tumor cells, like EGFR. The molecular targeting allows for precision imaging by selectively illuminating tumor cells. While the real-time imag-

ing and precise targeting are major advantages, depth penetration is a hindrance from wide adoption. Fluorescence imaging has been widely adopted in surgical guidance due the tissue already being exposed, removing the depth penetration constraint. Clinical lymph node imaging has been limited to *ex-vivo* applications, mainly to augment pathological assessment [23].

1.2.3 Photoacoustic imaging

Photoacoustic imaging (PAI) is a hybrid imaging modality that combines the use of fluorescence imaging with ultrasound imaging. Photoacoustic imaging works by transmitting pulsed light (e.g., a nanosecond laser or light emitting diode (LED)) into tissue which is absorbed by chromophores . The absorption process generates localized heating, generating an ultrasound pressure wave that can be detected using a conventional B-mode ultrasound transducer. The image is formed using the time-of-flight of the acoustic wave, much like grayscale ultrasound. Photoacoustic images provide information on the optical properties of tissue, specifically optical absorption, while pure ultrasound images provide the mechanical properties of tissue [24]. The pressure distribution produced upon deposition of optical energy can be correlated to the absorbed optical energy distribution given the optical absorption and scattering properties of the tissue [24]. The core advantages of photoacoustic imaging are its high spatial and temporal resolution, clinically sufficient imaging depths, the ability to image both endogenous and exogenous contrast agents and zero ionizing radiation exposure [25].

Photoacoustic imaging typically use optical wavelengths in the NIR range (650 - 1350 nm) which allows for the deepest depth penetration up to a 5 cm [26, 25, 24]. Imaging in the NIR window allows for spectroscopic photoacoustic imaging (sPA), which exploits the temporal resolution of PAI and the NIR window by transmitting multiple wavelengths of light into the tissue to create a spatial map of the absorption spectra within the tissue. This allows for the ability image endogenous chromophores such as hemoglobin, lipids, water,

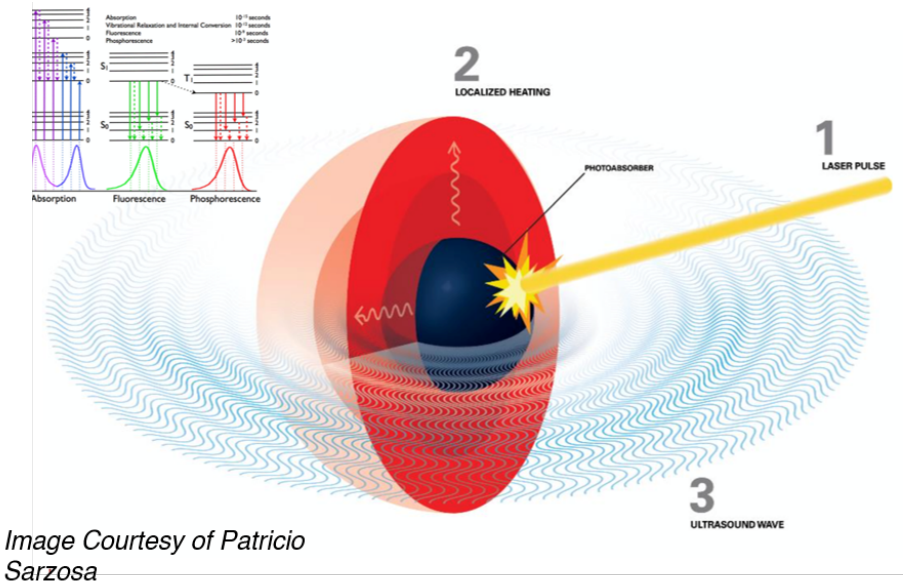

Figure 1.2: Photoacoustic imaging uses light to excite tissue which results in a acoustic pressure wave that can be read by an ultrasound transducer. The laser pulse excites a photoabosorber which causes thermoelastic expansion of the tissue resulting in the ultrasound wave. Image courtesy of Patricio Sarzosa.

melanin in addition to exogenous chromophores like small molecule dyes and nanoparticles with greater depth penetration than traditional optical imaging [24]. By knowing the absorption properties of the different chromophores, spectral analysis can be performed to quantify the concentration of the various chromophores within in the tissue. One major application where this has been used is to quantify blood oxygenation (sO_2) by exploiting the difference in optical absorption spectra between oxyhemoglobin and de-oxyhemoglobin. Blood oxygen imaging provides information on the physiological state of the tissue and has shown to be able to identify tumor hypoxia [27] and differences between metastatic and benign lymph nodes [28] without the use of external contrast agents.

The hypoxic status of the primary tumor has shown to be an indicator of lymph node metastasis [29]. Blood oxygenation imaging using PAI has shown to be able to differentiate between metastatic and benign lymph nodes [28]. The overall blood oxygen saturation of tissue can be computed by taking the ratio between the concentration of hemoglobin and de-oxyhemoglobin in the tissue, requiring no external contrast agents. The measurements

therefore are receptive of functional changes in the node compared to molecular changes [28]. The sO_2 within metastatic lymph nodes is shown to be lower than benign nodes due to the increased metabolic activity from cells in the region responding to the metastatic invasion [28]. Tumor hypoxia is another factor that explains the decrease in sO_2 compared to benign nodes. Photoacoustic imaging can be further augmented through the use of exogenous contrast agents such as fluorescent dyes, plasmonic nanodroplets and multi-modal contrast agents [30] which will be discussed in the subsequent sections.

A major limitation of PAI is depth penetration due to light attenuation into tissue. Beyond the first millimeter in tissue, light is attenuated by a factor of 4 for each subsequent centimeter of penetration depth [24]. This leads to lower ultrasound signals, requiring low frequency transducers to capture the low signals, compromising on image quality. Strategic use of photosensitizers and choice of transducers can optimize the depth penetration limitation. Another major limiting factor is spectral coloring, where the optical absorption and scattering of tissue changes the fluence leading to inaccurate photoacoustic signals [31, 32]. To correct for the spectral coloring, deep learning methods have been explored showing promise to correctly estimate sO_2 [33, 34].

1.3 Imaging Contrast Agents

The use of imaging contrast agents augments the different imaging modalities. Contrast agents help generate more contrast that is detectable by the imaging modality, but can further be tuned to serve a functional purpose such as molecular targeting and imaging. Contrast enhanced ultrasound (CEUS) has been explored to enhance the functionality of ultrasound through the use of microbubbles or nanodroplets for vasculature and molecular imaging [35]. The contrast is achieved due to the acoustic impedance mismatch between the gas in the core of the agent and the surrounding tissue. Some of the contrast agents developed can also serve as multi-modal contrast agents in conjunction with photoacoustic

or fluorescence imaging. Currently, microbubbles have been approved by the FDA for ultrasound imaging [36].

1.3.1 Microbubbles

Contrast microbubbles are gas filled with a diameter between 1-10 μm. The core of the microbubble is typically a perfluorinated gas mixed with air, encapsulated in a shell made of proteins, polymers, lipids or surfactants [35]. The perfluorinated core is poorly soluble in water and oppose the *in-vivo* Bernoulli forces from blood vessels, keeping the microbubble intact *in-vivo* [35]. The microbubbles are injected into either the bloodstream or lymphatics through a small bolus or infusion. Their micrometer size allows them to circulate through the vasculature, enabling vasculature imaging. The interaction between the ultrasound wave and the compressible gas core results in an unique nonlinear oscillation pattern, leading to further enhanced contrast [37]. In addition to oscillation, interaction with ultrasound waves can also lead to microbubble steering, gas dissolution and vasculature/membrane disruption through micro streaming of the fluid around the microbubble [38]. Disruption of the vasculature using microbubbles has ultrasound triggered drug delivery [38]. The use of microbubbles with ultrasound have shown higher sensitivity of detecting hypo- or hyper-vascularity compared to Doppler [37].

Microbubbles have been used in a variety of applications such as vasculature imaging, molecular targeting [35], targeted drug delivery [39], therapeutic gas delivery [40], and lymph node imaging [37]. While microbubbles have shown promise in vasculature imaging, microbubble mediated delivery in tumors has been limited mainly due to the inability to perfuse into the micro-vasculature in tumors due to their size. The size cutoff of tumor vasculature pores ranges from 380 - 780 nm, while some expand up to 2 μm [41]. Additionally, microbubbles experience short circulation times on the order of minutes [42], limiting their *in-vivo* application. The use of microbubbles has shown to be able to improve metastatic lymph node detection compared to conventional ultrasound [37], but the overall

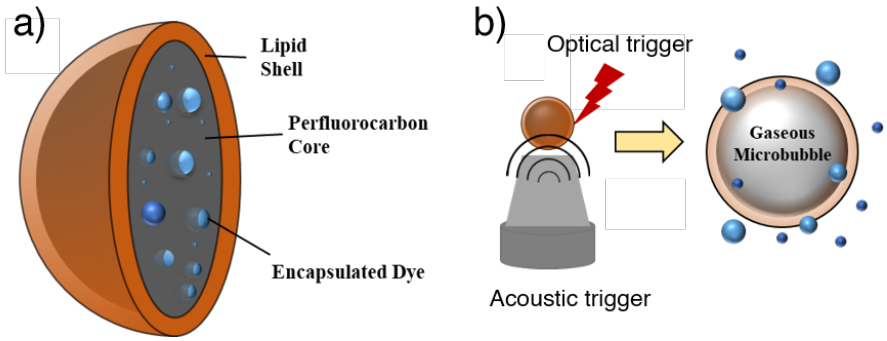

Figure 1.3: a) Schematic of the perfluorocarbon nanodroplets. The core of the nanodroplet contains a liquid perfluorocarbon core, encapsulated by a lipid shell. A fluorescent dye can be embedded into the core of the nanodroplet for optical activation. b) the liquid nanodroplet can be activated either with an optical or acoustic trigger to initiate the liquid to gas phase transition. The gaseous microbubble is what produces the contrast in the ultrasound images.

tumor penetration and ability to detect micro-metastasis still requires improvement.

1.3.2 Nanodroplets

To address the major size limitation of microbubbles, nanodroplets have been explored as contrast agents due to their ability to better perfuse into the tumor microenvironment through the enhanced permeability and retention (EPR) effect [41]. Tumor tissue is associated with poor vascularization, leading to irregular blood flow and leaky vasculature. Smaller sized contrast agents have a greater chance of accumulating into the tissue. Many nanoparticles have been developed for a variety of applications, but phase change nanodroplets are a particular class that have been heavily explored as ultrasound contrast agents. Phase change nanodroplets employ a perfluorocarbon core encapsulated in a lipid, polymer or protein shell. The stabilizing shell keeps the nanodroplet in the liquid phase due to the high Laplace pressure acting on the core of the nanodroplet [43].

The perfluorocarbon core is attractive because of their low boiling points. Upon exposure to either acoustic or optical energy, the low boiling point liquid droplet vaporizes into a gaseous microbubble. In the stable liquid droplet state, there is no visible ultrasound

contrast, however when the core undergoes the vaporization event, the resulting microbubble produces the ultrasound contrast. Nanodroplet circulation is longer than microbubbles, due to their size and use of polyethylene oxide chains to avoid recognition by the reticulo-endothelial system and blood proteins involved in clearance [43]. Phase change nanodroplets have been developed for a variety of different applications such as gene and drug delivery [43], penetrating the blood brain barrier[44, 45], and super resolution imaging [46] to name a few. By incorporating fluorescent dyes within the nanodroplet, phase change nanodroplets have been used as multi-modal imaging agents for photoacoustic and ultrasound imaging. Indocyanine green (ICG) is an FDA approved photosensitizer with an excitation wavelength in the NIR spectrum that has been explored as a photosensitizer for photoacoustic imaging and photodynamic therapy [47, 48]. The use of an optical stimulus such as a nanosecond pulsed laser tuned to the excitation wavelength of the embedded dye can cause the same vaporization effect, leading to ultrasound contrast [47]. While the use of small molecule dyes in the nanodroplet allows for tunable wavelength selection, the depth penetration is limited by the attenuation of light in tissue. Phase change nanodroplets activated by an ultrasound stimulus, known as acoustic droplet vaporization (ADV), has better depth penetration and has open doors to better *in-vivo* imaging.

1.4 Aims for Thesis

1.4.1 Aim 1: Development of a combined ultrasound and photoacoustic imaging system

The first aim of this thesis is to develop an ultrasound-photoacoustic (USPA) imaging system that is capable of imaging blood oxygen and photoacoustic contrast agents. The system used a Verasonics Vantage 256 high frequency research ultrasound system combined with a near infrared nano-second pulsed tunable laser. The blood oxygenation measurements were characterized using cow blood phantoms, modulating the amount of oxygen in the

blood by mixing it with carbon dioxide. In an effort to correct for spectral coloring, an accompanying deep learning model was developed to accurately estimate sO_2 from Monte Carlo simulations and experimental photoacoustic images.

1.4.2 Aim 2: Synthesis of tumor biomarker targeted ultrasound phase change nanodroplets for molecular imaging and improved contrast

The second aim of this thesis is to fabricate, functionalize and characterize molecularly targeted perfluorocarbon (PFC) phase change nanodroplets conjugated to anti-EGFR antibodies (PFCnD-Ab). EGFR was chosen as the target due to its over-expression in head and neck squamous cells carcinoma (HNSCC) cells. The PFCnD-Abs do not emit any ultrasound contrast in the inherent liquid state. Upon activation with an acoustic or optical trigger, the PFC core expands from a liquid droplet to a gaseous microbubble, producing the ultrasound contrast. The choice of perfluorocarbon core can also induce recondensation and reactivation, leading to a blinking effect. This section will explore the fabrication, robustness and targeting efficiency of the PFCnD-Abs using cells, phantoms and *in-vitro* studies.

1.4.3 Aim 3: Paired agent imaging approach using ultrasound phase change nanodroplets for multiplexing

The third aim of this thesis is to expand the second aim by introducing multiplexing imaging using different PFCnD contrast agents together. In this section, two different PFCnDs with different cores, perfluorohexane (boiling point 56°C) and perfluoropentane (boiling point 29°C) each with their own fluorescent dye are imaged together using a custom high intensity focused ultrasound (HIFU) imaging setup. The perfluorohexane core nanodroplet surface is functionalized with anti-EGFR antibodies for molecular targeting, while the per-

fluoropentane nanodroplet surface is not functionalized and serves as a non targeting control. Each nanodroplet has a different fluorescent dye embedded to allow for paired agent imaging and targeting validation. Paired agent imaging allows for a ratiometric direct comparison between the two nanodroplets to validate the targeting efficiency using fluorescence, since both particles are experience the same flow kinetics *in-vivo*. The custom developed HIFU imaging system was used to differentiate between the PFH and PFP ultrasound signals, based off the repeatable blinking effect of the PFH particles and the one time activation of the PFP particles. The ability to differentiate between the two nanodroplets was performed and compared using fluorescence and ultrasound *in-vivo*.

Chapter 2

Ultrasound-Photoacoustic (USPA) System Development

2.1 Introduction and Background

Photoacoustic imaging (PAI) is a hybrid imaging modality that uses light to excite tissue and measures the optically induced ultrasound signals. The conversion of light to sound is known as the photoacoustic effect and was discovered by Alexander Graham Bell in 1880 [49]. Ultrasound images provide information about the elastic and mechanical properties of tissue, whereas photoacoustic images provide information about the optical properties within the tissue [24]. When tissue is exposed to nanosecond, high energy pulses of light, it causes thermoelastic expansion within the tissue due to the optical absorption of the light. The thermoelastic expansion results in transient broadband ultrasound waves which can be detected by an conventional ultrasound transducer to form an image [50]. A prominent feature of PAI is the ability to distinguish tissue components such as hemoglobin, melanin, water, and lipids to name a few, each having a different absorption profile within tissue (Figure 2.1). Since light propagation is only used to excite the tissue and not used in generating the image, PAI can penetrate tissue deeper than traditional optical imaging [50].

Additionally, ultrasound scattering in tissue is 2-3 magnitudes lower than optical scattering in tissue, allowing for deeper penetration and higher spatial resolution [50]. PAI has the potential to clinically augment ultrasound imaging, specifically in cancer imaging.

2.1.1 Basic Principles of Photoacoustic Imaging

The photoacoustic effect is the generation of sound from the absorption of light. The light energy is absorbed by endogenous photoabsorbers (e.g., hemoglobin or melanin) converting it to heat. The heat then causes the tissue to thermoelastically expand, generating acoustic waves detectable by conventional ultrasound transducers.[30]. The maximum initial pressure P_{o} from the photoabsorber is correlated to the absorbance coefficient of the absorber. The relationship is described in the following equation:

$$P_{\mathrm{o}} = \Gamma \mu_{\mathrm{a}} F \tag{2.1}$$

where Γ is the tissue's Grüneisen parameter [30], μ_{a} is the absorbance coefficient of the photoabsorber and F is the fluence of light at the photoabsorber. The more light that can be delivered into the tissue, the stronger the resulting acoustic wave. The absorbance coefficient is a wavelength dependent constant for the photoabsorber. The Grüneisen parameter is constant relating to the thermal expansion of tissue and and is defined as

$$\Gamma = \beta/(\kappa \rho C_{\mathrm{p}}) \tag{2.2}$$

where β is the isobaric volume coefficient, C_{p} is the specific heat κ is the isothermal compressibility and ρ is the mass density [51]. It is important to note that the P_{o} values are an approximation due to tissue heterogeneity and light attenuation, which occurs as both the optical and acoustic energy travel through the tissue [30].

A biomedical PAI system typically contains a tunable near-infrared (NIR) laser with a pulse width < 10 ns, a fluence of 20 - 100 mJ/cm^2 at 700 - 1,100 nm, and a pulse repeti-

tion frequency (PRF) between 10 and 50 Hz [50]. Optical wavelengths in the NIR window allow for the deepest penetration of light due to low optical absorption within the tissue. Higher fluence and shorter pulse widths enhance the photoacoustic effect and enable deeper penetration. However, imaging depth and spatial resolution are direct trade-offs [50]. Photoacoustic imaging relies on the light penetrating into the tissue, but light diffuses in tissue past a depth of 1 mm [30]. Assuming uniform diffusion, the spatial resolution is dependent on the ultrasound transducer parameters. The axial resolution is inversely related to the bandwidth of the transducer. Higher bandwidth and center frequency transducers produce higher resolution images, but at the cost of imaging depth; higher frequency acoustic waves are more quickly attenuated in tissue [52]. For comparison, a 50 MHz and a 5 MHz transducer have a typical axial resolution of 15 and 150 μm and a lateral resolution of 50 and 300 μm resolution, respectively [30]. The lateral resolution is dependent on the number of elements in the array, shorter linear arrays have lower resolution. Wavelength selection is also important in determining the imaging depth [53].

2.1.2 Spectroscopic photoacoustic imaging

Spectroscopic photoacoustic (sPA) imaging is performed by using multiple wavelengths to excite the tissue and unmixing the resulting PA signals for each wavelength. Thus, the concentrations of the different optical absorbers within the tissue can be determined. The selection of wavelengths is important, ideally a large number of wavelengths spanning a broad spectrum should be used. However in practice, the number of wavelengths used is limited by the spectral range of the laser, the line width of the laser, the PRF and the light attenuation of the tissue being imaged [53]. The concentrations of the different absorbers are determined by treating each pixel as a combination of different intensities from each absorber based on their absorption coefficient at each individual wavelength [53]. Figure 2.1 shows the absorption profiles of different absorbers in tissue, including oxyhemoglobin, deoxyhemoglobin, melanin, water and fat, based on data produced from the Oregon Med-

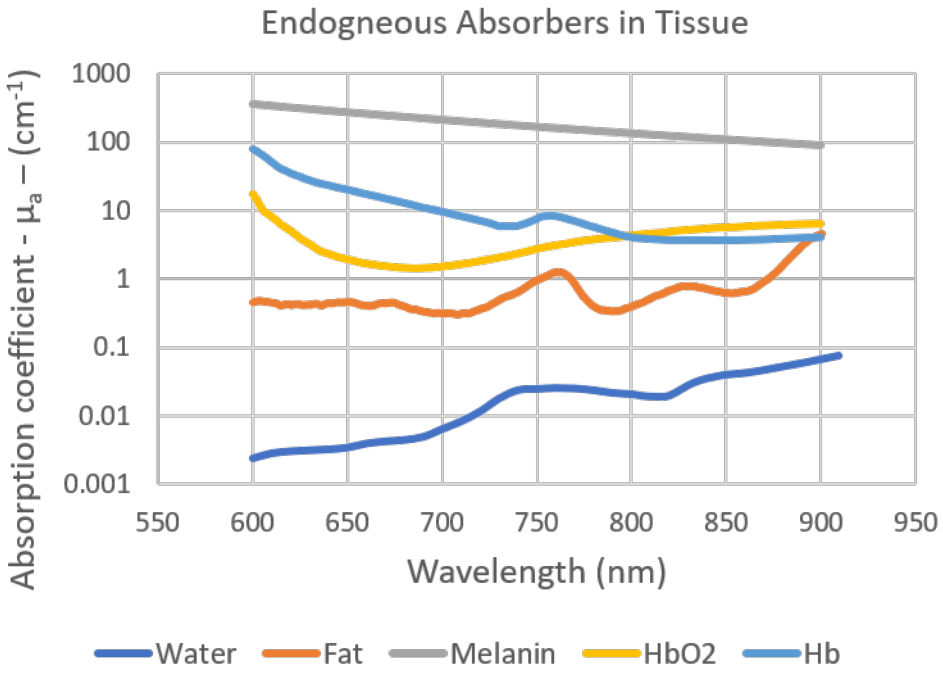

Figure 2.1: The endogenous chromophores in tissue each have different absorption profiles with respect to wavelengths. In particular, the difference the in the absorption between hemoglobin (HbO_2) and deoxyhemoglobin (HbR) within the optical window (650 - 900 nm) allows for spectroscopic photoacoustic imaging to determine blood oxygenation using spectral unmixing [54].

ical Laser Center. Two main applications of sPA are blood oxygenation and nanoparticle deposition in tissue [53].

2.1.3 Blood oxygenation imaging using photoacoustic imaging

Hemoglobin is the absorbing molecule in blood. Its optical spectrum changes based on whether it carries an oxygen molecule or not, denoted oxyhemoglobin and deoxyhemoglobin, respectively. Normal arterial blood oxygen levels range between 95% - 100%, while venous blood lies in the 60% - 80% range [54]. Fast growing tumors have a high oxygen consumption rate leading to the creation of new blood vessel networks (a process known as angiogenesis) [54]. The irregular blood vessel network results to interrupted blood flow, irregular vascular path, and leaky vessel walls leading to a heterogeneous oxygen distribu-

tion within the tumor [54]. With the rapid growth of blood vessels, tumors tend to have hypoxic cores due to the irregular growth [54], which leads to an overall decrease in blood oxygenation within tumors [54]. The use of sPA imaging can estimate the concentrations of hemoglobin and deoxyhemoglobin to determine the sO_2. Within the 600-900 nm range, both deoxyhemoglobin (Hb) and hemoglobin (HbO_2) have an optical absorption coefficient that is at least one order of magnitude higher than other endogenous chromophores, such as lipids and water [54]. Luke et. al have shown that it is possible to differentiate between healthy and metastatic lymph nodes using photoacoustic blood oxygen saturation [28]. The metastatic lymph node displayed a lower sO_2 throughout the whole lymph node compared to healthy nodes [30], indicating that it could be a possible biomarker for the spread of the disease.

2.1.4 Exogenous contrast agents for photoacoustic imaging

Spectroscopic photoacoustic imaging can also be used to image contrast agents in tissue. Dyes, plasmonic nanoparticles, phase changing nanoparticles have been used to enhance the imaging contrast while also providing molecular information [2]. To maximize the exogenous contrast, the optical absorption of the contrast agent should be within the optical window (600-1100 nm) where the absorption of tissue is lowest [30]. Contrast agents should have a signaling compound that absorbs the optical energy such as a dye, metallic or semi-metallic nanostructure or an organic nanostructure [55] along with a targeting moiety for a specific biological process or entity such as antibodies, affibodies, aptamers, small molecules or peptides [55]. The signaling compound can either be directly conjugated to the targeting compound or encapsulated within a nanostructure with the targeting compound on the surface [55].

Different nanoparticles with different conjugation strategies have been developed for photoacoustic imaging. There are many biocompatible dyes within the optical window, such as indocyanine green (ICG), AlexaFluor 750, IRDye 800CW, and methylene blue

that have been commonly used [30]. The dyes are small molecules on the order of one nanometer, allowing quick clearance through the body [30]. Lower quantum yield dyes lead to higher PA signal generation because less of the absorbed energy is emitted [30].

Plasmonic nanoparticles use noble metals like gold or silver and rely on the surface plasmon resonance (SPR) effect, which occurs when the surface free charges on the metal oscillate due to the electromagnetic field resulting in optical absorption five times greater than small molecule dyes [30]. The resonant frequency is shape and size dependent, allowing for wavelength tunability and application flexibility [30]. Different shapes such as nanospheres, nanorods, nanostars, nanoplates and nanocages have been developed for photoacoustic imaging [30]. The surface can also be easily modified to conjugate to other molecules. Poly(ethylene glycol) (PEG) molecules have been conjugated to the surface to increase circulation time and biocompatibility [56]. While plasmonic nanoparticles are tunable and versatile, the use of noble metals is a clearance and safety concern.

Perfluorocarbon phase change nanodroplets (PFCnDs) have also been used in photoacoustic imaging applications which produce contrast in both ultrasound and photoacoustic images, leading to multi-modal capabilities [57]. Optical absorbers are incorporated into PFCnDs to allow for optical excitation. ICG has been used with PFCnDs due to its amphiphilic properties, allowing it to be embedded into the particle [47]. The choice of PFC core allows for tunability, with lower bowling point PFCs requiring less energy to induce the phase change [58]. The use of higher boiling point PFCs, such as perfluorohexane which has a boiling point of 56°C, allows for repeated vaporization which has allowed for tumor imaging and super-resolution imaging [58, 46, 59]. PFCnDs also have been used in photoacoustic imaging of lymph nodes [60, 59].

Photoacoustic imaging has allowed for ultrasound based imaging of lymph nodes using label free methods [28] and exogenous contrast agents [60]. In this chapter, we set to develop a USPA system capable of imaging blood oxygen saturation using endogenous contrast with the potential to also work with exogenous contrast agents for non-invasive

metastatic lymph node detection. This chapter discusses the system design considerations, characterization of the system, acquired experimental results and future directions.

2.2 Materials and Design Considerations

The ultrasound-photoacoustic (USPA) imaging system has two main components: a nanosecond pulsed laser and an ultrasound imaging system. The laser is used as the signal generating energy source, while the ultrasound imaging system is used as the recording and image acquisition device. When it comes to lasers, there is a trade-off between laser energy and pulse repetition frequency. The more energy being emitted, the slower the pulse repetition frequency, resulting in a trade-off between imaging depth and frame rate. Light attenuates in tissue as it propagates deeper into tissue, meaning that in order to image deeper structures, high energy light needs to be emitted into the tissue.

The developed USPA system simultaneously acquires both ultrasound and photoacoustic images, but comes at a trade-off. Each channel in the ultrasound transducer needs to be able to both send and receive radio frequency signals. By simultaneously imaging both the ultrasound and photoacoustic images, there is a division of allocated transducer elements for the ultrasound and photoacoustic images. This leads to a trade off in PA signal strength, which is typically low to start off with. However, the added value of capturing the ultrasound image is that there is an anatomical reference which serves as the basis. The photoacoustic image can be overlaid on the ultrasound image highlight both the elastic and optical properties of the tissue. This is useful from a clinical translatability standpoint, clinicians have training using ultrasound to identify structures in tissues which may lead to better adoption of this technology.

2.2.1 Nanosecond Pulsed Laser

The USPA system was developed with the intent of imaging deep structures, characterized here as 2-3 cm below the surface. The nanosecond pulsed laser chosen for the system was the Phocus Mobile HE (Opotek) which has a low pulse frequency (10 Hz) and a high pulse energy (80 - 100 mJ/pulse). The higher pulse energy satisfies the design requirement to image deep structures. The laser is tunable and consists of a 1064-nm Nd:YaG pump laser, second harmonic generator, and optical parametric oscillator to achieve a tunable spectral range from 690 to 950 nm. The optical range is in the near infrared (NIR) regime, which allows imaging of endogenous chromophores such as hemoglobin and deoxyhemoglobin. The laser has an optical fiber bundle which is used to transmit the light into tissue. A custom hand-held transducer that combines the ultrasound transducer and a custom fiber optic bundle (CeramOptec, Bonn, Germany) was developed and will be explained in further detail below.

2.2.2 Ultrasound Imaging System

The second important component of the system is the ultrasound imaging system. A Verasonics Vantage 256 ultrasound system was chosen to acquire the PA signals, and form the image. The Vantage is widely used in research because of its programmable customizability and easy integration with the Phocus laser. The imaging system is connected to a PC computer, which handles the image formation.

The ultrasound transducer is another key design element in the system and is dependent on the application being pursued. Two transducers, a 7-MHz, 128-element linear array transducer (L11-4v, Verasonics) and a 15 MHz, 256 element linear array (L22-8v CMUT, Kolo Medical) were chosen because of their reasonable frequency range for a variety of clinical ultrasound imaging applications. Their bandwidths are appropriate for receiving the weaker broadband PA signals.

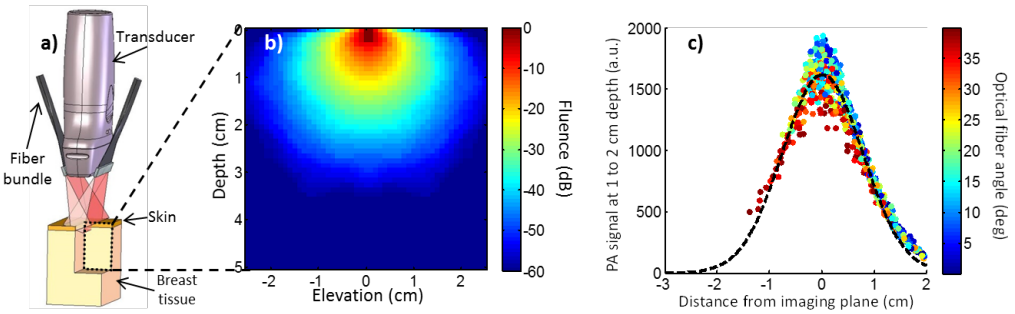

Figure 2.2: a) Schematic of the transducer and fiber bundle aligned to project the light onto the surface of the skin. b) Monte Carlo simulation of elevation vs depth and fluence. c) the fiber bundle angle was determined based on the distance from the imaging plane vs the PA signal intensity and the optical fiber angle.

2.2.3 Handheld Ultrasound Transducer

Photoacoustic imaging relies on light being delivered to the imaging plane on the skin surface. An ideal case would have the ultrasound transducer and laser aligned co-linearly; however, this is not possible due to the thickness of the ultrasound transducer. The design used flat optical fiber bundles oriented off-axis to the ultrasound transducer at an angle. The angle off-axis was determined through Monte Carlo simulations of light into tissue. Relatively uniform distribution of light into the tissue can be achieved by having optical fiber bundles running alongside of the transducer.

Custom 3D printer parts were used to create the necessary housing to assemble the handheld transducer. The optical fiber bundles were carefully glued to a 3D printed flap that would easily slide into the main ultrasound transducer standoff. The standoff was filled with a tissue mimicking polyacrylamide phantom with a thin layer of titanium dioxide mixed with gelatin. The titanium dioxide blocks back scattering of light, protecting the ultrasound transducer from damage and noise. Ultrasound gel is used to generate good contact between the transducer and transducer standoff.

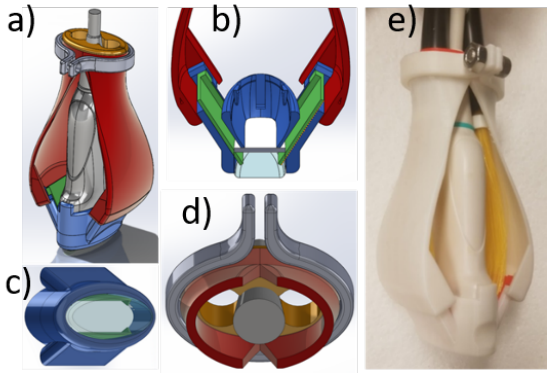

Figure 2.3: Schematics of the hand-held transducer and offset. a) schematic of the whole assembly developed in SolidWorks (Dassault Systems). b) the green flaps are attached to the optical fiber bundles. The red supports allow for handheld operation. c) the blue offset is filled with tissue-mimicking material and allows for the light to reach the surface of the skin in the ultrasound plane. d) the cable housing. e) image of the fully assembled transducer.

2.3 Preliminary Results and Discussion

2.3.1 Point Spread Function

To first characterize the system, we measured the point spread function (PSF) by sending the signal from each element in a 64x64 pixel field of view with a mechanical pencil lead (0.5 mm) in the center of the FOV. The image was produced using the back-projection method. The maximum pixel intensity point was selected to analyze the point spread function. The pixel intensities of the row containing the max intensity pixel was used to measure the lateral full width half max (FWHM), 0.8 mm. The column of the max intensity pixel was used to calculate the axial FWHM, 0.1 mm (Fig 2.4).

2.3.2 Blood oxygen characterization

To characterize the blood oxygen saturation (sO_2) measurements using the photoacoustic system, spectroscopic measurements of bovine blood using 5 wavelengths between 700-850 nm with increments of 30 nm were collected. The blood sample was measured using a custom acoustically transparent ballistic gel (Humimic Medical Gelatin 2) phantom with

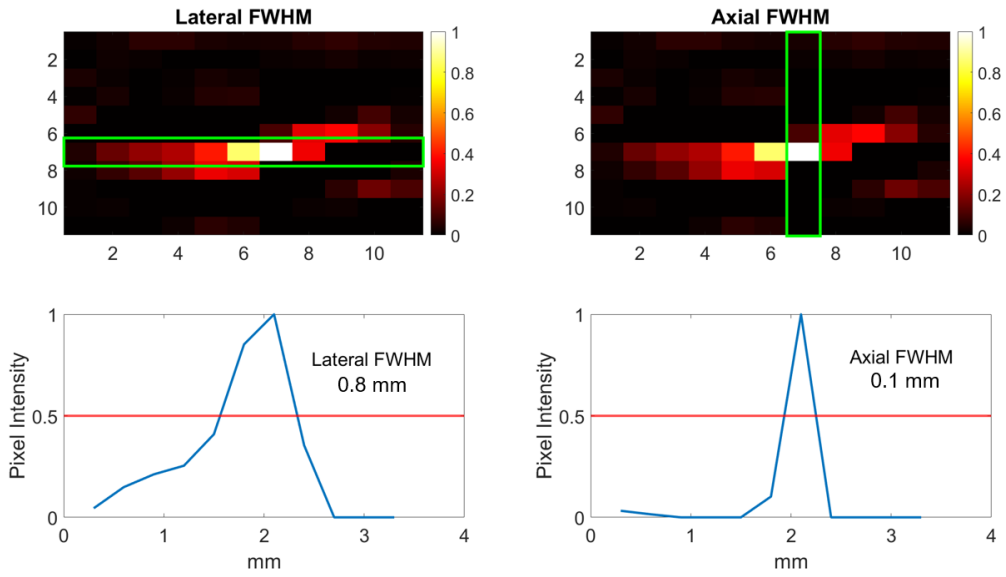

Figure 2.4: a-b) A close-up of the image corresponding to the pencil lead with the maximum intensity pixel in the field of view. The lateral row and axial column are highlighted by the green box. The pixel intensities in the row and column were normalized and plotted (c-d); the lateral and axial full width half maximum (FWHM) were calculated 0.8 mm and 0.1 mm respectively.

a blood flow channel. The handheld USPA transducer was placed 7 mm above the blood flow channel. The USPA system was used to aquire simultanous US and PA images.

To characterize the blood oxygen saturation measurements from the USPA system, cow blood was imaged while constantly being purged with CO_2. The blood sample was diluted by a 1:1:0.1 ratio of bovine blood (Lampire Biological Laboratories), phosphate buffer solution (Corning) and intralipid. Ground truth measurments of sO_2 were performed using an optical reflectance fiber probe, which used 4 white light pulses followed by a dark light signal for correction. For each optical probe measurements, five photoacoustic imaging acquisitions were acquired and averaged. Measurements were taken every 30 seconds while O_2 was purged into a closed flask with the blood mixture. The experiments were carried out for 30 minutes total.

The resulting USPA images from the blood flow phantom were processed using MATLAB to determine the blood oxygen saturation. A mask was created by tracing the blood

channel in the ultrasound images. The mask was then applied to the photoacoustic image to reduce noise and only highlight the region of interest. The overall intensity of the region of interest was calculated for each of the five wavelengths for each photoacoustic frame. The intensity for each wavelength was corrected for the laser power for each respective wavelength. Power values were recorded before every experiment using a power meter (ThorLabs PM400, ES245C Sensor). The photoacoustic Hb and HbO_2 intensities were calculated by multiplying each wavelength photoacoustic intensity by the respective ideal Hb and HbO_2 spectrum and added together for each pixel within the region of interest. The sO_2 values were then calculated by the following formula.

$$sO_2 = \frac{C[HbO_2]}{C[HbO_2] + C[Hb]} \tag{2.3}$$

The optical probe sO_2 measurements and the photoacoustic sO_2 measurements were plotted against each other to visualize the correlation between the ground truth (optical probe) and the photoacoustic measurement. A correlation coefficient of 0.95 was found between the two measurement systems (Figure 2.5).

The experimental blood profile was calculated by multiplying the average experimental sO2 value by the ideal Hb and HbO2 absorption profiles and summing the two together. The measured photoacoustic signal for each wavelength used was also plotted to assess the performance of the USPA system (Figure 2.6).

2.4 Discussion

The developed USPA system can be modified for a variety of applications such as blood oxygen saturation, but also with the use of exogenous contrast agents. The main consideration to improve with this system is the signal to noise ratio with relation to penetration depth. Transducer choice plays a role in achieving the optimal result, two transducers were tested, the L11-4v (7-MHz, 128-element) and the L22-8v CMUT (15 MHz, 256 element)

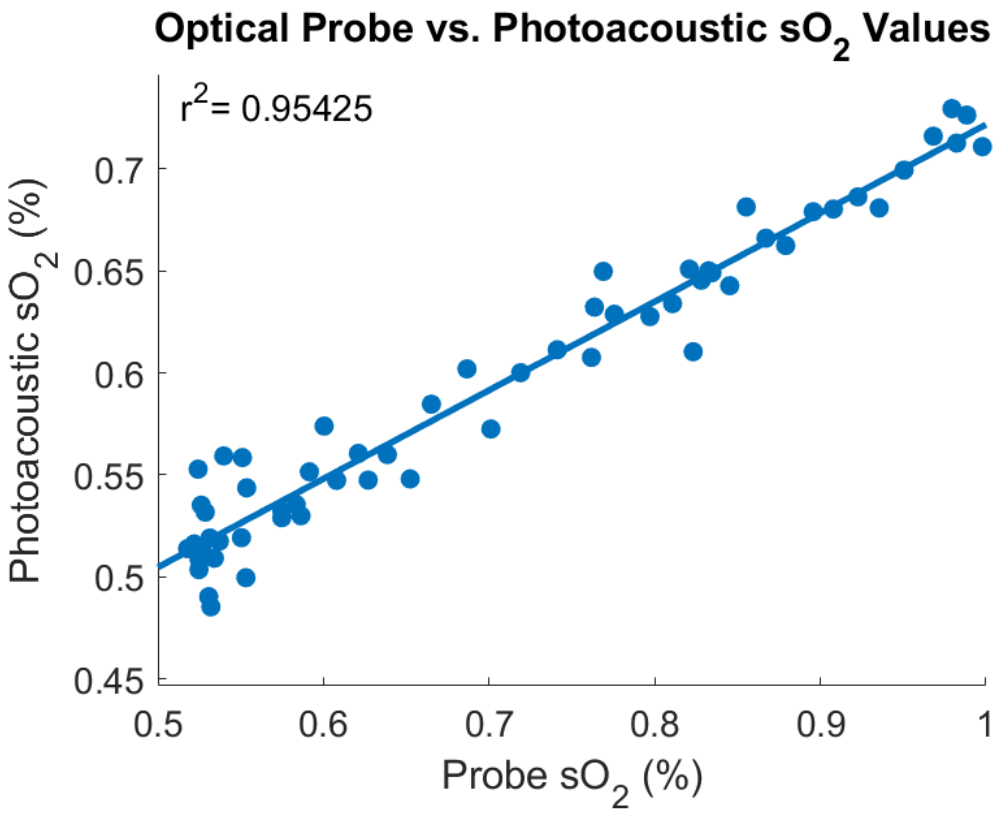

Figure 2.5: The sO_2 measurements from the optical probe vs the measured sO_2 from our photoacoustic imaging system. The oxygen saturation of bovine blood was modified by purging O_2 by bubbling CO_2 into a closed vessel. The correlation coefficient between the two measurements was calculated to be 0.954.

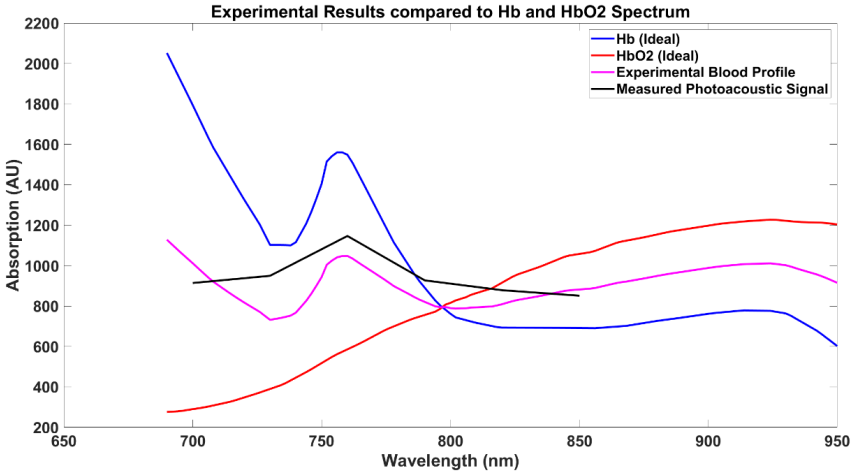

Figure 2.6: The ideal blood oxygenation spectrum in comparison to the experimental blood profile from our photoacoustic system. The measured photoacoustic intensity is plotted in black. The experimental blood profile was calculated by summing the product of the average experimental sO2 value and the ideal Hb and HbO2 absorption profiles.

transducer from Verasonics. It was found that lower frequency transducers could image deeper in tissue, but with a trade off with image quality. The higher frequency transduer was not able to generate accurate PA signals.

It was shown that blood oxygen could be measured using our system and correlates well with the ground truth measurements, however there is still room for improvement. From a hardware perspective, the use of a polyacrylamide head instead of the ballistic gel head could improve signal penetration into tissue and improve SNR. Secondly, the processing algorithms might not be taking into account spectral coloring, a phenomenon known to skew photoacoustic results based on tissue attenuation. Thirdly, improvements can be made on the image processing, currently the whole vessel was segmented from the ultrasound images while most of the photoacoustic signal is from the top of the vessel, leading to a level of noise in the blood oxygenation calculation.

While blood oxygenation was the main application demonstrated in this section, the USPA system has the potential to image exogenous contrast agents with photoabsorbers within the NIR window. Blood oxygenation on its own can be used in identifying vasculature [54] and determining metastatic lymph nodes [28]. The concept can be expanded to image tumor vasculature and hypoxia to gain a better understanding of the tumor oxygen dynamics. However, further clinical *in-vivo* studies need to be performed to determine the clinical viability for USPA blood oxygenation measurements and metatstatic lymph node detection using this system.

2.5 Conclusion

In conclusion, the developed photoacoustic system has been shown to measure blood oxygen saturation in phantoms. The nanosecond pulsed laser and Verasonics ultrasound imaging system were chosen due to their customizability. MATLAB algorithms were written to control the imaging system, acquire spectroscopic photoacoustic images as well as process

the acquired images. The handheld transducer design was optimized to be lightweight and deliver the most amount of light into the tissue. Blood oxygen saturation measurements were performed and compared to optical light probe oxygen measurements resulting in a correlation of 0.95.

While it was shown that the USPA system was able to determine blood oxygenation, further experiments are needed to improve detection accuracy. First, the laser can be tuned further to ensure that that there is adequate power delivery from all the different wavelengths. The crystals should be tuned using a power meter to ensure maximum power delivery. Secondly, the gelatin phantom used to measure the photoacoustic signal did not include any scattering agents or multiple tissue layers, which need to be accounted for when thinking about clinical translatability. Repeating the experiment with a different tissue phantom with multiple skin layers and scattering agents would assist in any corrections that might need to made in the processing. Finally, the PA signal was predominantly at the top of the blood vessel, but the whole vessel was used as the region of interest leading to estimation errors. Reprocessing the datasets using just the top of the vessel where the PA signal is evident would be appropriate to try to improve the correlation coefficient between the USPA system and the ground truth measurements.

Chapter 3

O-NET - Convolutional Neural Network for PA Imaging Segmentation and Oximetry

3.1 Introduction

While spectroscopic photoacoustic imaging (sPA) allows of non-invasive blood oxygenation imaging, accurate quantification of sO_2 is hampered by unknown tissue properties such as optical scattering, absorption and light attenuation in tissue. The amount of light that attenuates deeper into tissue varies as a function of optical wavelength, a phenomenon known as 'spectral coloring' [61]. This phenomenon leads to a skew in blood oxygenation measurements due to the heterogeneous nature of tissue leading to heterogeneous light attenuation. In order to accurately quantify blood oxygen saturation, recent efforts have included principle component analysis or the use of machine learning [62, 63, 64, 65]. Principle component analysis has shown promising results, but it requires knowing the boundary conditions, oftentimes unknown [33]. With advances in machine learning, computer vision techniques such as semantic image annotation have been explored [66]. Semantic image

annotation is a computer vision approach that enables classification and segmentation of sPA images to generate clinically relevant data like blood oxygenation [66] through the use of convolutional neural networks (CNN). One advantage of deep learning is the fast interface time, enabling real time processing and measurement of data [66].

Here we developed a new machine learning approach to obtain quantitative sO_2 from sPA data based on a deep convolutional neural network (CNN). The network consisted of a new deep convolutional neural network architecture - O-Net - that simultaneously estimates vascular sO_2 and segments the blood vessels from two-wavelength PA images generated from three-dimensional Monte Carlo simulations of light transport in tissue. Once the model was developed and trained on the simulated Monte Carlo data, it was trained on experimental photoacoustic data generated from our USPA imaging system.

3.2 Data Generation and Methods

3.2.1 Monte Carlo data generation

Monte Carlo simulations are considered the gold standard in modeling light transport in turbid media and are frequently used to validate numerical models. Monte Carlo simulations are a pure numerical approach and simulates the path taken by 'packets of energy' as they propagate one by one through the scattering medium. Simulated Monte Carlo sPA data was generated by using the MCXYZ program [67]. The data generated consisted of 3.8 x 3.8 x 3.8 cm volumes with background tissue properties using epidermis, dermis, and breast tissue measurements [68] to simulate heterogeneous layered tissue. Within each simulated volume, one and three cylinders with diameters ranging from 0.5 and 4 mm were inserted with random orientations to represent blood vessels. Each simulated vessel was assigned with a with a randomly selected sO_2 value. A laser beam with a 36 x 1.5 mm rectangular aperture directed at the surface of the skin was used in the simulation. Two different optical wavelengths: 700 and 900 nm were used to excite the simulated tissue. 4000 simulations

(2000 for each wavelength) were performed on a cluster containing two 10-core Xeon E5-2640v4 2.40GHz processor with 256 GB of memory for each node. Approximately 106 photon packets were delivered to each simulated volume. Each simulation ran for a duration of 30 minutes. The resulting 128 x 128 x 128-voxel absorbed energy maps were filtered using a 3 x 3 x 3-voxel median filter to reduce the noise from scattering photon packets. sO_2 measurements were performed on a 2-D cross section from the center of the 3-D voxel.

3.2.2 Model construction and training

The O-Net architecture was based on the widely used U-Net architecture [69], which has been effective at image segmentation where the output resembles the input. The O-Net architecture (Figure 3.1) consists of two U-Nets arranged in parallel. The top half of the neural network is focused on blood vessel segmentation while the bottom half estimates the sO_2 in the vessels. ELU activation functions were used except for all of the levels except the last stage, where a sigmoid function was applied. Since the output sO_2 has a range between 0 and 1, the sigmoid function was deemed appropriate. This activation combination demonstrated better accuracy than linear, ELU, or RELU activations alone. To avoid overfitting, dropout layers were added in each level after the first convolution layer. Two sets of 128 x 128 pixel PA image cross sections representing the two simulated wavelengths, 700 and 900 nm, were used as the model inputs. The model assumed that the initial pressure distribution was perfectly reconstructed, allowing the model to focus on the optical problem. There have been other models developed that focus on accurately reconstructing the initial pressure distributions, which could be easily combined with our O-Net [70, 71]. To focus the calculation mainly on the blood vessels within the tissue, the top ten rows of the PA images containing signal from the epidermis were zeroed out. The output was a pair of 128 x 128 images, one with the sO_2 estimate and the other with the vessel segmentation. The data was split into an 80%, 10%, and 10% training, validation,

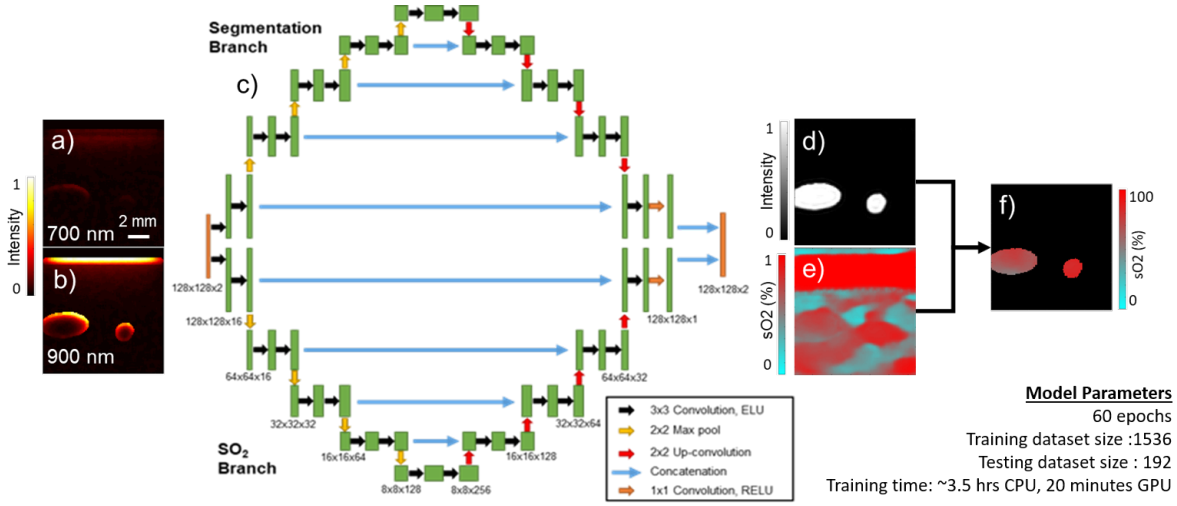

Figure 3.1: O-Net network architecture used for blood vessel segmentation and oxygen estimation using simulated Monte Carlo data. Monte Carlo simulated photoacoustic images for two wavelengths (700 (a) and 900 (b) nm) were inputted into the the model. The segmentation branch outputs the vessel segmentation map (d), and the sO_2 branch estimates the sO_2 within the volume (e). The final output only estimates the sO_2 within the vessel segmentation map (f). The model was trained for 60 epochs with a training dataset size of 1536 images and a testing dataset of 192 images. The training time was roughly 3.5 hours on a CPU and 20 minutes using a GPU.

and testing data sets, respectively. Each PA image pair was normalized by the maximum pixel value, allowing each pixel to range between 0 and 1. The training parameters includes a batch size of 32, for 60 epocs and used an Adam optimizer with a learning rate of 0.001 [33]. The training time was around 3.5 hours and performed using an Intel i5-8350U CPU with 16 GB of RAM.

3.2.3 O-Net custom loss function

The O-Net used a custom loss metric where the mean-squared error of the sO_2 was only minimized within the blood vessels, compared to a standard mean squared error (MSE) loss function that that optimizes the sO_2 for the whole tissue. The standard loss function skewed the sO_2 estimates towards the background tissue, rather than just the blood vessels [33]. The use of the custom loss function leads to large errors in background tissue sO_2 estimates, but

the background tissue estimates are nullified when combined with the accompanying vessel segmentation map from the other half of the O-Net [33]. The segmentation half of the O-Net used the standard MSE loss function. Each of the two losses (sO_2 and segmentation) were weighed equally [33].

3.2.4 Experimental data generation

After the initial training of the model on Monte Carlo simulated data [33], experimental data was used to train the model. Photoacoustic images of cow blood were aquired using a custom USPA system. The USPA system consisted of an nanosecond pulsed laser (Phocus Mobile HE, Opotek) which has a low pulse frequency (10 Hz) and a high pulse energy (80 - 100 mJ/pulse). The accompanying ultrasound system used was a research grade Verasonics Vantage 256. A ballistic gel phantom with a blood flow channel was imaged. The cow blood was diluted by a 1:1:0.1 ratio of bovine blood (Lampire Biological Laboratories), phosphate buffer solution (Corning) and intralipid. Ground truth sO_2 measurements were performed using an optical reflectance fiber probe. The blood oxygen was modulated by purging CO_2 gas into the blood and reoxygenated by purging O_2 gas into the blood. Five photoacoustic images were taken and averaged for each optical probe ground truth measurement. Two wavelengths were used in the image acquisition, 700 and 850 nm. A total of 410 PA images were collected for each of the two wavelengths. 369 images of each wavelength were used for the training set, 41 for the validation and 41 for the testing set. The sO_2 values from the optical probe were considered to be the ground truth and were encoded as the pixel values for each pixel in the ground truth sO_2 image. The ground truth vessel anatomy image was obtained by segmented the accompanying ultrasound image.

3.2.5 Linear spectral unmixing

As a way to compare the efficency and performance of the O-Net, linear spectral unmixing was performed on both the simulated and experimental datasets. Linear spectral un-

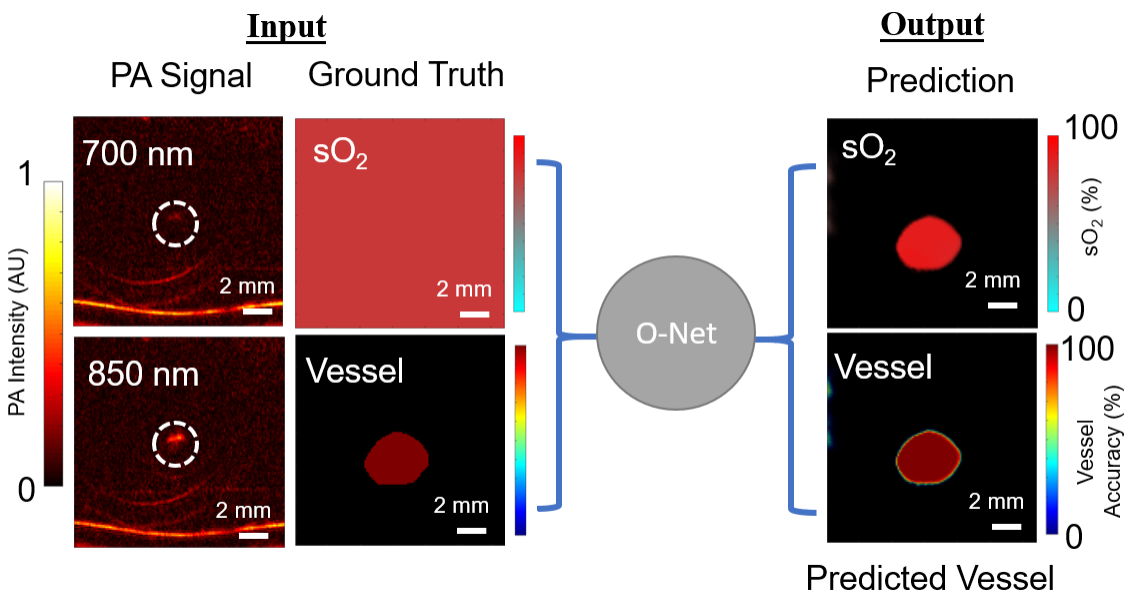

Figure 3.2: Diagram showcasing the inputs and outputs of the O-Net convolutional neural network using experimental data. The inputs include experimental photoacoustic images at two wavelengths, 700 and 850 nm. The ground truth sO_2 value was determined using an optical oxygen probe and encoded as the pixel value of every pixel within the sO_2 image. The fourth input is the segmented vessel map. The outputs are the predicted sO_2 and vessel anatomy.

mixing assumes that both the simulated and experimental data contained only two optical absorbers, Hb and HbO_2. The absorption spectra for these two absorbers is known [68]. This simplifies the model by assuming that the PA signal in each pixel is proportional to the weighted sum of the concentration of Hb and HbO_2 with respect to the wavelength as described in the equation below where λ is the wavelength, μ_{a} is the absorption coefficient of the absorber and C is the concentration [33].

$$PA(\lambda) = \mu_{\text{aHbO}_2}(\lambda)C[HbO_2] + \mu_{\text{a Hb}}(\lambda)C[Hb] \tag{3.1}$$

The sO_2 in each pixel was calculated using the following equation [33].

$$sO_2 = \frac{C[HbO_2]}{C[HbO_2] + C[Hb]} \tag{3.2}$$

3.3 Results

3.3.1 Custom loss function accuracy

The custom loss function developed was able to segment the vessel and measure the sO_2 within the vessel for better estimation. For comparison, sO_2 estimates were also calculated using the standard root mean squared error (RMSE) loss function. When comparing the custom loss function to the RMSE loss function, there was a significantly *(p-value < 0.001)* lower mean absolute error.

The custom loss function was also compared to linear unmixing. The O-Net custom loss function out performed linear unxming for noise free data as shown in Figure 3.3. The standard MSE loss function was not able to accurately determine sO_2 and resulted in high errors. This is due to the inclusion of background tissue signals in the optimization process. Linear unmixing showed higher error for deeper structures in the noise free data.

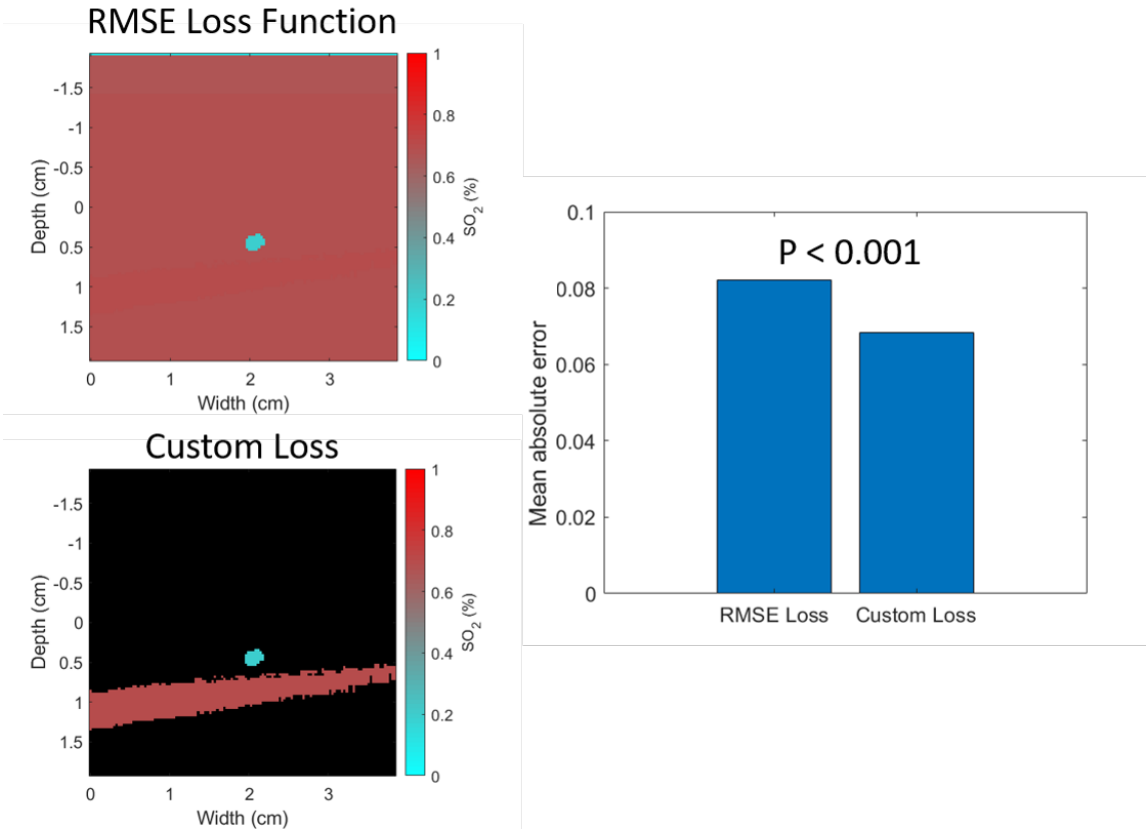

Figure 3.3: The dataset was tested on two different loss functions, root mean squared error (RMSE) and a custom loss function. The sO_2 estimations from the two loss functions were compared using the blood vessel simulated data. The custom loss function estimates sO_2 within the vessels compared to RMSE which estimates the sO_2 throughout the tissue, leading to skewed estimations because of the background tissue signals. The mean absolute error was significantly lower when using the custom loss function compared to RMSE.

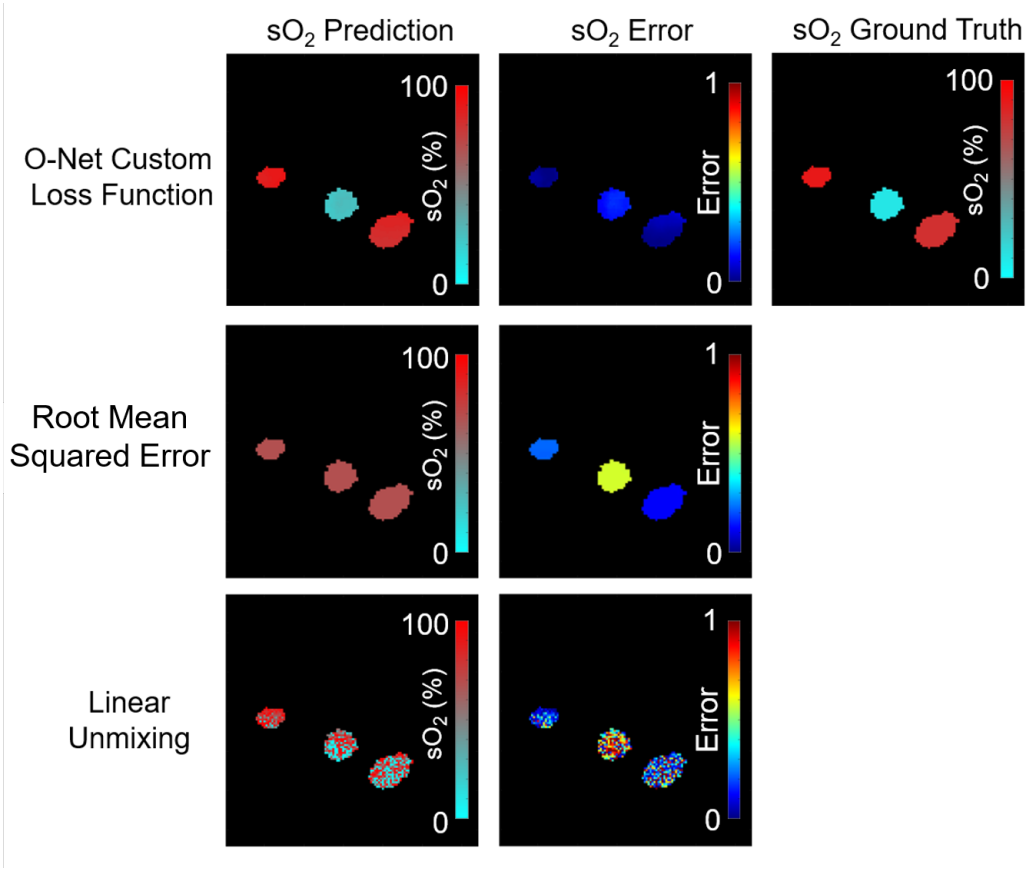

Figure 3.4: The custom O-Net loss function compared with Root Mean Squared Error (RMSE) and Linear Unmixing. The custom loss function outperforms both RMSE and LU in being able to accurately predict the sO_2 in Monte Carlo simulated data. The sO_2 error is shown in the middle column.

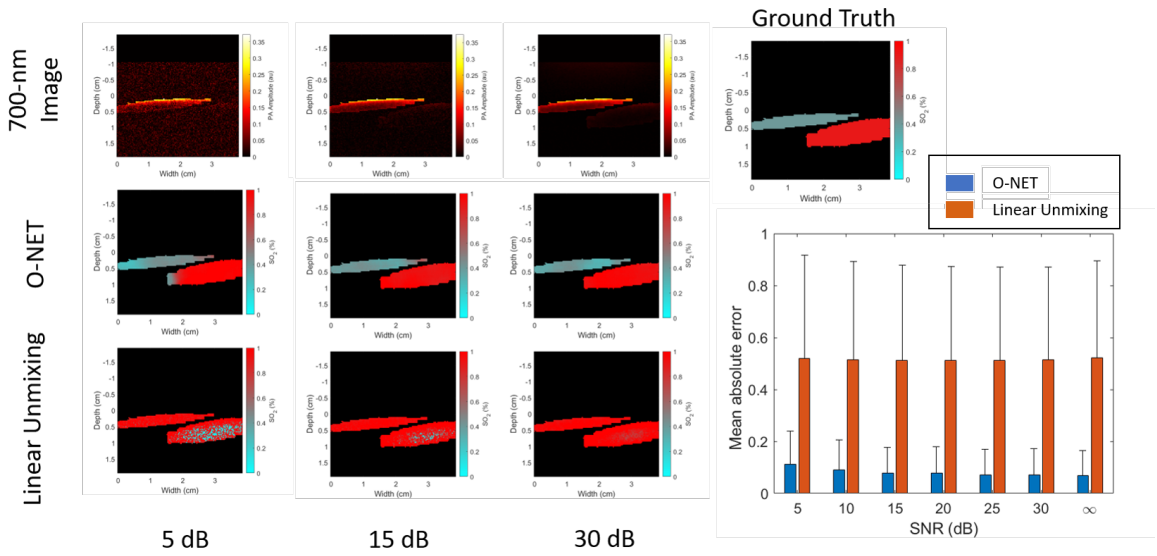

Figure 3.5: Different levels of noise were added to the simulated data and retrained using the O-Net. For comparison, the same datasets also underwent linear unmixing. Three representative noise groups are shown in the figure. The mean absolute error was determined for both the O-Net and linear unmixing. The mean absolute error of the O-Net was lower than linear unmixing for all of the noise groups.

3.3.2 Robustness to noise

The O-Net was able to accurately determine the sO_2 in noise free data compared to using the MSE loss function and linear unmixing. To test the robustness of the O-Net, different levels of noise were added to the images and retrained using the model. The different levels of noise were balanced to have an average image signal to noise ratio (SNR) of 5, 10, 15, 20, 25, or 30 dB. The noise added data was also processed using linear unmixing as a comparison. The mean absolute error was calculated for each noise group (Figure 3.5). The predicted sO_2 was also compared to the ground truth sO_2 for both the O-Net and linear unmixing methods (Figure 3.6).

While the O-Net has shown to outperform MSE and linear unmixing in estimating sO_2 within the blood vessels, the segmentation accuracy of the O-Net was also determined for the different noise levels (Figure 3.7 a). The overall segmentation accuracy was approximately 96% for all of the different noise level cases. The false negative and false positive

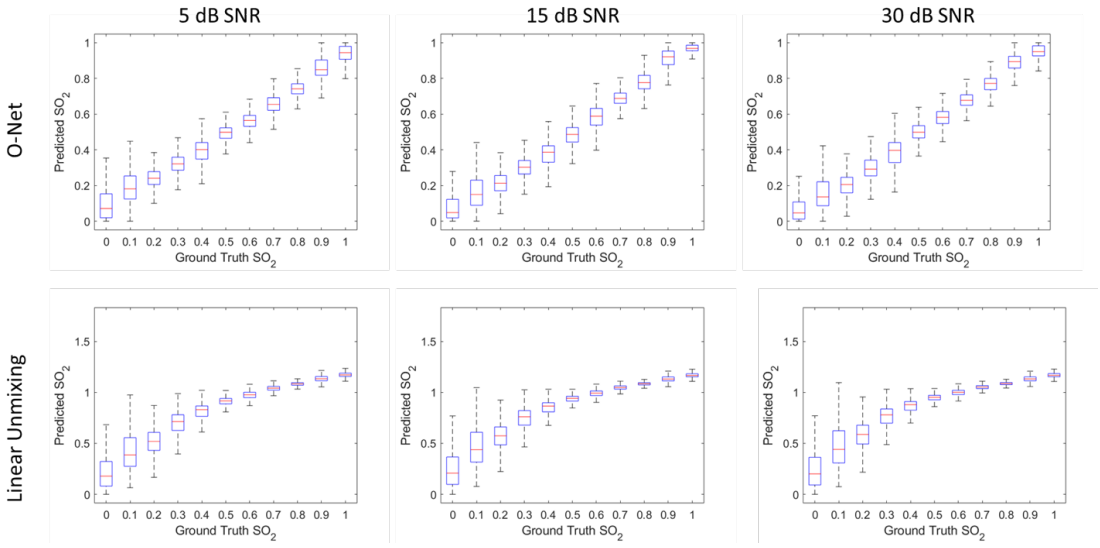

Figure 3.6: The predicted sO_2 was compared to the ground truth sO_2 for the different noise levels (5, 15, 30 dB SNR shown here) for both O-Net and linear unmixing. The O-Net showed a linear correlation between the predicted and ground truth sO_2 values for all of the noise levels, where linear unmixing tended to overestimate the sO_2 for all of the noise levels.

error rates were also determined (Figure 3.7 b). The false positive error rate was close to zero for all the different noise cases, indicating that the model did a good job of determining the blood vessel. The false negative error rate increased as the noise within in the images increased. A false negative indicates that the model determined a pixel not to be a part of the vessel, when it actually is. With the addition of noise, it is suspected that edges of the vessel are harder to determine for the model, leading to the increase in false negative error rates.

3.3.3 O-Net performance vs linear unmixing on experimental data

The O-Net was able to accurately determine the sO_2 compared to the ground truth in simulated images. Even with the addition of noise, the O-Net outperformed linear unmixing. The O-Net performance was tested using experimental data acquired from our USPA imaging system. Linear unmixing was also performed on the same data set of images for comparison. The estimated sO_2 was compared to the ground truth for both methods. The

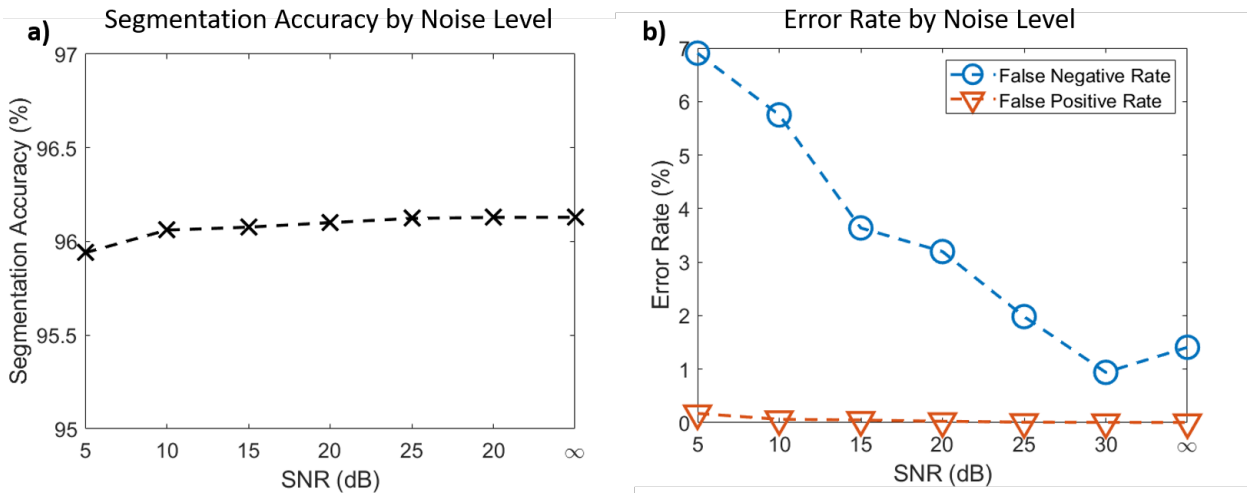

Figure 3.7: (a) The segmentation accuracy for the different noise cases. The segmentation accuracy was around 96% for all of the different noise cases. (b) The false negative and false positive error rates for the different noise level cases. The false positive error rate stayed close to 0 for all of the noise cases; the false negative error rate was higher in images with higher levels of noise, indicating that model had trouble determining the edge cases of the vessels with the introduction of noise.

O-Net was able to better predict the sO_2 with a r^2 of 0.847 compared to a r^2 of 0.618 for linear unmixing (Figure 3.8).

3.4 Discussion

Overall, the O-Net with the custom loss function outperformed the mean squared error (MSE) loss function and the linear unmixing method in both vessel segmentation and sO_2 estimation in both simulated and experimental data. Linear unmixing showed to overestimate the sO_2 predictions. This is probably because of the weak signals from deeper in the tissue. The MSE loss function was not able to accurately determine the sO_2 due to the background bias in the calculations. With the introduction of noise, the O-Net was still able to accurately estimate blood oxygen, but did show an increasing false negative error rate in vessel segmentation as the noise in the images increased. We suspect the error is stemming from the edges of the vessels, because the false positive error rate was consistently low for all of the noise cases.

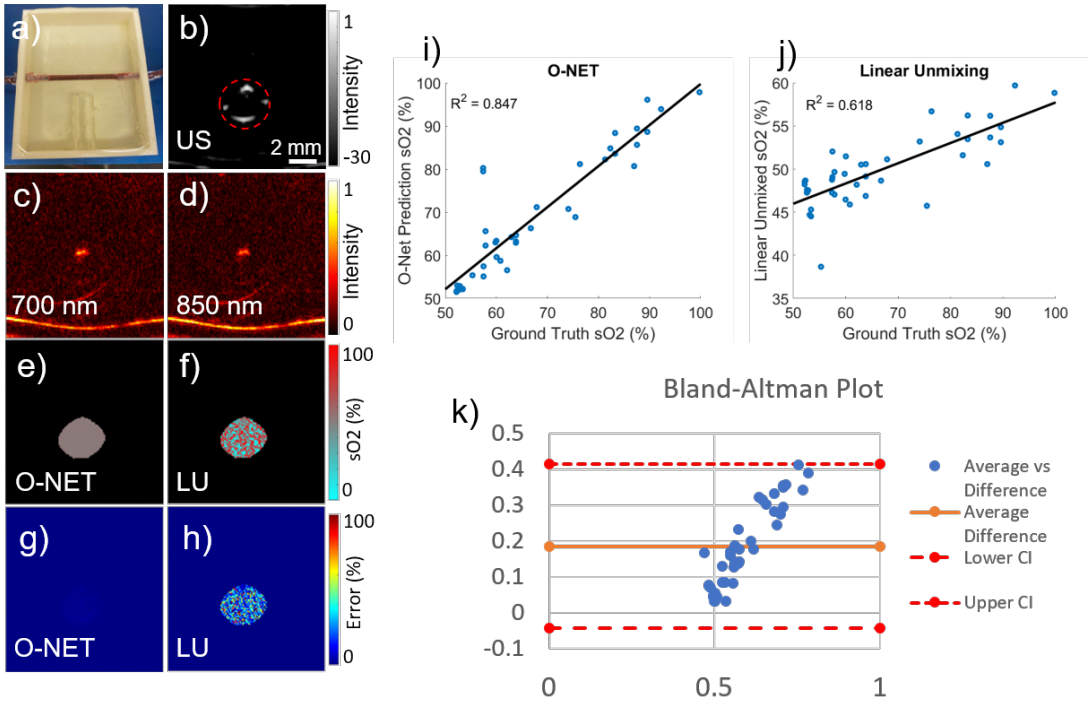

Figure 3.8: a) the ballistic gel blood flow phantom used to acquire the USPA images. b) the corresponding ultrasound image used to generate the vessel map for the O-Net, indicated by the dotted red circle. c-d) the corresponding photoacoustic images. Two wavelengths were used 700 and 850 nm. e-f) the sO_2 predictions within the blood vessel for the O-Net (e) and linear unmixing (f). g-h) the sO_2 prediction error for the two methods. i) the correlation between the ground truth sO_2 and the O-Net predicted sO_2. j) the correlation between the ground truth sO_2 and the linear unmixed sO_2 prediction. k) Bland-Altman plot showing the average difference between the O-NET and the linear unmixing methods with a 95% confidence internval.

The O-Net also outperformed the linear unmixing method when trained and tested using experimental data. However the O-Net correlation between the ground truth sO_2 and the predicted sO_2 was lower than the simulated data with added noise. A larger data-set with multiple vessel geometries are needed to properly train the O-Net using experimental data to improve the performance. Additionally, the vessel was segmented using the ultrasound image for the whole vessel, where the PA signal was emitted mainly from only the top of the vessel. Better segmentation and more geometries could improve the O-Net performance using experimental data.

In addition to better segmentation and sO_2 predictions using the O-Net, it is also computationally fast. The average prediction time per image was under 50 ms, potentially enabling real-time sO_2 prediction and segmentation. The O-Net has the potential to be augmented with our custom USPA system for faster imaging processing and sO_2 quantification.

3.5 Conclusions

We have developed a new neural network, O-Net, that simultaneously estimates blood sO_2 and segments blood vessels from a pair of PA images. The network vastly outperforms linear spectral unmixing on a data-set generated from 3-D Monte Carlo simulations. The model was also outperformed linear unmixing on experimentally acquired photoacoustic images from the developed USPA system. Overall, this approach could be used to implement quantitative oximetry and vessel segmentation deep in tissue.

While the model shows improvement compared to the currently linear unmixing method, the model performance can be further improved by retraining the model on more simulated and experimental data. The simulated data used in the model is a good starting point, but realistically, the sO_2 within the blood vessel represents a Gaussian distribution instead of just one value. Recreating the Monte Carlo data set with a Gaussian sO_2 distribution will be

needed to improve the model. Secondly, the experimental data used to train the model were only acquired using the tissue mimicking gelatin phantom used in Chapter 2. Additionally, the vessel position in the experimental data set was the same for all of the images. Acquiring experimental data with the vessel in different positions within the image would be needed to train the model further. Adding tissue layer with scattering agents as well as different levels of melanin on the top layer would help in the training the model for accuracy for different attenuation factors. Performing a study with multiple phantoms modulating the vessel depth, melanin levels, scattering levels would provide a more complete experimental data set.

Chapter 4

Molecular targeting of perfluorocarbon core nanodroplets for metastatic lymph node detection using ultrasound

4.1 Introduction

Ultrasound imaging contrast agents have augmented the modality's potential for a wide variety of diagnostic and therapeutic applications, such as vascular mapping, tissue ablation, clot disruption, targeted drug delivery, and lithotripsy [72, 73, 74, 36]. Typically, microbubbles with a gaseous air or perfluorocarbon core are used to provide imaging contrast due to the large acoustic impedance mismatch between their gaseous core and the surrounding water-based tissue. In addition to enhancing contrast, molecular information can be obtained through attachment of targeting molecules to the surface of the microbubbles. This has enabled molecular imaging of oncological biomarkers, such as VEGFR2, for visualization of angiogenesis [75, 76, 77]. While microbubbles have proven to be effective contrast agents with limited clinical adoption, their relatively large size restricts them to the vasculature and results in rapid clearance from the bloodstream.

Nano-sized contrast agents overcome the size restrictions of microbubbles by allowing for permeation into leaky vasculature of tumors as leading to potential ultrasound guided tumor specific molecular imaging targets [41]. One particular class of ultrasound contrast agents, perfluororcarbon nanodroplets (PFCnDs), have been studied due to their phase change properties, leading to reduced size and improved in-vivo stability [78]. The PFCnDs contain a liquid perfluorocarbon core surrounded by a lipid or protein shell. The ultrasound contrast is produced when the PFCnDs are activated using an optical or acoustic stimulus to induce the liquid perfluorocarbon core to vaporize into a gaseous microbubble. The microbubbles reflect the incident acoustic waves, creating the contrast in the image. The phase change dynamics of the PFCnDs have led to their use in a variety of imaging and therapeutic applications [79, 46, 80, 81, 82]. Optical activation of the PFCnDs is achieved by incorporating an optical absorber into the PFCnD and activating with a pulsed laser [57]. While the choice of optical absorber and excitation wavelength allow for PFCnD versatility, the optical activation depth is limited due to light attenuation in tissue. Acoustic droplet vaporization (ADV), in comparison, allows for deeper activation due to the low attenuation of acoustic waves in tissue. ADV works by exposing the nanodroplets to a peak negative pressure lower than both the core's vaporization pressure and the Laplace pressure from the stabilizing shell.

4.1.1 The use of ultrasound in metastatic lymph node staging

Knowing the lymph node metastatic state is paramount in accurately staging cancers and developing the appropriate treatment plan [3]. While positron emission tomography (PET), magnetic resonance imaging (MRI) and x-ray/computed tomography (CT) are used to screen for metastatic lymph nodes in clinical practice, they are limited by size resolution and have difficulty detecting lymph nodes less than 10 mm [83]. For smaller metastases, ultrasound imaging is used due to the information provided in addition to size, such as echogencity, echogenic hilus, calcification and necrosis [16] as well as vasculature infor-

mation [83]. However, ultrasound is limited by contrast and depth in comparison to the other modalities. Microbubble contrast agents have been used to enhance ultrasound contrast for better detection [83], but the size limitation of microbubbles limits the penetration into smaller vessels.

Perfluorocarbon nanodroplets have the potential to enhance the use of ultrasound by providing molecular information through various targeting strategies. Multiple publications have reported the development of perfluorocarbon nanodroplets to target extracellular markers such as folate receptors [84, 85], and human epidermal growth factor receptor-2 (HER2) [86]. While these examples show targeting to specific molecules, the PFC core used in the droplets have boiling points lower than the surrounding tissue, leading to one-time activation and instability.

In this chapter, antibody-functionalized phase-changing perfluorohexane-core nanodroplets (PFHnD-Ab) for molecular ultrasound imaging is described. The perfluorohexane core has a boiling point of 56 °C. This allows for repeated vaporization and recondensation of the PFHnD-Ab for more robust imaging. The molecular specificity is conferred through directional attachment of epidermal growth factor receptor (EGFR) antibodies to the surface of the nanodroplets through a hydrazide-aldehyde reaction. The molecular specificity is demonstrated through fluorescence microscopy and ultrasound imaging [87]. The impact of repeated vaporization cycles on molecular binding is investigated. Overall, the results show that the PFHnD-Ab provide reliable targeting and contrast for extended imaging applications.

4.2 Methods

4.2.1 Perfluorohexane Nanodroplet Synthesis

Perfluorocarbon nanodroplets were synthesized using a modified sonication-based method described in Hannah, et al. [59], 2.2 μmol of lipids consisting of a 1:0.2:0.03 molar ratio of

DSPE-PEG-2k, DPPC and DSPE-PEG-Hz respectively were added to 1 mL of chloroform (Oakwood Chemical, Estill, South Carolina, USA) in a 50 mL round-bottom flask. The solution was evaporated to form a lipid cake using a rotary evaporator (Heidolph, Schwabach, Germany) at 38.5 °C, 250 mbarr and at a speed of 50 rpm. For the nanodroplets used in the fluorescence experiments, 20 µL of 1 mg/mL DiD (Biotium, San Francisco, USA) fluorescent dye was also added to the mixture prior to evaporation. Upon complete evaporation of the chloroform, the lipid cake was resuspended in 1 mL of DI water. The solution was then vortexed (VWR, Radnor, PA, USA) for 30 seconds at 3000 rpm and sonicated using a 35-kHz ultrasound water bath sonicator (VWR Symphony, Radnor, PA, USA) at room temperature for 1 minute. The resulting mixed lipid solution was transferred to a 20-mL centrifuge tube in an ice bath and 50 µL of perfluorohexane (Fluoromed, Round Rock, TX, USA) was added to the solution. The mixture was then sonicated using a microtip probe sonicator (QSonica, Newtown, CT, USA) at two different intensities, one of low intensity (1% power, 1 s on, 5 s off, 20 total pulses) followed by a high intensity (50% power, 1 s on, 10 s off, 5 total pulses). Following sonication, the nanodroplets were washed three times by centrifugation (MiniSpin, Eppendorf, Hamburg, Germany) at room temperature first at 800 rcf for 60 seconds keeping the supernatant, followed by 1300 rcf for 60 seconds, once again keeping the supernatant and finally centrifuged again at 3500 rcf for 60 seconds, this time discarding the supernatant and resuspending the pellet in 1 mL of DI water for the final PFHnDs.

4.2.2 Antibody Conjugation to the PFHnDs

Epidermal growth factor (EGFR) antibodies (Bio X Cell, Lebanon, NH, USA) were filtered using a 30 kDa MWCO centrifuge filter (Sigma Aldrich, St. Louis, MO, USA) for 15 minutes at 3000 rcf (Sorvall ST8, Thermo Fisher) resulting in a final concentration of 1 mg/mL. The antibodies were then fluorescently labeled using the Alexa Fluor 555 (AF555) antibody labeling kit (Thermo Fisher Scientific, Waltham, MA, USA) following

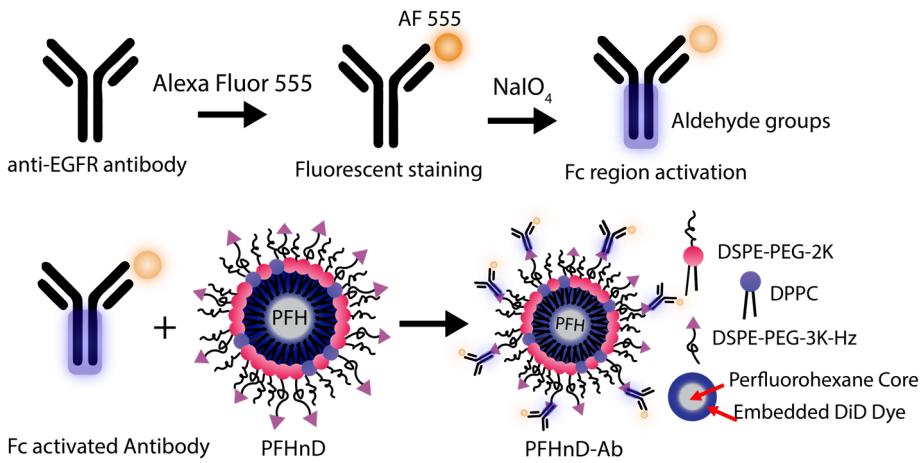

Figure 4.1: The antibodies were first labeled with AF 555 antibody labeling kit. Secondly, the Fc region of the antibody was oxidized by reacting with 100 mM $NaIO_4$ leading to aldehydes on the Fc region. The aldehydes on the activated Fc region then bind to the hydrazides available on the surface of the PFHnDs, forming a stable hydrazone bond, leading to the final antibody conjugated nanodroplet (PFHnD-Ab). The core of the PFHnD contains perfluorohexane (b.p. 56 °C) and DiD fluorescent dye.

the included protocol. The labeled antibodies were stored as a stock solution at 4 °C until needed.

The procedure for oxidizing the Fc region to produce aldehyde groups for binding was adapted from previous work on noble metal nanoparticles [88] and barium titanate nanoparticles [89]. To briefly summarize, 10 µL of the AF555 labeled antibodies were added to 130 µL of 100 mM Na_2HPO_4.Fifty microliters of this solution was added to 5 µL of 100 mM $NaIO_4$. It is important to note that the $NaIO_4$ should be made immediately before use for optimal results. After 30 minutes of incubation with $NaIO_4$, 150 µL of PBS was added to stop the reaction. Aldehydes were confirmed using the Purpald (Alfa Aesar, Tewksbury, MA, USA) test: 20 µL of the antibody solution was added to 60 µL of a 10 mg/mL solution of Purpald mixed with 1 M NaOH. The purpald solution qualitatively turns violet in the presence of aldehyde groups.

To attach the antibodies to the surface of the PFCnDs, a direct conjugation strategy was employed using the aldehydes on the Fc region of the antibody to bind to the free hydrazides on the surface of the PFCnDs, creating a stable hydrazone bond. 200 µL of the

aldehyde activated antibodies were then added to a solution with 200 µL PFHnDs (2.2×10^8 particles/µL) and 100 µL of BupH coupling buffer (0.1 M sodium phosphate, 0.15 M NaCl, pH 7.2; ThermoFisher, Waltham, MA, USA). The mixture was incubated for 4 hours at room temperature in the dark on a shaker (10 rcf; Belly Dancer, IBI Scientific, IA, USA). Post incubation, the solution was washed three times at 9000 rcf for 2 minutes (MiniSpin Centrifuge, Eppendorf, Hamburg, Germany) to remove the unbound antibodies by removing the supernatant each time and resuspending the pellet in 400 µL of PBS. The resulting antibody-nanodroplet product (PFHnD-Ab) was resuspended in 200 µL of PBS after the third wash.

4.2.3 Molecular Targeting of EGFR-targeted PFHnDs to FaDu cells

FaDu cells (ATCC) were used as the *in-vitro* model of head and neck squamous cell carcinoma due to their over-expression of EGFR on the surface, which enables molecular targeting via the anti-EGFR antibody. The cells were cultured in T-75 flasks by using Dulbecco's Modified Eagle's Medium (DMEM; Corning, Tewksbury, MA, USA) supplemented with 10% fetal bovine serum (Gibco - Thermo Fisher, Waltham, MA, USA) and 1% penicillin (Corning, Tewksbury, MA, USA). FaDu cells were suspended in 2 mL of DMEM for a final concentration of 4.42×10^5 cells/mL for use in the targeting experiments. Then, 200 µL of the cell solution was treated with 100 µL of 4×10^7 nanodroplets/µL solution of fluorescent, PFHnD-Abs and incubated for 30 min at 36 °C.

Two control experiments were conducted. Firstly, cells were incubated with PFHnDs without conjugated antibodies to determine the level of non-specific binding. Secondly, cells were first subjected to unlabeled free floating anti-EGFR IgG (71 µg/mL) to block the specific receptors, inhibiting any EGFR-mediated PFHnD-Ab binding, followed by the addition of the same concentration and volume of PFHnD-Abs as the positive group. To remove unbound nanodroplets, the cells were washed five times for 30 s at 800 rcf (Minispin, Eppendorf), each time removing the supernatant and re-suspending in 400 µL of PBS. Af-

ter the final wash, the cells were then re-suspended in 200 μL of PBS and imaged under a microscope (DMi8, Leica, Germany). Dark field was used to image the cells, the red fluorescence channel was used for the PFHnDs (DiD), and the yellow fluorescence channel was used for the antibodies (AF555). To quantify the PFHnD fluorescence, the dark-field images were segmented in MATLAB using the Image Processing Toolbox (MathWorks, Natick, MA, USA). The coordinates of all of the cells in the dark field image were determined and then used to quantify the fluorescence from the corresponding co-registered fluorescent images. The Mann-Whitney U-test was used to determine the statistical significance of the results.

4.2.4 Ultrasound Imaging of FaDu Cells

To validate the ability to image the PFHnD-Abs targeted to the cells, tissue-mimicking polyacrylamide phantoms were fabricated. Polyacrylamide phantoms have tissue-like acoustic properties such as density, sound speed, acoustic impedance and attenuation[90, 91, 92]. 10 mL of 30% polyacrylamide solution (Sigma-Aldrich, St. Louis, MO, USA) was added to 20 mL of DI water and 30 μL of ammonium persulfate (Sigma-Aldrich, St. Louis, MO, USA) to generate a 30 mL phantom. 27 mL of the solution was set into the mold first followed by adding 33.75 μL of Tetramethylethylenediamine (TEMED; Alfa Aesar, Haverhill, MA, USA) crosslinker to create the phantom base layer. The phantom was allowed to set for 5 minutes until hardened. The remaining 3 mL of PA solution was mixed with cells and 3.75 μL of TEMED crosslinker. The solution was added to the top of the base layer and allowed to set.

The experimental setup, ultrasound imaging acquisition sequence and image processing was adapted from previous work [87]. To briefly summarize, the custom ultrasound imaging setup (Fig. 4.2) used a 15-MHz, 256-element linear array ultrasound transducer (L22-8v, Verasonics, Kirkland, WA, USA) powered by a Verasonics Vantage 256 (Verasonics, Kirkland, WA, USA) ultrasound imaging system and single element high intensity focused

ultrasound (HIFU) transducer (H-151, Sonic Concepts, Bothell, WA, USA). A polyacrylamide coupling cone was used to focus the HIFU waveform to the activation spot. The ultrasound image acquisition sequence was synchronized with the HIFU through a digital trigger output from the Verasonics imaging system. The trigger output was generated using an arbitrary waveform generator (Tektronix, Beaverton, OR, USA), which created a 10-cycle, 1.1-MHz sinusoid burst. The waveform was then amplified by a 200-W radio frequency power amplifier (1020L, E & I).

The image beamforming and processing methods were adapted from previous work [87]. The image reconstruction and data processing were completed using the Verasonics reconstruction algorithms. Briefly, each B-mode image was acquired using 5 plane-wave transmissions at angles of -18°, -9°, 0°, 9°, and 18°. Six B-mode ultrasound images were acquired before the fist HIFU pulse to be able to reliably determine the background signal. Then, two frames were acquired 500 μs and 400 ms after each HIFU pulse. A delay of 500 μs after the second frame was applied before transmitting the next HIFU pulse. A total of 5 HIFU pulses were applied in each imaging sequence. A differential of frames between pre-HIFU and the first frame after HIFU exposure were used to isolate the signal from the PFHnD vaporization. The differential ultrasound signal was determined within the 3.94 mm^2 focal spot region.

To determine the detection limitation, cells with attached PFHnD-Ab were diluted 10×, 50×, 100×, and 500×. The cells were then embedded into polyacrylamide phantoms and imaged using the same procedure. The initial concentration of cells were measured using an automated cell counter (LUNA II, Logos Biosystems, South Korea).

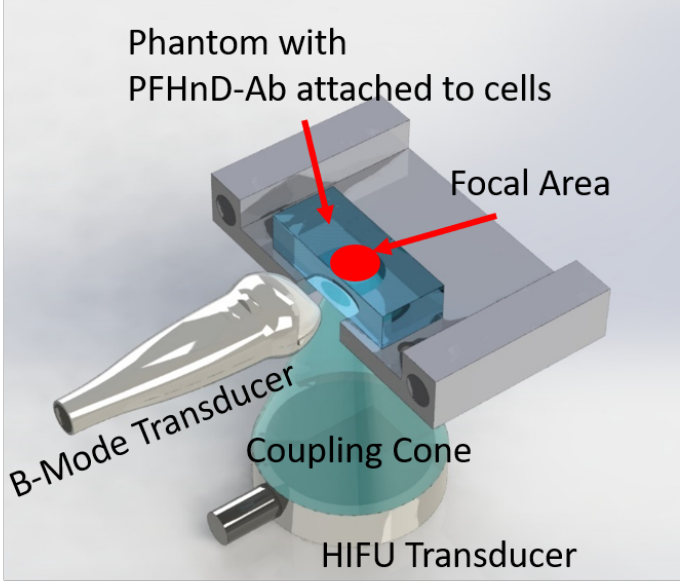

Figure 4.2: Schematic of the custom ultrasound setup. The single element HIFU transducer uses a polyacrylamide coupling cone to deliver the activation energy needed to induce the PFHnD-Ab phase change. Polyacrylamide phantoms PFHnD-Abs conjugated to cells were placed on the 3D printed stage. A linear array B-mode transducer was placed perpendicular to the activation plane to capture the vaporization and recondensation processes.

4.3 Results

4.3.1 Nanodroplet Characterization and Conjugation

The perfluorocarbon nanodroplet (PFHnDs) were synthesized with a perfluorohexane core, and a lipid shell consisting of a 1:0.2:0.03 molar ratio of DSPE-PEG-2k, DPPC and DSPE-PEG-Hz. Using dynamic light scattering (DLS), we obtained a peak size of 530 ±40 nm (n=3) and a zeta potential of -13 ±2 mV (Fig. 4.3). After conjugation to the antibodies, the size distribution of the targeted nanodroplets (PFHnD-Ab) increased to a peak of 640 ±50 nm (n=3) and the zeta potential increased to -9 ±4 mV (n=3). The as-synthesized concentration was 2.2×10^8 nanodroplets/µL as measured by the DLS. Additionally, the amount of antibody conjugated to the nanodroplet surface was quantified using a spectrofluorometer (FluoroMax, Horiba, Kyoto, Japan). The average fluorescent antibody concentration in the sample was measured to be 1.57 µg/mL. This resulted in an average of 3×10^4 antibodies

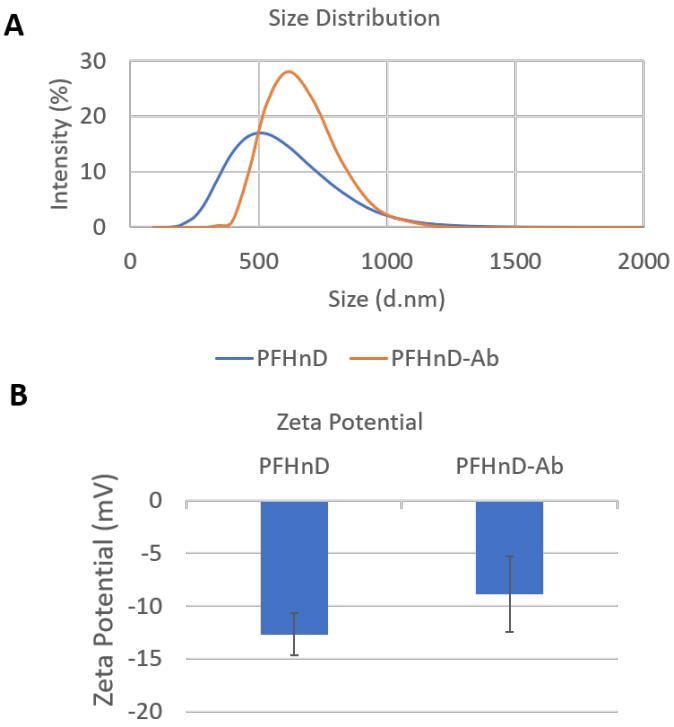

Figure 4.3: A) The size distribution of both the untargeted PFHnDs (530 ±40 nm; n=3) and antibody conjugated PFHnD-Ab (640 ±50 nm; n=3) . B) The zeta potential of both targeted (PFHnD-Ab; -9 ±4 mV; n=3) and untargeted (PFHnD; -13 ±2 mV; n=3) nanodroplets.

per PFHnD.

4.3.2 Molecular Targeting of PFHnD-Ab to FaDu cells

The binding ability of the PFHnD-Abs were explored by culturing with human squamous cell carcinoma cells (FaDu cell line) that overexpress EGFR. The cells were incubated with the PFHnD-Ab at 35 °C for 30 min. Three control groups were included to test the binding specificity of the PFHnD-Abs. Firstly, PFHnDs without conjugated antibodies were incubated with the cells under the same conditions to test for non-specific binding. Secondly, to validate that the binding was due to the EGFR receptor-antibody reaction, the cells were first exposed to free floating anti-EGFR antibodies followed by the same concentration and volume of PFHnD-Abs as in the positive control case. The free floating antibodies are intended to block all the receptor sites on the cells. Thirdly, cells without any

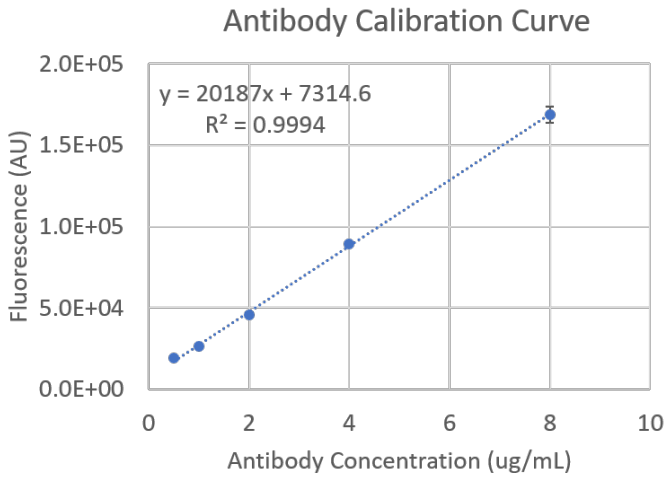

Figure 4.4: Antibody calibration curve measuring the AlexaFluor 555 fluorescence for different concentrations. Fluorescence was measured using a spectrofluorometer with three measurements per concentration.

nanodroplets were also studied. After incubation, the unbound nanodroplets were washed via centrifugation and the cells were imaged using a fluorescence microscope.

The PFHnD-Abs exhibited high levels of binding to the FaDu cells. Both fluorescence channels exhibited a higher fluorescence signal per cell in the targeted group compared to the other groups (Fig. 4.5A), indicating that the PFHnD-Ab bond remained intact after binding. The DiD fluorescence signal of the PFHnD-Ab was 5.63× and 6× greater than the signal in the case of nontargeted PFHnDs (without the antibody) and the EGFR blocking control, respectively. The mean fluorescence per cell (n=567 cells) was 43 ±15 in the DiD channel. The control samples averaged 8 ±5 (n=410 cells) for the nontargeted group and 7 ±4 (n=558 cells) for the EGFR-blocking group (free floating IgG). The cell autofluorescence without the presence of any nanodroplets or antibodies was measured to be 6 ±1. The Mann-Whitney U-test was used to determine the statistical significance since the data distributions were deemed not normal by the Lilliefors test. The PFHnD-Ab sample fluorescence was statistically significant compared to all conditions, as shown in Fig. 4.5B (***,$p < 0.001$). The data suggest that conjugating antibodies to the PFHnDs significantly improves the binding to EGFR overexpressing cells. Some nonspecific binding

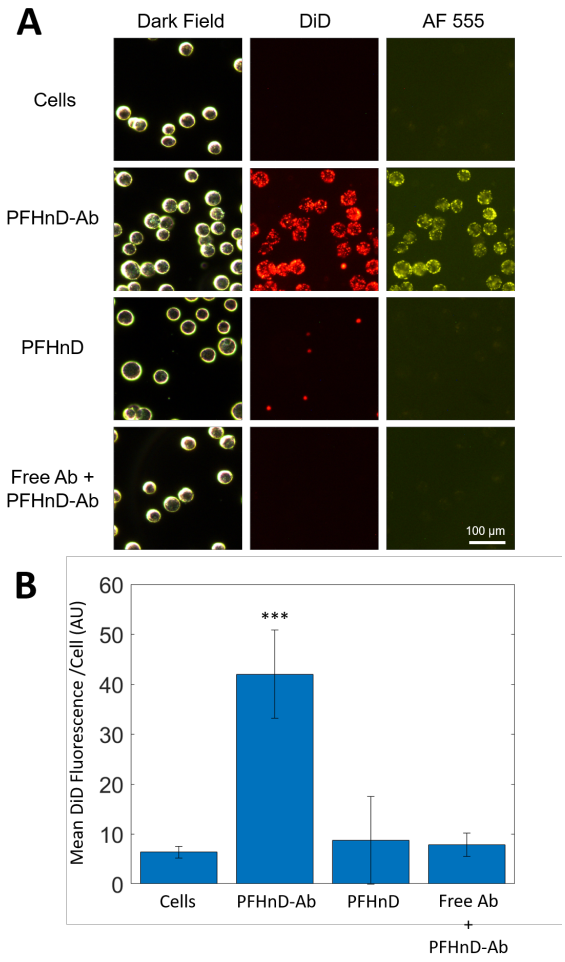

Figure 4.5: DiD lipophilic dye was embedded into the core of the nanodroplets. The antibodies were labeled with Alexa Fluor 555. Targeted and nontargeted particles were allowed to incubate withe FaDu cells for 30 minutes. Additionally, a blocking control was also employed where the cells were saturated with free antibody first before adding targeted nanodroplets. A) Microscope images of cells were obtained in dark field, DiD fluorescence channel and AF 555 channel. B) The DiD fluorescence per cell was computed for cells from each group, resulting in the PFHnD-Ab group having a significantly higher mean DiD fluorescence/cell compared to the other groups ($p < 0.001$).

of non-targeted PFHnDs to the cells was observed; however, there was not any significant statistical difference in the fluorescence with relation to the cell autofluorescence. It was also shown that the PFHnD-Ab conjugate binding to the cells is EGFR mediated and reliant on the presence of EGFR receptors due to the significantly higher fluorescence signal compared to the blocking control case.

4.3.3 Effects of repeated vaporization of PFHnD-Ab and cell targeting efficiency

One of the advantages of using perfluorohexane in the core of the nanodropets is the ability to repeatedly activate the particles from a liquid to gas state. Since the boiling point of PFH is 56 °C, the core recondenses into a liquid nanodroplet after acoustic droplet vaporization [87]. Given the unique dynamics of PFHnDs, it is important to investigate the effects of repeated vaporization of the PFHnD-Abs on their targeting ability. Specifically, we sought to determine if repeated vaporization would impact the molecular specificity of the PFHnD-Ab. To test the targeting efficiency, PFHnD-Ab were vaporized by either 0, 10, 100 or 1000 HIFU pulses before incubation with the FaDu cells. The nanodroplets were allowed to incubate with cells for 30 minutes, followed by centrifugation wash steps to remove unbound nanodroplets. The cells were then imaged using fluorescence microscopy (Fig. 4.6A) and the fluorescent signal in the DiD (Fig. 4.6B) and AF 555 (Fig. 4.6C) channels were quantified. The results show that there is no significant difference in targeting efficiency resulting from prior vaporization of the PFHnD-Ab. This supports the notion that the antibodies remain attached and functional after repeated activation and recondensation.

4.3.4 Effects of repeated vaporization of PFHnD-Ab after cell binding

A second test was carried out to determine whether activation of the PFHnD-Ab once bound to cells would lead to detachment from the cells. Four groups were used in this study,

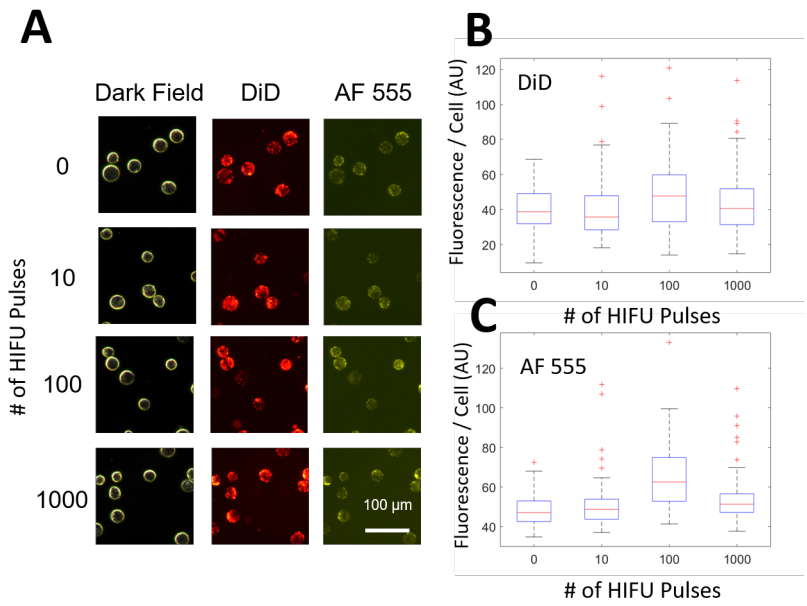

Figure 4.6: The PFHnD-Abs were subjected to different levels of HIFU activation before being incubated with cells to test the antibody-nanodroplet bond robustness. The PFHnD-Abs were split into four groups and exposed to 0, 10, 100 and 1000 HIFU pulses before being being allowed to incubate with FaDu cells. After 30 minutes of incubation with cells, the cells were washed to remove any unbound PFHnD-Abs and were imaged using fluorescence microscopy (A). There was no significant difference in DiD fluorescence (B) and AF 555 (C), indicating that the antibody-nanodroplet bond is strong and can withstand repeated vaporization and recondensation cycles.

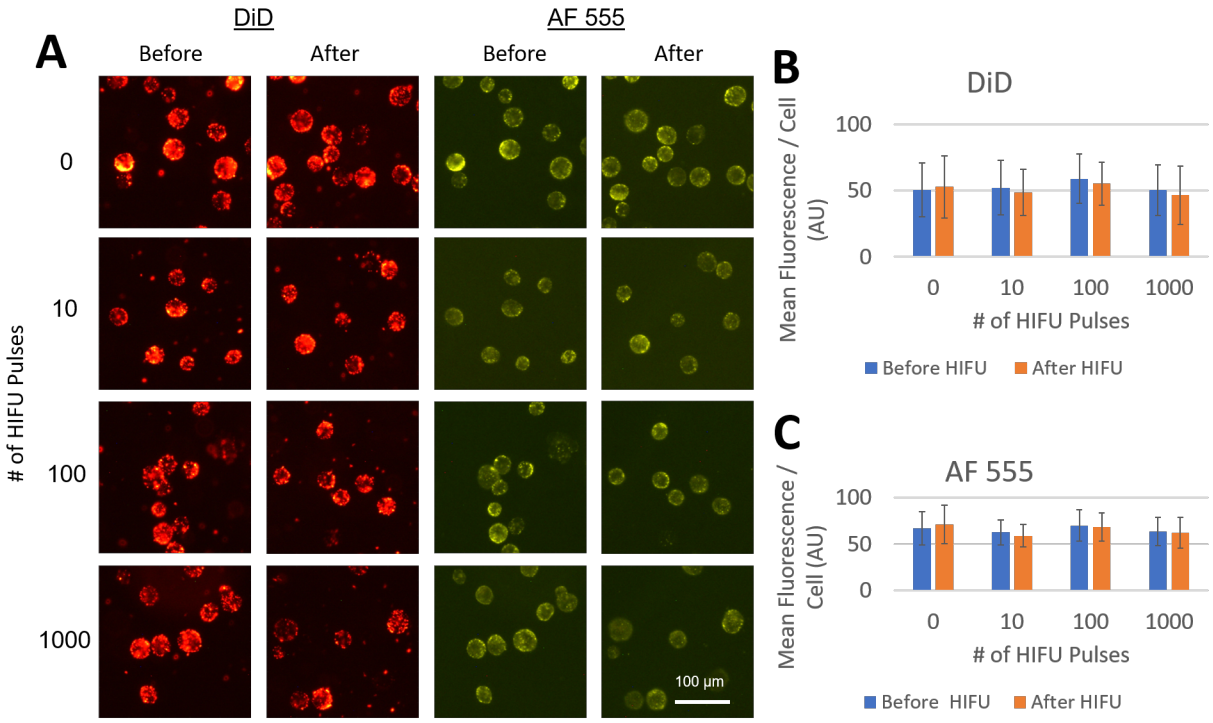

Figure 4.7: The PFHnD-Abs were allowed to incubate with cells and then split into 4 groups, each being exposed to a different number of HIFU pulses (0, 10, 100, 1000). The cells were imaged before and after the HIFU treatment (A), and the mean fluorescence per cell was determined in both the DiD and AF 555 channels. There was no significant difference in the DiD (B) and AF 555 (C) fluorescence per cell after the HIFU treatment, indicating that the targeted PFHnD-Ab remained attached to the cells during the vaporization and recondensation phases.

no activation, 10 HIFU pulses, 100 HIFU pulses and 1000 HIFU pulses. The cells were imaged with fluorescence microscopy before and after the HIFU activation (Fig. 4.7A) and the DiD (Fig. 4.7B) and AF 555 (Fig. 4.7C) fluorescence from the cells was quantified. We found that there was not any significant difference in DiD and AF 555 fluorescence between the groups. The data shows that even after undergoing multiple vaporization-recondensation cycles, the PFHnD-Ab remain bound to their target. Taken together with the results from Fig. 4.6, the experiments show that the PFHnD-Ab are robust molecular imaging agents.

4.3.5 Ultrasound imaging of PFHnD-Ab targeted cells in phantoms

After fluorescence confirmation of PFHnD-Ab targeting to FaDu cells and washing to remove unbound nanodroplets, the cells were embedded in polyacrylamide tissue-mimicking phantoms to enable ultrasonic activation and detection. A custom imaging setup that combines a single-element HIFU transducer for activation with a linear array transducer for imaging was used to evaluate the PFHnDs as contrast agents (Fig. 4.2). The PFHnDs were activated using a 10-cycle, 10.5-MPa, 1.1-MHz burst from the HIFU transducer. The resulting microbubbles were visualized using a B-mode ultrasound transducer that was oriented perpendicular to the HIFU axis. The image acquisition sequence was optimized to allow for capture of the vaporization and recondensation processes of the nanodroplets. The sequence consisted of a total of 5 HIFU pulses, with 6 ultrasound images captured before the first HIFU pulse, and one image after each HIFU pulse, resulting in a set of 16 ultrasound images per acquisition. Additionally, the same cells-only, non-targeted PFHnD, and IgG blocking control groups were used.

The PFHnD-Ab activation was confirmed by taking the difference between the ultrasound images before and after the HIFU activation pulse. The differential amplitudes for each group are displayed in Fig. 4.8A. The phantom containing cells with the PFHnD-Ab resulted in the highest ultrasound signal compared to the control groups (Fig. 4.8B), with a *p-value* « 0.001 (*p-value* = 3.7×10^{-14}). There was negligible ultrasound signal present in the phantom containing only cells, reaffirming that the HIFU levels used in this study were below the cavitation threshold. As expected, there was some signal in the other two control groups, PFHnDs and IgG blocking (free antibody + PFHnD-Abs), due to limited non-specific binding and incomplete washing. Repeated vaporization of the PFHnD-Abs was confirmed from the captured ultrasound images and quantification of the ultrasound amplitude per frame (Fig. 4.8C). Based on the results, it is clear that the PFHnD-Ab can be used as molecularly targeted contrast agents for ultrasound imaging.

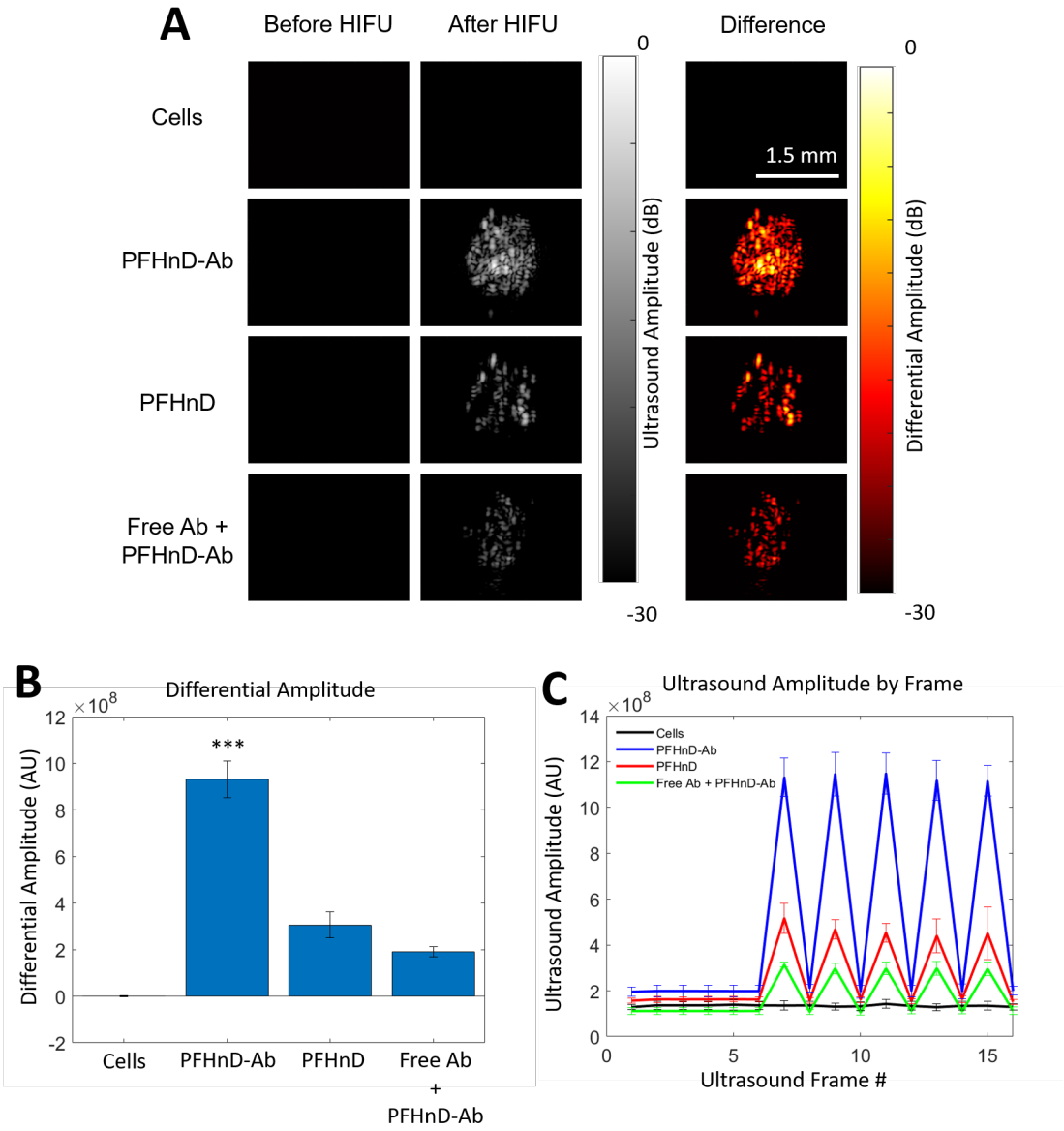

Figure 4.8: A)Ultrasound images of cells embedded in polyacrylamide tissue mimicking phantoms before and after the HIFU activation of the PFHnDs. The difference between the two images is displayed in the right panel, indicating PFHnD activation. Cells conjugated with the targeted droplets (PFHnD-Ab) were imaged along with the control groups; non-targeted droplets (PFHnD), blocking group (Free antibody and PFHnD-Ab) and FaDu cells without PFHnDs. B) The differential amplitude was calculated for each of the groups and resulted in the PFHnD-Ab group having a significantly higher differential amplitude ($p < 0.001$) than the other groups C) The average ultrasound amplitude within the focal spot for each ultrasound frame captured for each of the groups. The HIFU was pulsed prior to frames 7, 9, 11, 13 and 15, resulting in the ultrasound amplitude spike within those frames.
.

4.3.6 Determining the PFHnD-Ab detection limits

Cells with attached PFHnD-Ab were diluted 10×, 50×, 100×, and 500× and embedded in a thin layer of polyacrylamide phantoms matching the elevational thickness of the imaging transducer. The initial cell concentration was measured to be 2.12×10^5 cells/mL. The average number of cells in the HIFU focal zone was determined by dividing the cells in the phantom by the area of the focal zone, 3.83 mm^2. This resulted in 38.16, 7.63, 3.81, and 0.76 cells per focal area for the 10×, 50×, 100×, and 500× dilutions, respectively. The differential ultrasound amplitude was computed and spatially averaged for five focal spots for each dilution. Interestingly, the more diluted samples showed individual points of signal, indicating single-cell detection (Fig. 4.9A). The differential ultrasound signal was linearly proportional to the cell concentration, with an r^2 value of 0.998 (Fig 4.9B). This suggests that ultrasound imaging of PFHnD-Ab could be a highly sensitive method to detect small numbers of cells.

4.4 Discussion

The conjugation strategy employed in attaching the antibodies to the PFHnDs benefits from multiple key features. First, the aldehyde-hydrazide chemistry is a one-step procedure that does not require specialized linker molecules and can be carried out in biologically appropriate conditions. Second, the method could be adapted to virtually any IgG antibody with a glycosylated Fc region, opening the door to imaging an array of different molecular targets. Third, by binding the PFHnDs to the Fc region of the antibody, directional conjugation is achieved, likely reducing the number of antibodies required to achieve effective targeting.

A high-boiling-point perfluorocarbon was used in the core of the nanodroplets in this study. Thus, in biological applications, the nanodroplets recondense after undergoing ADV. This enables repeated activation and imaging of the same nanodroplets, opening the door

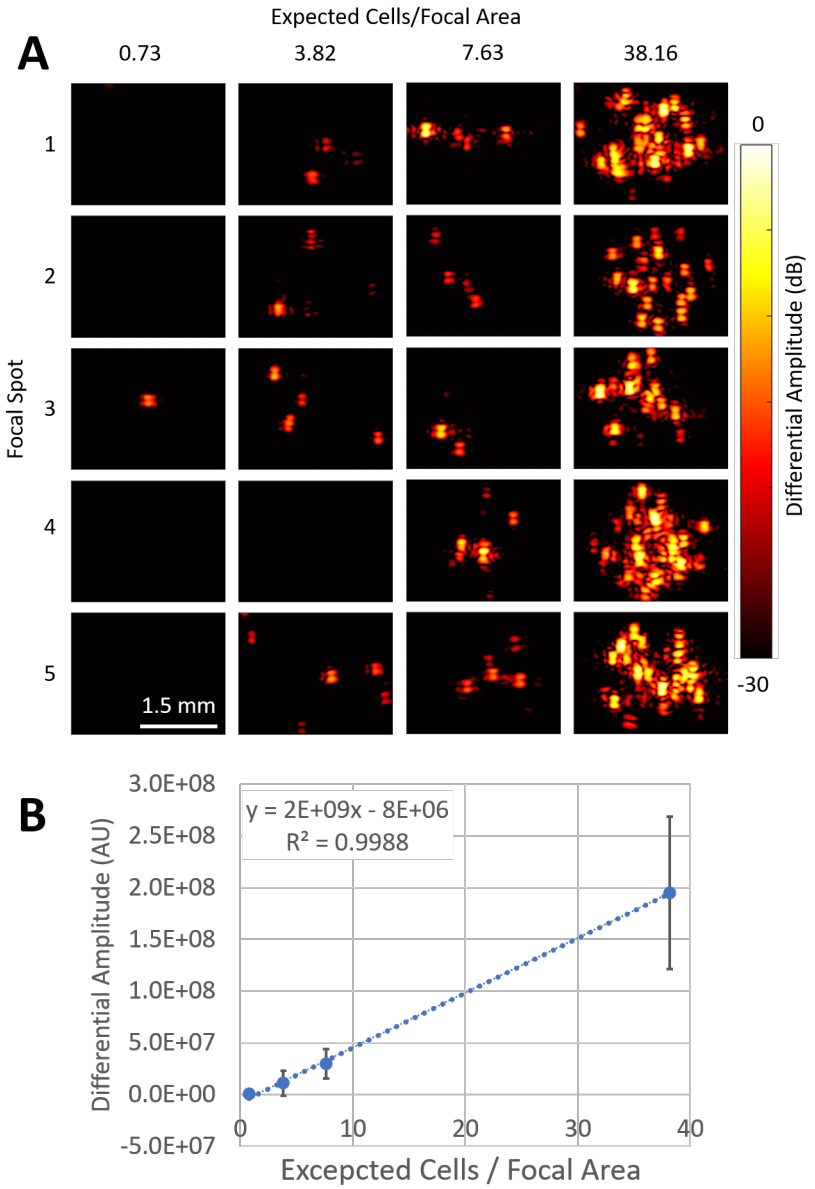

Figure 4.9: Cells with PFHnD-Abs attached to them were diluted to different concentrations and embedded into polyacrylamide phantoms. A) Images of the differential ultrasound amplitude for each of the different concentrations. The expected cells/focal area was calculated based on the initial concentration of cells. B) The differential amplitude plotted as a function of the expected cells/focal area yielded an r^2 of 0.998.

to improved contrast or super-resolution imaging [87, 59, 46]. Importantly, the results in this paper show that the PFHnD-Ab retain their molecular targeting capabilities even after undergoing 1000 vaporization/recondensation cycles. Furthermore, the PFHnDs remained bound to their targets even when the HIFU energy was applied after their incubation with cells. This suggests that the PFHnD-Abs have the promise to be robust *in-vivo* contrast agents for molecular ultrasound imaging.

The perfluorohexane core requires a relatively large amount of energy to initiate the vaporization. Previous studies have relied on the use of a pulsed laser for activation, which results in limited imaging depth [46, 59, 93]. The use of HIFU to activate the nanodroplets allows for deeper tissue activation [87]. The HIFU pressure levels used in this study were below the cavitation threshold, and no signs of cavitation were observed; however, the biological effects of HIFU in combination with PFHnDs has not yet been determined *in vivo*.

Importantly, the conjugation strategy does not rely on the use of perfluorohexane. It could be applied to the more volatile perfluoropentane (b.p. 28C) or perfluorobutane (b.p. 4C). These nanodroplets would require less energy for activation (i.e., a conventional imaging transducer could be used), but would only offer a single-time vaporization. Thus, more care would need to be taken to ensure binding in a region prior to imaging. An additional benefit of using a lower-boiling-point core is the ability to release cargo on demand. Therefore, the nanodroplets could be used for molecularly targeted drug delivery with ultrasound image guidance [80, 94, 95].

4.5 Conclusion

In this study, we have presented a new directional antibody conjugation strategy to confer molecular specificity to PFHnDs. The conjugation of EGFR antibodies promoted strong association with EGFR-overexpressing FaDu cells with minimal nonspecific binding. We

also demonstrated that the particles bound to cells could be imaged with a linear array ultrasound transducer after using HIFU to activate the PFHnDs. These findings show that the PFHnD-Ab are a robust contrast agent that could be applied to a wide variety of molecular imaging applications. While it was shown that the particles improve contrast, the size of the nanodroplets could be of concern for clinical translatability. Further studies are needed *in-vivo* to determine the clinical feasibility.

While specific targeting was shown on using the PFHnD-Abs, one additional control experiment should be carried out to ensure that the cellular binding is due to the antibody-receptor binding. Conjugating isotype control antibodies onto the surface of the PFHnDs as a control would be a way to fully prove specific antibody binding.

While it was shown that the targeted PFHnD-Abs can improve ultrasound contrast, the size of the particles can be further optimized to reduce the diameter. A size characterization study should be carried out modulating three factors, the DSPE-PEG:DPPC ratios, the sonication intensity and the centrifugation wash steps. The use of an extruder helps in reducing the size of the particles to the size of the filter. We have used a 0.4 μm filter membrane before which has resulted in nanodroplets in the 400 nm rang, however the extruder was not used with droplets with antibodies. Experimenting to see the effect of extruding on the surface antibody conjugation would be worthwhile. Other filter membrane sizes have not been tested and could result in smaller particles.

Chapter 5

Multiplexing using paired agent PFCnDs for metastatic lymph node detection

5.1 Introduction

Perfluorocarbon nanodroplets (PFCnDs) have been shown to be versatile contrast agents and have been used in both photoacoustic and ultrasound imaging due to their phase change properties. Upon activation with either a laser or ultrasound pulse, the liquid perfluorocarbon core undergoes a phase change into a gaseous microbubble, providing contrast on demand. The choice of perfluorocarbon core results in different varporization thresholds, with higher boiling point cores being able to recondense back into a liquid nanodroplet from a gaseous microbubble. The sub-micron size of the nanodroplets allows for molecular imaging or extravascular tissue [58]. PFCnDs have also been shown to be used as both imaging contrast agents and drug delivery vehicles, releasing the payload and providing contrast upon delivery [80]. We have shown in earlier chapters that PFCnDs can be conjugated into antibodies for molecular targeting applications as well. While there have been many diagnostic and therapeutic applications of PFCnDs, combining the effects for multiplexed strategies has yet to be fully explored. Santiesteban et. al have shown opti-

cal multiplexing by mixing two different perfluoropentane (PFP) nanodroplets, each with a different optical dye. They were able to selectively activate the nanodroplets based on the optical wavelength of the respective dye in the nanodroplet cocktail [96]. Multiplexing potentially opens the doors to new therapeutic strategies, for example, one nanodroplet can be used as a feedback loop to confirm the nanodroplets reached the target site before activating the other nanodroplet to deliver the payload.

5.1.1 Paired agent imaging

While multiplex imaging has shown potential for augmenting optical and ultrasound imaging, one of the challenges for multiplex targeting is determining specific targeting vs non specific targeting *in-vivo*. Paired-agent fluorescence imaging has shown to alleviate this issue by co-administering a non-targeted control imaging agent with a molecular targeted imaging agent to allow for non-specific uptake correction [97, 98]. It is assumed that the kinetics of the control and targeted paired agents is the same *in-vivo* and differences within the fluorescence would indicate targeting [97]. Molecular imaging of lymph nodes has been challenged with non specific effects, paired agent imaging has shown the ability to quantitatively identify cancerous tissue by eliminating the non-targeted fluorescence ultimately enhancing the targeted agent fluorescence to tumor contrast, providing better information [99].

While paired agent imaging has shown to be able to detect metastatic lymph nodes accurately, since it based on fluorescence, the depth penetration is a limitation. Optical imaging multiplexing is also faced with depth limitations. Acoustically activated PFCnDs allow for deeper tissue penetration compared to fluorescent imaging and optical imaging. We have shown that we can successfully target PFHnDs to EGFR overexpressing cells and visualize them using ultrasound *in-vitro*. However, non-specific binding was also noticed in the *in-vitro* studies, highlighing a need for a better visualization strategy before translating to *in-vivo*.

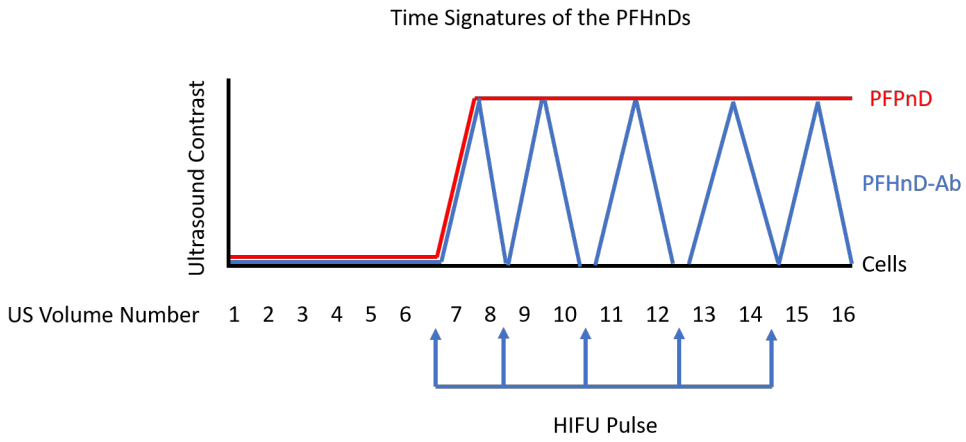

Figure 5.1: The two PFCnDs can be differentiated based on their time signature. Since PFP has a lower boiling point than body temperature, (b.p. 29 °C), once activated, the liquid nanodroplet stays as a gaseous microbubble producing prolonged ultrasound contrast. In comparison, PFH has a higher boiling point that body temperature (b.p. 56 °C), resulting in a vaporization-recondensation cycle that can be activated multiple times. Recondensation occurs on an order of milliseconds. These different time signatures can be used to distinguish between the two nanodroplets.

In this chapter, we describe methods of applying the paired agent imaging strategy for acoustically activated PFCnDs for metastatic lymph node detection. Two different PFCnDs were developed, one with a perfluoropentane (PFP, b.p. 29 °C) core, and one with a perfluorohexane (PFH, b.p. 56 °C) core, where the PFP nanodroplet serves as the non targeted control and the PFH nanodroplet is the molecularly targeted agent. Each of the nanodroplets was assigned a different fluorophore to allow for fluorescent paired agent imaging as a validation technique.

We have shown previously in our lab to be able to distinguish between the two nanodroplets based on their ultrasound time signature. Since the boiling point of PFP is below the body temperature (37 °C), once activated the PFP nanodroplets will stay in their microbubble state. PFH nanodroplets in comparison have a boiling point above the body temperature and exhibit a recondensation behavior after activation. The timescale of activation and recondensation of PFH nanodroplets is on the order of milliseconds [46], allowing for repeated activation. With the proper activation sequence, the difference in time signatures

can be used to distinguish between PFP and PFH nanodroplets.

5.2 Methods

5.2.1 Development and characterization of paired imaging agents

The two paired agent PFCnDs were synthesized using a modified sonication-based method described in Hannah, et al. [59] as described in the previous chapter. The targeting nanodroplet (PFHnD) was contained a perfluorohexane core with a lipid shell consisting of of a 1:0.2:0.03 molar ratio of DSPE-PEG-2k, DPPC and DSPE-PEG-Hz. Antibodies were conjugated to the surface of the PFHnDs using the same methods described in chapter 4. The antibodies were modified using 100 mM sodium periodate resulting in available aldehyde groups on the Fc region to bind to the hydrazide on the surface of the PFHnD. For cell studies, DiD (Biotium, San Francisco, CA, USA), a lipophillic near infrared dye was embedded into the lipid shell. For *in-vivo* fluorescence studies, a lipophillic near infrared dye, DiR (Biotium, San Francisco, CA, USA) was embedded into the PFHnD-Ab. The choice of dye for the different studies were determined by the fluorescence capabilities of the instruments used in the studies.

The non-targeted paired agent (PFPnD) has a perfluoropentane core encapuslated in a lipid shell consisting of 1:0.2:0.03 molar ratio of DSPE-PEG-2k, DPPC and DSPE-PEG-Cy5.5 (for *in-vivo* studies) or DSPE-PEG-FITC (for *in-vitro* studies). The fluorescent lipid was chosen for studies depending on the fluorescent capabilities of the instruments used in the study. The synthesis was identical to the PFHnDs aside from the difference in lipid shell composition. Size characterization was performed using dynamic light scattering (Zetasizer Nano ZS, Malvern Panalytical, UK). The nanodroplet concentrations were calculated using the concentration tools (Zetasizer Software, Malvern Panalytical, UK) based on the nanodroplet size.

5.2.2 *In-vitro* assessment of paired imaging agents

To assess the multiplexing capabilities of the paired imaging agents, cell studies were performed and validated using fluorescence microscopy using the same methods described in chapter 4. FaDu cells (ATCC) were used as the *in-vitro* model of head and neck squamous cell carcinoma due to their over-expression of EGFR on the surface, enabling molecular targeting via the anti-EGFR antibody. The cells were cultured in T-75 flasks by using Dulbecco's Modified Eagle's Medium (DMEM; Corning, Tewksbury, MA, USA) supplemented with 10% fetal bovine serum (Gibco - Thermo Fisher, Waltham, MA, USA) and 1% penicillin (Corning, Tewksbury, MA, USA). FaDu cells were suspended in 2 mL of DMEM for a final concentration of 4.42×10^5 cells/mL for use in experiments. Then, 200 μL of the cell solution was treated with a 9:10 ratio between PFHnD-Ab and PFPnD nanodroplets (total 150 μL) with concentrations of 4.76×10^7 nanodroplets/μL (PFHnd-Ab) and 4.31×10^7 nanodroplets/μL (PFPnD) and incubated for 30 minutes at 36 °C. Two additional groups were used as controls to investigate the individual nanodroplet effects on cell targeting. 200 μL cells were incubated with 100 μL of PFPnDs (4.31×10^7 nanodroplets/μL), and 200 μL of cells were incubated with 90 μL of PFHnD-Abs (4.76×10^7 nanodroplets/μL) to keep the concentrations consistent.

Fluorescent microscopy was used to visualize the cell and nanodroplet interactions. The different groups were imaged fluorescently using both the DiD and FITC channel along with a dark field image for reference. The cellular fluorescence was determined by segmenting the cells in the dark field image and calculating the fluorescence within the segmented cell regions in the respective fluorescence images.

5.2.3 *In-vivo* tumor model

All of the animal studies were performed after receiving approval from the Dartmouth institutional animal care and use committee (IACUC). Head and neck squamous cell carcinoma (HNSCC) FaDu cells were inoculated at in the oral cavity of immunodeficient six week old

female nu/nu mice. Approximately 500,000 cells were inoculated into the tongue of the mouse and were allowed to grow until forming a diameter of 3-4 mm, with the intent of developing metastases in the lymph nodes. Prior to any imaging, the mice were anesthetized using a combination of isoflurane (2.5%) and O_2 (1 L/min).

After imaging studies were performed, the mice were euthanized using an overdose of isoflurane (5%) and cervical dislocation. For mice containing tumors, the lymph nodes were excised and fixed in 10% formalin for 24-48 hours, then transferred into ethanol. The fixed tissue was sent to pathology to be embedded in paraffin and sliced in 200 μm levels. Each slice was stained using hematoxylin-eosin to identify micro-metastases.

5.2.4 Fluorescent imaging studies

Upon tumor formation, a 30 μL of a 1:1 ratio of PFHnD and PFPnD were injected into the tongue of the mouse and were allowed to drain into the lymph nodes for 4 hours. The lymph nodes were imaged using a small animal fluorescence imaging system (Pearl Trilogy, LI-COR, Lincoln, Nebraska, USA) using two channels, 700 nm and 800 nm. The PFPnD was imaged using the 700 nm channel corresponding to the excitation of Cy5.5, while the DiR dye fluorescence in the PFHnDs corresponded to the 800 nm channel. To correct for background signals, both vials of nanodroplets were imaged individually and the 1:1 mix was also imaged prior to injecting into mice.

5.2.5 Ratiometric quantification of fluorescent images

The ratiometric quantification approach was adopted from paired agent imaging [98]. Using the fluorescent image of the mixed particles, the maximum intensity of the 1:1 mix in each channel was computed and the normalization factor was determined. The 700 nm image corresponds to the PFPnDs and the 800 nm channel corresponds to the PFHnD-Abs. The fluorescent images (700 nm and 800 nm) of the nodes were then filtered using a 5 by 5 pixel 2D median filter to smooth the background noise in MATLAB. Each fluorescent

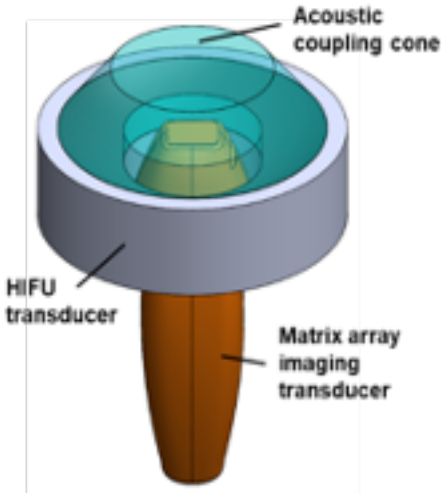

Figure 5.2: Schematic of the 1024 element matrix array ultrasound transducer co-linearly aligned with the high intensity focused ultrasound transducer (HIFU). A polyacrylamide coupling cone was used to ensure good contact between the imaging setup and the lymph node. Figure courtesy of Dr. Austin Van Namen.

image was then normalized to the maximum value within the respective image. The ratio between the 800 nm (PFHnD - targeting) and 700 nm (PFPnD non-targeted) images for each pixel were computed and adjusted using the normalization factor if above a threshold. The ratiometric values were then overlaid on top of the mouse for visualization.

5.2.6 Ratiometric imaging of lymph nodes using 3D matrix array ultrasound

After fluorescence imaging, the lymph nodes were imaged using a 1024 element 32 x 32 matrix array 3D ultrasound transducer. A high intensity focused ultrasound (HIFU) transducer (H-300 series, 150 mm diameter with a 41 mm opening, Sonic Concepts, Bothell, WA, USA) was used to activate the nanodroplets. The HIFU transducer has a 41 mm opening within the center allowing for co-linear alignment of the HIFU and matrix array transducer. The PFCnDs were activated using the HIFU transducer and the image was formed using the matrix array transducer.

A function generator was used to manually trigger the activation and imaging acquisi-

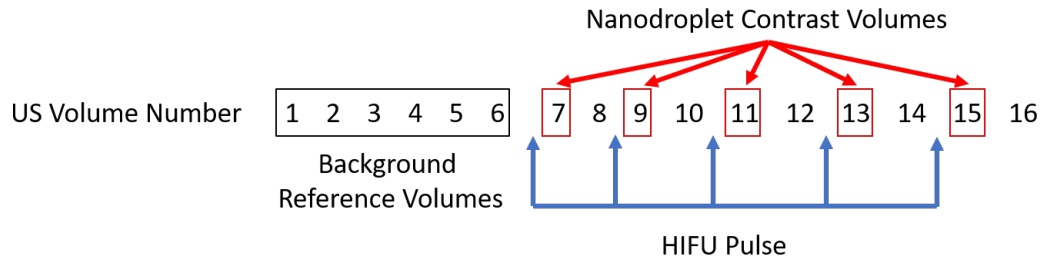

Figure 5.3: The imaging acquisition sequence of the lymph nodes resulted in a total of 16 volumes. The first 6 volumes were used as background reference volumes, followed by a HIFU pulse to activate the PFCnDs after the 6th volume. The PFCnD contrast would appear in volume 7. The second HIFU pulse was triggered after the 8th volume following the same pattern until the 14th volume. The total PFCnD signal from the volumes was determined by taking the mean between volume 7 and 16, then subtracting from the mean of the background reference volumes. The PFHnD-Ab signal was isolated from volumes 9, 11, 13 and 15, due to the vaporization-recondensation effect. The PFPnD signal was isolated by subtracting the PFHnD-Ab signal from the total PFCnD signal.

tion. The HIFU transducer activation waveform was a sine wave with a frequency 515 kHz and an amplitude of 280 mVrms. For each trigger, a total of 16 volumes were captured. The first 6 volumes were used to average the background signal, followed by 5 HIFU pulses within the 10 subsequent recording volumes (Figure 5.3). The total PFCnD signal from the volumes was determined by taking the mean between volume 7 and 16, then subtracting from the mean of the background reference volumes. The PFHnD-Ab signal was isolated from volumes 9, 11, 13 and 15, due to the vaporization-recondensation effect. The PFPnD signal was isolated by subtracting the PFHnD-Ab signal from the total PFCnD signal.

After the first HIFU activation pulse, it is assumed that both the PFPnD and the PFHnD-Abs will both be activated and produce ultrasound contrast (volume 7) and the PFHnD-Abs will recondense back into a liquid nanodroplet eliminating its ultrasound contrast until the next HIFU pulse (volume 9), however the PFPnD contrast will remain constant through the subsequent volumes. After isolating the respective PFCnD signal from the volumes, a pixel by pixel ratio calculation was performed between the PFHnD-Ab and PFPnDs and overlaid on top of the ultrasound image.

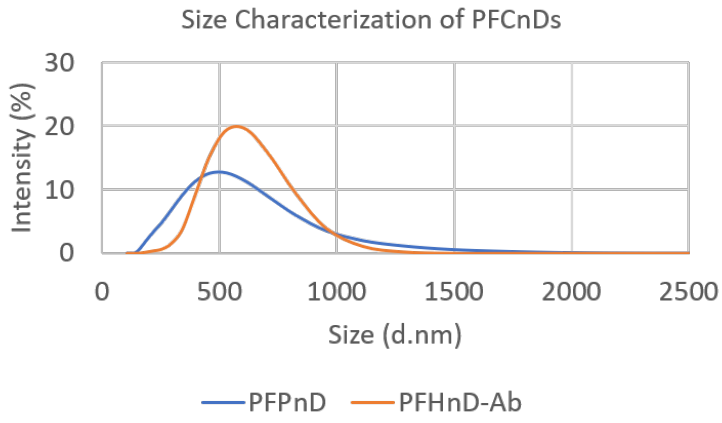

Figure 5.4: The size distribution of both paired agents PFPnD (500 ±20 nm; n=3) and antibody conjugated PFHnD-Ab (680 ±7 nm; n=3)

5.3 Results

5.3.1 Size characterization of PFHnDs and PFPnDs

The size distribution of both paired agents PFPnD (500 ±20 nm; n=3) and antibody conjugated PFHnD-Ab (680 ±7 nm; n=3). The nanodroplet concentrations were determined using the concentration calculators in the Malvern Zetasizer software. The concentration of the PFPnDs was determined to be 4.31×10^7 nanodroplets/µL and 4.76×10^7 nanodroplets/µL for the PFHnD-Abs.

5.3.2 Fluorescence imaging of PFCnDs *in-vitro*

To determine the binding specificity of the PFHnD-Abs and the PFPnDs were fluorescently tagged with DiD and FITC respectively. Both nanodroplets were mixed together with HNSCC FaDu cells and were incubated for 30 minutes. As controls, the nanodroplets were individually also allowed to incubate with FaDu cells. Each of the groups were imaged using a fluorescence microscope in the dark field, DiD and FITC channels.

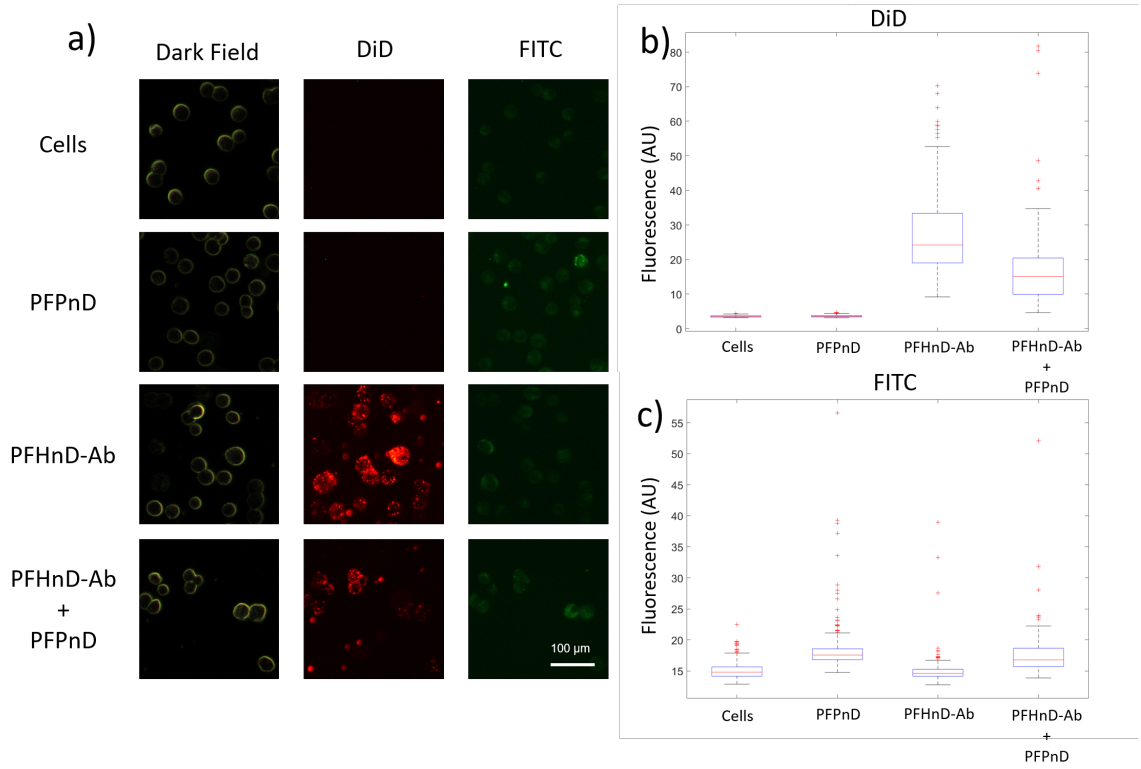

Figure 5.5: Both nanodroplets, PFHnD-Abs and PFPnDs were mixed together with FaDu cells to evaluate specific binding. After washing the unbound nanodroplets, it was determined that the PFHnD-Abs were selectively bound to the cells, while the PFPnDs were washed out as confirmed by fluorescence microscopy (a). The fluorescent intensity per cell was determined for each group for the two different fluorescent channels. The FITC fluorescence was low as expected, due to the unbound PFPnDs washing out.

5.3.3 Ratiometric imaging of lymph nodes using fluorescence

An *in-vivo* orthotopic mouse model was used to evaluate paired agent imaging of the two ultrasound contrast imaging agents. The non-targeted PFPnDs (700 nm) and targeted PFHnD-Abs (800 nm) were administered together in the tongue and were allowed to drain into the lymph nodes for 4 hours. The ratio between the two fluorescent channels was corrected with the normalization factor computed using a fluorescent image of both of the nanodroplets mixed together. As a control, the same study was done using mice without tumors.

Mice containing tumors did not show ratiometric accumulation of the PFHnD-Abs in the lymph nodes after correcting with the normalization factor, however there was accumulation of the targeted nanodroplets in the drainage pathway to the lymph nodes (Figure 5.6(f)). The control mice did not show any ratiometric accumulation of the PFHnD-Abs. Histological analysis of the lymph nodes determined that the lymph nodes were not metastatic in the tumor model.

5.3.4 Ratiometric imaging of lymph nodes using ultrasound

After fluorescence imaging of the mice for 4 hours, the lymph nodes were imaged using the custom HIFU 3D matrix array ultrasound imaging system. The PFH and PFP signals were isolated from the ultrasound volumes and the ratio between PFH and PFP were calculate for each pixel and the ratiometric values were overlaid on top of the ultrasound image. For pixels with a ratio of 1, indicating that the pixel contained a PFHnD-Ab, the ultrasound time signature showed repeated vaporization (Figure 5.7). For pixels with a ratio less 1, indicating a mix of PFP and PFH nanodroplets, the ultrasound time signature initially showed an increase in the baseline signal after the first pulse, followed by a repeated vaporization time signature (Figure 5.8).

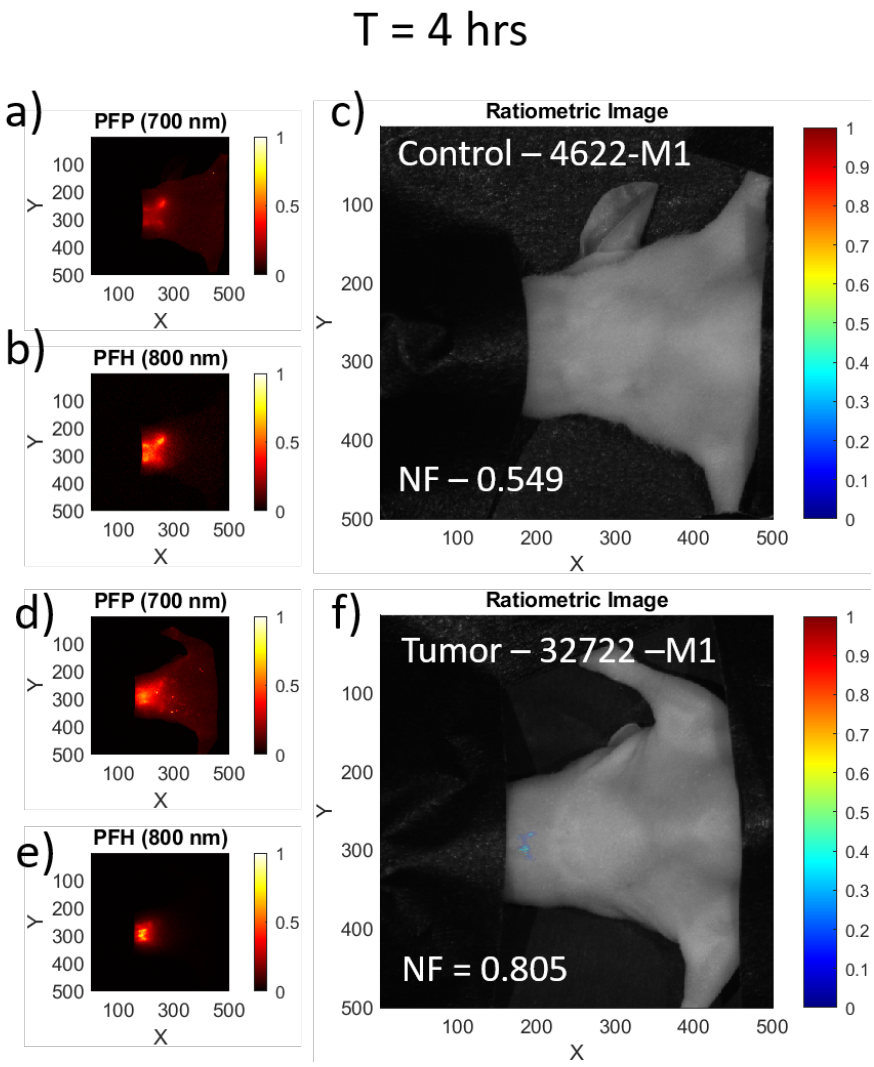

Figure 5.6: A cocktail of non-targeted PFPnDs (700 nm) and targeted PFHnD-Abs (800 nm) were injected into the tongue of the mouse and allowed to drain into the lymph nodes for 4 hours. Fluorescent images were acquired in both the 700 nm and 800 nm channels and the pixel wise ratio between the two channels was computed and corrected using the normalization factor (NF). a-b) are the fluorescent images from the 700 nm and 800 nm channels for a control mouse, and the ratiometric image is displayed in c). d-e) are the fluorescent images from a mouse with an orthotopic tongue tumor model, and f) is the corresponding ratiometric image corrected using the normalization factor. A slightly higher PFHnD-Ab signal was observed in the tumor mouse in the drainage pathway to the lymph nodes. Histology confirmed that the lymph nodes were not metastatic.

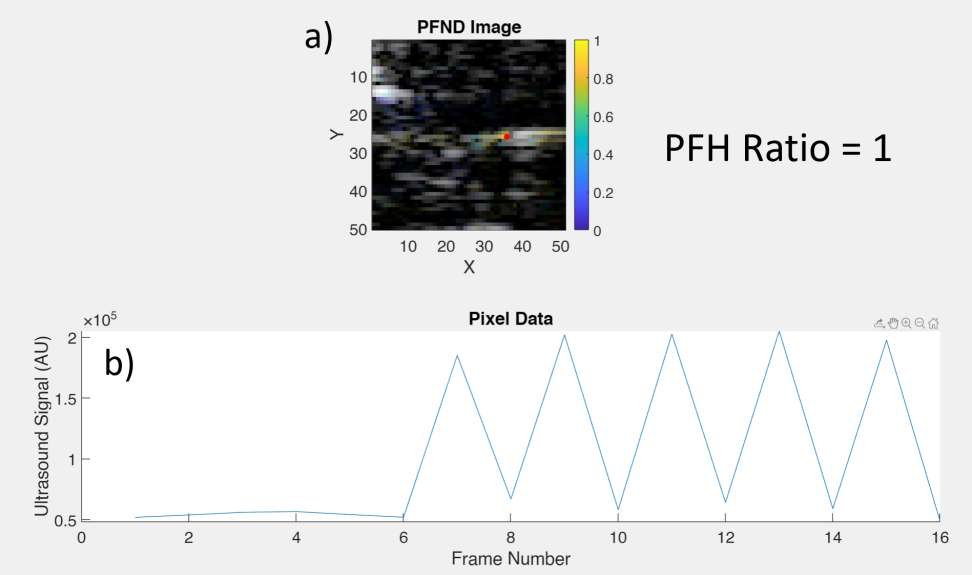

Figure 5.7: a) A differential ultrasound slice of the ultrasound volume in the x-z plane of a lymph node. The selected pixel (red dot) indicated a ratio between PFH and PFP of 1. b) the ultrasound time signature resembles that PFH, indicated by the increased ultrasound signal after each HIFU pulse (frames 7,9,11,13,15) showing repeated vaporization.

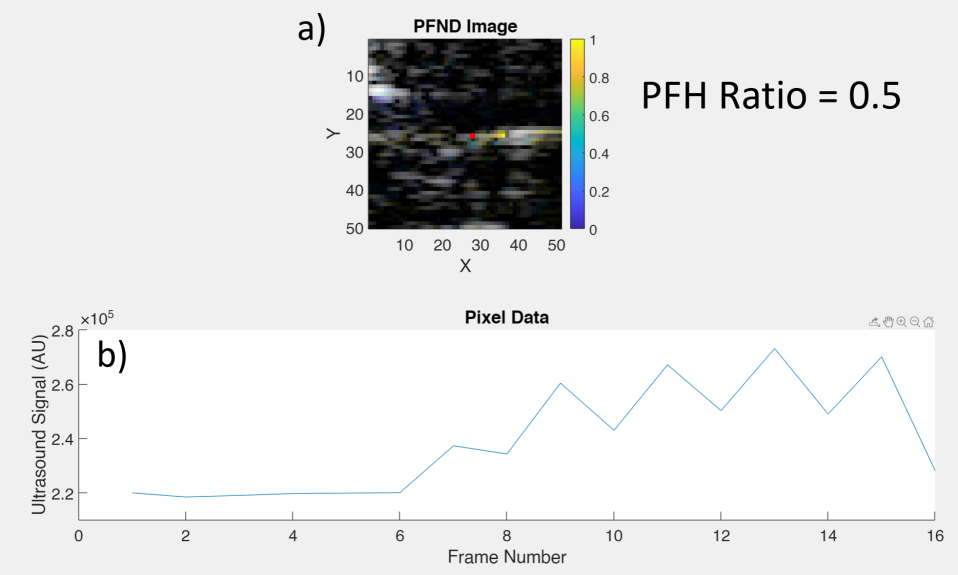

Figure 5.8: a) A differential ultrasound slice of the ultrasound volume in the x-z plane of a lymph node. The selected pixel (red dot) indicated a ratio between PFH and PFP of 0.5. b) the ultrasound time signature resembles a combination of both PFP and PFH, indicated by the increased ultrasound signal baseline after the first HIFU pulse (frame 7). The overall ultrasound signal increases after each HIFU pulse (frames 7,9,11,13,15) showing repeated vaporization of the PFH, but the recondensation is signal magnitude is set to the new baseline compared to in Figure 5.7.

5.4 Discussion

The use of a paired agent imaging approach for multiplexing perfluorocarbon core nanodroplets to improve ultrasound contrast in-vivo and reliably detect metastasis shows promise. Ratiometric imaging allows for relative quantification between the two paired agent, allowing for better insight. Both nanodroplets, the targeted PFHnD-Abs and the non-targeted PFPnDs, exhibited high fluorescence signal in the small animal fluorescence images, but when ratiometrically compared, no specific targeting was observed. Without the non-targeted agent, the fluorescent signal from the targeted droplet would have been misleading. By using a normalization factor, the initial fluorescence intensities for the two channels are not binding, (i.e if one agent has a stronger signal than the other, it can be corrected). However, a limitation in the normalization factor approach is that the factor is calculated using the nanodroplet mix, but is applied to signals *in-vivo* and does not account for tissue attenuation. None of the lymph nodes from the mice subjected to tumors were determined metastatic when validated by histology, explaining the lack of ratiometric signal within the lymph nodes. However, the ratiometric signal observed in the drainage pathway shows promise. Further studies need to be performed with a metastatic mouse model to truly validate selective binding using the nanodroplets and fluorescence paired agent approach.

The ultimate goal of this chapter was to assess if the paired agent approach could be adopted for paired agent ultrasound imaging to enable multiplexing. While the targeted PFHnD-Ab nanodroplets were hypothesized to selectively attach to the metastatic lymph nodes, imaging the nodes using the developed 3D matrix array ultrasound system still showed signs of being able to differentiate between the PFH and PFP nanodroplets based on the time signature. The time series differentiation between the two particles was shown in two pixels within a node as a proof of concept, but further assessment is needed. With metastatic lymph nodes, it is hypothesized that there would be a higher accumulation of PFHnD-Abs in the lymph node, leading to ratiometric visualization of the node and confirmed by the time signature. However, the time signature from pixels with a ratio of 0.5

show promise to be able to use the imaging system with multiplex imaging. There are many perfluorocarbon based nanodroplets for different applications such as drug delivery [80, 94, 95] that rely on optical activation, which is limited by tissue attenuation and depth penetration. The use of this system would allow for deeper activation and imaging. The use of a targeted nanodroplet and non-targeted nanodroplet can open doors to selective targeting for diagnosis followed by one time activation for drug delivery using the different nanodroplets.

5.5 Conclusions

In this chapter, the use of paired agent imaging using two ultrasound contrast agents, one molecularly targeted and one non-targeted, were explored for multiplexing applications. By exploiting the the difference in perfluorocarbon core boiling points, differentiation between the two nanodroplets *in-vivo* was demonstrated based on their unique time signatures. Fluorescence imaging was used to validate selective binding and the paired agent approach *in-vivo*. While none of the lymph nodes in the tumor mice were proven to be metastatic, the ratiometric imaging showed selective targeting within the lymph node drainage pathway, showing promise to be able to image metastatic lymph nodes. The normalization factor in the ratiometric images was determined based on the fluorescent image of vial containing a mix of both of the particles, however, this can lead to errors due to the difference in fluorescent attenuation *in-vivo* and *in-situ*. To correct of this, picking a spot in the *in-vivo* images where the drainage between both particles is expected to be same would result in a more accurate normalization factor. An alternative strategy is to inject a small volume of the mixture of both particles subcutaneously in the arm or leg to create an *in-vivo* reference signal to determine the normalization factor.

Chapter 6

Conclusions and Future Directions

6.1 Conclusions

The purpose of this thesis was to combine the specificity of molecular imaging with the functionality of ultrasound and photoacoustic imaging through the use of nanodroplets for metastatic lymph node detection in head and neck squamous cell carcinomas (HNSCC). The lymph node metastatic state is used in staging and treatment planning highlighting the need for accurate detection. Metastatic lymph nodes have irregular vasculature leading to differences in blood oxygen saturation compared to healthy lymph nodes [28]. Additionally, metastatic lymph nodes have shown to over express EGFR, making it a great target for molecular imaging [100].

6.1.1 Ultrasound photoacoustic imaging system and deep learning neural network for blood oximetry

In this thesis, an ultrasound photoacoustic imaging system to estimate blood oxygen saturation (sO_2) was developed. The USPA system can also be used with exogenous contrast agents for nanodroplet molecular imaging as well. It was shown that the USPA system could accurately estimate sO_2 (r^2 = 0.95) by modulating bovine blood with CO_2 and O_2.

The ground truth sO_2 was measured using a optical reflectance probe. While photoacoustic imaging is able to estimate blood oxygen saturation, the estimations are based on assumptions leading to errors in estimates calculated by linear unmixing. Another limitation is light attenuation in tissue leading to inaccurate estimations deeper in tissue. To correct for this, a deep learning model, O-Net, was developed that can segment and estimate sO_2 from photoacoustic images from two wavelengths. The model was trained on Monte Carlo simulated data using a custom loss function that only optimized the sO_2 within the blood vessels. The O-Net with the custom loss function outperformed the same model using the mean squared error (MSE) loss function, and the traditional linear unmixing approach. The O-Net also showed that it was capable of estimating sO_2 from experimental photoacoustic images collected from our USPA system. The sO_2 estimation accuracy of the experimental data was was lower than the simulated data, but much better then linear unmixing using the same data. More experimental data is needed for better results.

6.1.2 Phase change perfluorocarbon nanodroplets for molecular imaging of lymph nodes

The USPA system is also capable of imaging phase change perfluorocarbon nanodroplet (PFCnDs) contrast agents. The perfluorocarbon core of the nanodroplets is encapsulated by a lipid shell that can be functionalized for molecular targeting applications. The contrast from the PFCnDs is only visible upon activation from an optical or acoustic stimulus to produce localized heating that induces a phase change of the PFC core from a liquid nanodroplet to a gaseous microbubble. The localized heating can be induced either optically by incorporating a dye within the nanodroplet (photoacoustics) or by the peak negative pressure (acoustic droplet vaporization). PFCnDs were developed with a perfluorohexane core with EGFR antibodies (PFHnD-Ab) functionalized on the surface through stable hydrazone bonds. EGFR antibodies were chosen due to EGFR over expression in HNSCCs. The PFHnD-Abs exhibited high molecular targeting to HNSCC (FaDu) cells compared to

non targeted perfluorohexane nanodroplets (PFHnDs) as confirmed by fluorescence microscopy. The PFHnD-Abs conjugated to cells also exhibited higher ultrasound contrast when imaged with a custom high intensity focused ultrasound (HIFU) imaging system. The high targeting efficiency and high ultrasound contrast from the PFHnD-Abs shows promise to be able to detect metastatic lymph nodes.

6.1.3 Multiplexing of PFCnDs using paired agent imaging for metastatic lymph node detection

The PFHnD-Ab nanodroplets developed showed high targeting levels and increased ultrasound contrast when attached to HSNCC cells. However some non specific binding of the non-targeted PFHnDs was evident. When translating to an *in-vivo* model, quantification of the contrast can be a challenge to determine the metastatic state. Paired agent imaging is a clever way of being able to ratiometrically quantify binding through the use of two different imaging agents together, one targeted and one non-targeted [97]. The premise is that since the flow kinetics are the same for both imaging agents, if a lymph node is metastatic, then the targeted agent will accumulate while the non targeted agent will continue to flow, leading to a high ratiometric difference between the signals from the two imaging agents [97]. The paired agent imaging strategy was adopted for contrast enhanced ultrasound by using two ultrasound phase change contrast agents, each with a different perfluorocarbon core. The PFHnD-Ab which was developed served as the targeting agents, while a perfluoropentane (PFP) core PFPnD was developed to used as the non targeted agent. The signal between the two nanodroplets can be distinguished based on their time signature matrix. The boiling point of PFP is below the body and room temperature, so once activated the PFP core stays as a gaseous microbubble. In comparison, perfluorohexane has a boiling point above body and room temperature, recondensing back into a liquid nanodroplet within milliseconds leading to a blinking effect [59]. While developing metastatic lymph nodes within mice has been a challenge, initial ultrasound imaging of the lymph

nodes were still able to detect ratiometric differences between the two nanodroplets. To our knowledge, paired agent imaging using ultrasound contrast agents and acoustic activation has not been done before, opening the door to ultrasound guided molecular imaging with multiplexing approach. While ultrasound imaging is the main focus of this work, we also showed that paired agent imaging using the same contrast agents could work in fluorescence imaging as well, if a fluorescent dye is embedded into the nanodroplet. Future experiments with a positive metastatic lymph nodes is needed to fully validate this concept, nonetheless, the results so far show promise for this new frontier.

6.2 Future Directions

6.2.1 USPA imaging system and O-Net

The USPA system and accompanying O-Net deep learning neural network showed ability to be able to estimate sO_2 in blood, however there is room for improvement in accuracy. The photoacoustic image quality can be improved with a higher frequency transducer, but at a trade off of depth penetration. Depending on the application, a higher frequency transducer could be preferred. Training the O-Net on more experimentally acquired data will improve its performance and sO_2 estimation. The current model is trained on Monte Carlo simulated data that assumes that the sO_2 of the blood vessel is uniform throughout, whereas *in-vivo* that is not the case and the sO_2 follows more of a Gaussian distribution. Generating new Monte Carlo data with Gaussian sO_2 distributions within the vessels for model training would be needed. Secondly, the experimental data used to train the model contained only two vessel orientations. Collecting more experimental data with different vessel depths, and including epidermis and dermis layers on top could aid in training the model.

While the primary focus of the imaging system is sO_2 estimation, the use of PFCnDs in blood can augment the images and introduce super-resolution imaging [46]. Combining the USPA imaging system with the PFHnD-Abs and super resolution imaging could

improve the image quality and resolution in imaging lymph nodes. Additionally, photoacoustic images with nanodroplets and blood could be used to train the O-Net for further classification. The computational speed of the O-Net shows promise for real time imaging and processing. Connecting the image acquisition algorithms with the O-Net for real time image processing still needs to be explored.

6.2.2 Ultrasound molecular imaging using PFCnDs

The antibody conjugated PFHnDs showed great targeting efficiency to HNSCC cells. The nanodroplets developed were targeted to EGFR, due to it's overexpression in FaDu cells, but the same antibody nanodroplet conjugation can be employed for other IgG antibodies as well, introducing a molecular contrast targeting strategy rather than a molecular contrast agent. Creating a suite of PFHnDs all conjugated to different targets can expand this imaging method to other cancers such breast. Since ultrasound is used to activate the nanodroplets, deeper tissues can also be imaged. The targeted nanodroplets can also be used for super resolution imaging with acoustic activation instead of optical.

While the improved contrast has been shown, the size of the nanodroplets could be of concern. The smaller the nanodroplet diameter, the higher probability of reaching the target site. The size of the nanodroplets can be reduced by optimizing the following; DSPE-PEG:DPPC lipid ratios in the lipid cake step, the probe tip sonication energy and time, the centrifugation settings used in washing out the larger particles and finally by using an extruder with a pore size filter. It was shown that the ratio between lipids plays a role in the size of the resulting PFCnD [101]. The sonication methods currently used include an initial longer low power sonication (1 % amplitude, 1 sec on, 5 seconds off) followed by a quick high power sonication (50 % amplitude, 1 sec on, 10 seconds off) which was adapted from [101]. Experimenting with the sonication settings to see the effects on size uniformity would be interesting. Lastly, the centrifugation steps currently used are aimed to remove the big particles from the solution and only keep the smaller ones. Further optimization

of this step could result in smaller particles. Spinning down the supernatant from the last centrifuge step could yield smaller particles, but at a trade off of a lower concentration. Performing a DLS size measurement of the supernatant would provide information on the size of the particles left over. Lastly, using an extruder will help in obtaining monodisperse particles. A 0.4 μm pore filter has been used before and resulted in nanodroplets in the 400 nm range, but extrusion was not applied to particles with conjugated antibodies. It would be interesting to see the effects of extrusion on the surface conjugation of antibodies. Reducing the size of the nanodroplets will be important when translating to *in-vivo* studies.

While specific targeting was shown on using the PFHnD-Abs, one additional control experiment should be carried out to ensure that the cellular binding is due to the antibody-receptor binding. Conjugating isotype control antibodies onto the surface of the PFHnDs as a control would be a way to fully prove specific antibody binding. An alternative would be to incubate the PFHnD-Abs with an EGFR-negative cell line, we would expect to not see any binding.

6.2.3 Paired agent imaging of PFCnDs for multiplexing applications

The natural next step after developing many different molecular targeting PFCnDs, is to use them in tandem. Paired agent imaging allows for a method to validate and quantify delivery, but with the use of different PFC cores in the nanodroplets, the activation thresholds can also be modulated to selectively activate only a subset of PFCnDs for true multiplexing. Combinatory strategies could then be employed, for example, one nanodroplet can be used to break open vasculature or the blood brain barrier, while a second nanodroplet could be used as drug delivery mechanism, all while providing ultrasound contrast and imaging feedback allowing the whole setup to be a diagnostic/theranostic imaging tool. Drug delivery using PFC nanodroplets has been explored extensively [80, 95, 94], however they rely on optical activation for the release and imaging. Depending on the PFC core used in those studies, existing nanodroplets should be able to interface with the imaging setup developed.

While the fluorescent imaging of the paired agents serves as a validation metric, the experimental setup needs further optimization to be accurate. Firstly, the initial tumor seeding needs to be optimized to ensure that the primary tumor metastasized. Currently, the mice either produce large tumors at a really fast rate, or are not able to generate a primary tumor. Injecting three mice with three different initial seeding concentrations of cells would be a way to assess the perfect number of cells to inject into the primary tumor to develop metastasis. Secondly, the normalization factor currently used to correct for the fluorescent paired imaging is currently based on the fluorescent image of the mixed particles. This method does not take into account the fluorescent attenuation from the tissue and skin in the mouse. A better approach would be to choose a spot where the flow rate between both paired agents is expected to be the same, however we had difficulties identifying a place in the mouse that met that criteria. An alternative method would be to include a small subcutaneous injection of the paired agent mix in the arm or leg away from the lymph nodes and use that spot as the normalization factor.

The 3D matrix array - HIFU imaging system has shown capabilities in being able to differentiate between PFP and PFH nanodroplets using the ratiometric paired agent approach based off the ultrasound time signature, however the image quality and experimental setup could use improvement. The system is currently in its first iteration, further characterization is needed to determine the proper ratiometric thresholds and limitations of the system.

Overall, the combination of the antibody targeted ultrasound contrast agents, the paired agent multiplex imaging approach and the developed ultrasound system shows promise to be able to detect metastatic lymph nodes and augment to use of ultrasound in diagnostic and theranostic applications.

Bibliography

[1] Daniel E Johnson, Barbara Burtness, C RenÃ© Leemans, Vivian Wai Yan Lui, Julie E Bauman, and Jennifer R Grandis. Head and neck squamous cell carcinoma. *Nature Reviews Disease Primers*, 6(1):92, 2020.

[2] Joseph A Ludwig and John N Weinstein. Biomarkers in Cancer Staging, Prognosis and Treatment Selection. *Nature Reviews Cancer*, 5(11):845–856, 2005.

[3] Jatin P Shah. Staging for Head and Neck Cancer: Purpose, Process and Progress. *Indian journal of surgical oncology*, 9(1):116–120, 3 2018.

[4] Clint T Allen, Jonathan H Law, Gavin P Dunn, and Ravindra Uppaluri. Emerging insights into head and neck cancer metastasis. *Head & Neck*, 35(11):1669–1678, 11 2013.

[5] Jae-Keun Cho, Seung Hyup Hyun, Nayeon Choi, Min-Ji Kim, Timothy P Padera, Joon Young Choi, and Han-Sin Jeong. Significance of Lymph Node Metastasis in Cancer Dissemination of Head and Neck Cancer. *Translational Oncology*, 8(2):119–125, 2015.

[6] Nnamdi Eze, Ying-Chun Lo, and Barbara Burtness. Biomarker driven treatment of head and neck squamous cell cancer. *Cancers of the Head & Neck*, 2(1):6, 2017.

[7] Naveed Basheeth and Naishadh Patil. Biomarkers in Head and Neck Cancer an Update. *Indian journal of otolaryngology and head and neck surgery : official publication of the Association of Otolaryngologists of India*, 71(Suppl 1):1002–1011, 10 2019.

[8] Ping Wee and Zhixiang Wang. Epidermal Growth Factor Receptor Cell Proliferation Signaling Pathways. *Cancers*, 9(5):52, 5 2017.

[9] Reema Goel, William Moore, Baran Sumer, Saad Khan, David Sher, and Rathan M Subramaniam. Clinical Practice in PET/CT for the Management of Head and Neck Squamous Cell Cancer. *American Journal of Roentgenology*, 209(2):289–303, 7 2017.

[10] David G Pfister, Sharon Spencer, David Adelstein, Douglas Adkins, Yoshimi Anzai, David M Brizel, Justine Y Bruce, Paul M Busse, Jimmy J Caudell, Anthony J Cmelak, A Dimitrios Colevas, David W Eisele, Moon Fenton, Robert L Foote, Thomas

Galloway, Maura L Gillison, Robert I Haddad, Wesley L Hicks, Ying J Hitchcock, Antonio Jimeno, Debra Leizman, Ellie Maghami, Loren K Mell, Bharat B Mittal, Harlan A Pinto, John A Ridge, James W Rocco, Cristina P Rodriguez, Jatin P Shah, Randal S Weber, Gregory Weinstein, Matthew Witek, Frank Worden, Sue S Yom, Weining Zhen, Jennifer L Burns, and Susan D Darlow. Head and Neck Cancers, Version 2.2020, NCCN Clinical Practice Guidelines in Oncology. *Journal of the National Comprehensive Cancer Network J Natl Compr Canc Netw*, 18(7):873–898, 2020.

[11] Bogdan Popescu, Patricia Ene, Serban Vifor Gabriel Bertesteanu, Razvan Ene, Catalin Cirstoiu, and Cristian Radu Popescu. Methods of investigating metastatic lymph nodes in head and neck cancer. *Maedica*, 8(4):384–387, 9 2013.

[12] Philipp Heusch, Christoph Sproll, Christian Buchbender, Elena Rieser, Jan Terjung, Christina Antke, Inga Boeck, Stephan Macht, Axel Scherer, Gerald Antoch, Till A Heusner, and JÃ¶rg Handschel. Diagnostic accuracy of ultrasound, 18F-FDG-PET/CT, and fused 18F-FDG-PET-MR images with DWI for the detection of cervical lymph node metastases of HNSCC. *Clinical Oral Investigations*, 18(3):969–978, 2014.

[13] Chenzhou Wu, John Gleysteen, Nutte Tarn Teraphongphom, Yi Li, and Eben Rosenthal. In-vivo optical imaging in head and neck oncology: basic principles, clinical applications and future directions. *International Journal of Oral Science*, 10(2):10, 2018.

[14] Kyeong Hwa Ryu, Seokho Yoon, Hye Jin Baek, Tae Hoon Kim, Jin Il Moon, Bo Hwa Choi, Sung Eun Park, Ji Young Ha, Dae Hyun Song, Hyo Jung An, and Young Jin Heo. Cervical Lymph Nodes Detected by F-18 FDG PET/CT in Oncology Patients: Added Value of Subsequent Ultrasonography for Determining Nodal Metastasis. *Medicina (Kaunas, Lithuania)*, 56(1):16, 12 2019.

[15] Lacey J McIntosh, Alexander A Bankier, Gopal R Vijayaraghavan, Robert Licho, and Max P Rosen. COVID-19 Vaccination-Related Uptake on FDG PET/CT: An Emerging Dilemma and Suggestions for Management. *American Journal of Roentgenology*, 217(4):975–983, 3 2021.

[16] A T Ahuja, M Ying, S Y Ho, G Antonio, Y P Lee, A D King, and K T Wong. Ultrasound of malignant cervical lymph nodes. *Cancer imaging : the official publication of the International Cancer Imaging Society*, 8(1):48–56, 3 2008.

[17] R B J de Bondt, P J Nelemans, P A M Hofman, J W Casselman, B Kremer, J M A van Engelshoven, and R G H Beets-Tan. Detection of lymph node metastases in head and neck cancer: A meta-analysis comparing US, USgFNAC, CT and MR imaging. *European Journal of Radiology*, 64(2):266–272, 2007.

[18] P Vassallo, K Wernecke, N Roos, and P E Peters. Differentiation of benign from malignant superficial lymphadenopathy: the role of high-resolution US. *Radiology*, 183(1):215–220, 4 1992.

[19] Martin G Mack, JÃ¶rg Rieger, Mehran Baghi, Sotirios Bisdas, and Thomas J Vogl. Cervical lymph nodes. *European Journal of Radiology*, 66(3):493–500, 2008.

[20] Dae Young Yoon, Hee Sung Hwang, Suk Ki Chang, Young-Soo Rho, Hwoe Young Ahn, Jin Hwan Kim, and In Jae Lee. CT, MR, US, 18F-FDG PET/CT, and their combined use for the assessment of cervical lymph node metastases in squamous cell carcinoma of the head and neck. *European Radiology*, 19(3):634–642, 2009.

[21] Jeroen E van Schaik, Gyorgy B Halmos, Max J H Witjes, and Boudewijn E C Plaat. An overview of the current clinical status of optical imaging in head and neck cancer with a focus on Narrow Band imaging and fluorescence optical imaging. *Oral Oncology*, 121:105504, 2021.

[22] Stan van Keulen, Naoki Nishio, Shayan Fakurnejad, Andrew Birkeland, Brock A Martin, Guolan Lu, Quan Zhou, Stefania U Chirita, Tymour Forouzanfar, A Dimitrios Colevas, Nynke S van den Berg, and Eben L Rosenthal. The Clinical Application of Fluorescence-Guided Surgery in Head and Neck Cancer. *Journal of Nuclear Medicine*, 60(6):758 LP – 763, 6 2019.

[23] Naoki Nishio, Nynke S van den Berg, Stan van Keulen, Brock A Martin, Shayan Fakurnejad, Nutte Teraphongphom, Stefania U Chirita, Nicholas J Oberhelman, Guolan Lu, Crista E Horton, Michael J Kaplan, Vasu Divi, A Dimitrios Colevas, and Eben L Rosenthal. Optical molecular imaging can differentiate metastatic from benign lymph nodes in head and neck cancer. *Nature Communications*, 10(1):5044, 2019.

[24] Paul Beard. Biomedical photoacoustic imaging. *Interface Focus*, 1(4):602–631, 8 2011.

[25] Idan Steinberg, David M Huland, Ophir Vermesh, Hadas E Frostig, Willemieke S Tummers, and Sanjiv S Gambhir. Photoacoustic clinical imaging. *Photoacoustics*, 14:77–98, 6 2019.

[26] Geng Ku and Lihong V Wang. Deeply penetrating photoacoustic tomography in biological tissues enhanced with an optical contrast agent. *Optics letters*, 30(5):507–509, 3 2005.

[27] Thierry L. Lefebvre, Emma Brown, Lina Hacker, Thomas Else, Mariam-Eleni Oraiopoulou, Michal R. Tomaszewski, Rajesh Jena, and Sarah E. Bohndiek. The Potential of Photoacoustic Imaging in Radiation Oncology. *Frontiers in Oncology*, 12, 3 2022.

[28] Geoffrey P Luke and Stanislav Y Emelianov. Label-free Detection of Lymph Node Metastases with US-guided Functional Photoacoustic Imaging. *Radiology*, 277(2):435–442, 5 2015.

[29] Varvara Petrova, Margherita Annicchiarico-Petruzzelli, Gerry Melino, and Ivano Amelio. The hypoxic tumour microenvironment. *Oncogenesis*, 7(1):10, 2018.

[30] Geoffrey P Luke, Doug Yeager, and Stanislav Y Emelianov. Biomedical Applications of Photoacoustic Imaging with Exogenous Contrast Agents. *Annals of Biomedical Engineering*, 40(2):422–437, 2012.

[31] Janek Gröhl, Thomas Kirchner, Tim J Adler, Lina Hacker, Niklas Holzwarth, AdriÃ¡n Hernández-Aguilera, Mildred A Herrera, Edgar Santos, Sarah E Bohndiek, and Lena Maier-Hein. Learned spectral decoloring enables photoacoustic oximetry. *Scientific Reports*, 11(1):6565, 2021.

[32] Roman Hochuli, Lu An, Paul C Beard, and Benjamin T Cox. Estimating blood oxygenation from photoacoustic images: can a simple linear spectroscopic inversion ever work? *Journal of biomedical optics*, 24(12):1–13, 12 2019.

[33] Geoffrey P. Luke, Kevin Hoffer-Hawlik, Austin C. Van Namen, and Ruibo Shang. O-Net: A Convolutional Neural Network for Quantitative Photoacoustic Image Segmentation and Oximetry. 11 2019.

[34] Deepit Abhishek Durairaj, Sumit Agrawal, Kerrick Johnstonbaugh, Haoyang Chen, Sri Phani Krishna Karri, and Sri-Rajasekhar Kothapalli. Unsupervised deep learning approach for photoacoustic spectral unmixing. In *Proc.SPIE*, volume 11240, 2 2020.

[35] Joseph A Knowles, Cara H Heath, Reshu Saini, Heidi Umphrey, Jason Warram, Kenneth Hoyt, and Eben L Rosenthal. Molecular targeting of ultrasonographic contrast agent for detection of head and neck squamous cell carcinoma. *Archives of otolaryngology–head & neck surgery*, 138(7):662–668, 7 2012.

[36] Peter Frinking, Tim Segers, Ying Luan, and FranÃ§ois Tranquart. Three Decades of Ultrasound Contrast Agents: A Review of the Past, Present and Future Improvements. *Ultrasound in Medicine & Biology*, 46(4):892–908, 2020.

[37] Cristina Dudau, Shema Hameed, Daren Gibson, Senthil Muthu, Ann Sandison, Rob J Eckersley, Peter Clarke, David O Cosgrove, and Adrian K Lim. Can contrast-enhanced ultrasound distinguish malignant from reactive lymph nodes in patients with head and neck cancers? *Ultrasound in medicine & biology*, 40(4):747–754, 4 2014.

[38] Stuart Ibsen, Carolyn E Schutt, and Sadik Esener. Microbubble-mediated ultrasound therapy: a review of its potential in cancer treatment. *Drug design, development and therapy*, 7:375–388, 5 2013.

[39] Ai-Ho Liao, Wan-Ting Lin, Hang-Kang Chen, Cheng-Ping Shih, Chih-Hung Wang, and Yueng-Hsiang Chu. Synergistic effects of combined treatment with ultrasound-mediated cisplatin-loaded microbubbles and atorvastatin on head and neck cancer. *Head & neck*, 43(1):15–26, 1 2021.

[40] Samantha M Fix, Mark A Borden, and Paul A Dayton. Therapeutic gas delivery via microbubbles and liposomes. *Journal of Controlled Release*, 209:139–149, 2015.

[41] Natalya Rapoport. Phase-shift, stimuli-responsive perfluorocarbon nanodroplets for drug delivery to cancer. *Wiley Interdisciplinary Reviews: Nanomedicine and Nanobiotechnology*, 4(5):492–510, 9 2012.

[42] Shu-Guang Zheng, Hui-Xiong Xu, and Hang-Rong Chen. Nano/microparticles and ultrasound contrast agents. *World journal of radiology*, 5(12):468–471, 12 2013.

[43] Natalya Rapoport, Kweon-Ho Nam, Roohi Gupta, Zhongao Gao, Praveena Mohan, Allison Payne, Nick Todd, Xin Liu, Taeho Kim, Jill Shea, Courtney Scaife, Dennis L Parker, Eun-Kee Jeong, and Anne M Kennedy. Ultrasound-mediated tumor imaging and nanotherapy using drug loaded, block copolymer stabilized perfluorocarbon nanoemulsions. *Journal of Controlled Release*, 153(1):4–15, 2011.

[44] Kristina A. Hallam and Stanislav Y. Emelianov. Toward optimization of blood brain barrier opening induced by laser-activated perfluorocarbon nanodroplets. *Biomedical Optics Express*, 10(7):3139, 7 2019.

[45] Cherry C Chen, Paul S Sheeran, Shih-Ying Wu, Oluyemi O Olumolade, Paul A Dayton, and Elisa E Konofagou. Targeted drug delivery with focused ultrasound-induced blood-brain barrier opening using acoustically-activated nanodroplets. *Journal of Controlled Release*, 172(3):795–804, 2013.

[46] Geoffrey P Luke, Alexander S Hannah, and Stanislav Y Emelianov. Super-Resolution Ultrasound Imaging in Vivo with Transient Laser-Activated Nanodroplets. *Nano Letters*, 16(4):2556–2559, 4 2016.

[47] Alexander Hannah, Geoffrey Luke, Katheryne Wilson, Kimberly Homan, and Stanislav Emelianov. Indocyanine Green-Loaded Photoacoustic Nanodroplets: Dual Contrast Nanoconstructs for Enhanced Photoacoustic and Ultrasound Imaging. *ACS Nano*, 8(1):250–259, 1 2014.

[48] Marvin Xavierselvan, Jason Cook, Jeanne Duong, Nashielli Diaz, Kimberly Homan, and Srivalleesha Mallidi. Photoacoustic nanodroplets for oxygen enhanced photodynamic therapy of cancer. *Photoacoustics*, 25:100306, 2022.

[49] Alexander Graham Bell. On the production and reproduction of sound by light. *American Journal of Science*, s3-20(118):305 LP – 324, 10 1880.

[50] Keerthi S Valluru and Juergen K Willmann. Clinical photoacoustic imaging of cancer. *Ultrasonography (Seoul, Korea)*, 35(4):267–280, 10 2016.

[51] Da-Kang Yao, Chi Zhang, Konstantin Maslov, and Lihong V Wang. Photoacoustic measurement of the Grüneisen parameter of tissue. *Journal of biomedical optics*, 19(1):17007, 1 2014.

[52] Chao Sun, Stephen D Pye, Jacinta E Browne, Anna Janeczko, Bill Ellis, Mairead B Butler, Vassilis Sboros, Adrian J W Thomson, Mark P Brewin, Charles H Earnshaw, and Carmel M Moran. The Speed of Sound and Attenuation of an IEC Agar-Based

Tissue-Mimicking Material for High Frequency Ultrasound Applications. *Ultrasound in Medicine & Biology*, 38(7):1262–1270, 2012.

[53] Geoffrey P Luke, Seung Yun Nam, and Stanislav Y Emelianov. Optical wavelength selection for improved spectroscopic photoacoustic imaging. *Photoacoustics*, 1(2):36–42, 2013.

[54] Mucong Li, Yuqi Tang, and Junjie Yao. Photoacoustic tomography of blood oxygenation: A mini review. *Photoacoustics*, 10:65–73, 5 2018.

[55] Judith Weber, Paul C Beard, and Sarah E Bohndiek. Contrast agents for molecular photoacoustic imaging. *Nature Methods*, 13(8):639–650, 2016.

[56] Takuro Niidome, Masato Yamagata, Yuri Okamoto, Yasuyuki Akiyama, Hironobu Takahashi, Takahito Kawano, Yoshiki Katayama, and Yasuro Niidome. PEG-modified gold nanorods with a stealth character for in vivo applications. *Journal of controlled release : official journal of the Controlled Release Society*, 114(3):343–347, 9 2006.

[57] Katheryne Wilson, Kimberly Homan, and Stanislav Emelianov. Biomedical photoacoustics beyond thermal expansion using triggered nanodroplet vaporization for contrast-enhanced imaging. *Nature Communications*, 3(1):618, 2012.

[58] Heechul Yoon. Ultrasound and Photoacoustic Imaging of Laser-Activated Phase-Change Perfluorocarbon Nanodroplets, 2021.

[59] Alexander S Hannah, Geoffrey P Luke, and Stanislav Y Emelianov. Blinking Phase-Change Nanocapsules Enable Background-Free Ultrasound Imaging., 2016.

[60] Heechul Yoon, Steven K Yarmoska, Alexander S Hannah, Changhan Yoon, Kristina A Hallam, and Stanislav Y Emelianov. Contrast-enhanced ultrasound imaging in vivo with laser-activated nanodroplets. *Medical physics*, 44(7):3444–3449, 7 2017.

[61] Benjamin T Cox, Jan G Laufer, Paul C Beard, and Simon R Arridge. Quantitative spectroscopic photoacoustic imaging: a review. *Journal of Biomedical Optics*, 17(6):1–23, 6 2012.

[62] Ivan Olefir, Stratis Tzoumas, Hong Yang, and Vasilis Ntziachristos. A Bayesian Approach to Eigenspectra Optoacoustic Tomography. *IEEE transactions on medical imaging*, 37(9):2070–2079, 2018.

[63] Stratis Tzoumas, Antonio Nunes, Ivan Olefir, Stefan Stangl, Panagiotis Symvoulidis, Sarah Glasl, Christine Bayer, Gabriele Multhoff, and Vasilis Ntziachristos. Eigenspectra optoacoustic tomography achieves quantitative blood oxygenation imaging deep in tissues. *Nature Communications*, 7(1):12121, 2016.

[64] Thomas Kirchner, Janek Gröhl, and Lena Maier-Hein. Context encoding enables machine learning-based quantitative photoacoustics. *Journal of Biomedical Optics*, 23(5):1–9, 5 2018.

[65] Chuangjian Cai, Kexin Deng, Cheng Ma, and Jianwen Luo. End-to-end deep neural network for optical inversion in quantitative photoacoustic imaging. *Optics Letters*, 43(12):2752–2755, 2018.

[66] Janek Gröhl, Melanie Schellenberg, Kris Dreher, and Lena Maier-Hein. Deep learning for biomedical photoacoustic imaging: A review. *Photoacoustics*, 22:100241, 2 2021.

[67] Steven L Jacques. Coupling 3D Monte Carlo light transport in optically heterogeneous tissues to photoacoustic signal generation. *Photoacoustics*, 2(4):137–142, 2014.

[68] Steven L Jacques. Optical properties of biological tissues: a review. *Physics in Medicine and Biology*, 58(11):R37–R61, 2013.

[69] Olaf Ronneberger, Philipp Fischer, and Thomas Brox. U-Net: Convolutional Networks for Biomedical Image Segmentation BT - Medical Image Computing and Computer-Assisted Intervention â MICCAI 2015. pages 234–241, Cham, 2015. Springer International Publishing.

[70] Hengrong Lan, Daohuai Jiang, Changchun Yang, Feng Gao, and Fei Gao. Y-Net: Hybrid deep learning image reconstruction for photoacoustic tomography in vivo. *Photoacoustics*, 20:100197, 2020.

[71] Ruibo Shang, Richard Archibald, Anne Gelb, and Geoffrey P Luke. Sparsity-based photoacoustic image reconstruction with a linear array transducer and direct measurement of the forward model. *Journal of Biomedical Optics*, 24(3):1–9, 12 2018.

[72] Ryan Gessner and Paul A Dayton. Advances in molecular imaging with ultrasound. *Molecular imaging*, 9(3):117–127, 6 2010.

[73] Katherine Ferrara, Rachel Pollard, and Mark Borden. Ultrasound Microbubble Contrast Agents: Fundamentals and Application to Gene and Drug Delivery. *Annual Review of Biomedical Engineering*, 9(1):415–447, 7 2007.

[74] Kenneth B Bader, Guillaume Bouchoux, and Christy K Holland. Sonothrombolysis. *Advances in experimental medicine and biology*, 880:339–362, 2016.

[75] Ching-Hsiang Fan, Chien-Yu Ting, Hao-Li Liu, Chiung-Yin Huang, Han-Yi Hsieh, Tzu-Chen Yen, Kuo-Chen Wei, and Chih-Kuang Yeh. Antiangiogenic-targeting drug-loaded microbubbles combined with focused ultrasound for glioma treatment. *Biomaterials*, 34(8):2142–2155, 2013.

[76] Lotfi Abou-Elkacem, Sunitha V Bachawal, and JÃ¼rgen K Willmann. Ultrasound molecular imaging: Moving toward clinical translation. *European journal of radiology*, 84(9):1685–1693, 9 2015.

[77] Sibylle Pochon, Isabelle Tardy, Philippe Bussat, Thierry Bettinger, Jean Brochot, Mathew von Wronski, Lisa Passantino, and Michel Schneider. BR55: A Lipopeptide-Based VEGFR2-Targeted Ultrasound Contrast Agent for Molecular Imaging of Angiogenesis. *Investigative Radiology*, 45(2), 2010.

[78] Paul S Sheeran, Naomi Matsuura, Mark A Borden, Ross Williams, Terry O Matsunaga, Peter N Burns, and Paul A Dayton. Methods of Generating Submicrometer Phase-Shift Perfluorocarbon Droplets for Applications in Medical Ultrasonography. *IEEE transactions on ultrasonics, ferroelectrics, and frequency control*, 64(1):252–263, 1 2017.

[79] Paul S Sheeran and Paul A Dayton. Phase-change contrast agents for imaging and therapy. *Current pharmaceutical design*, 18(15):2152–2165, 2012.

[80] Catalina-Paula Spatarelu, Austin Van Namen, and Geoffrey P Luke. Optically Activatable Double-Drug-Loaded Perfluorocarbon Nanodroplets for On-Demand Image-Guided Drug Delivery. *ACS Applied Nano Materials*, 4(8):8026–8038, 8 2021.

[81] Yang Cao, Yuli Chen, Tao Yu, Yuan Guo, Fengqiu Liu, Yuanzhi Yao, Pan Li, Dong Wang, Zhigang Wang, Yu Chen, and Haitao Ran. Drug release from phase-changeable nanodroplets triggered by low-intensity focused ultrasound. *Theranostics*, 8(5):1327–1339, 2018.

[82] Kristina A Hallam, Eleanor M Donnelly, Andrei B Karpiouk, Robin K Hartman, and Stanislav Y Emelianov. Laser-activated perfluorocarbon nanodroplets: a new tool for blood brain barrier opening. *Biomedical Optics Express*, 9(9):4527–4538, 2018.

[83] Shin-Ichi Oikawa, Kiyoto Shiga, Daisuke Saito, Katsunori Katagiri, Aya Ikeda, Kodai Tuchida, Jun Miyaguchi, Kazuyuki Ishida, and Tamotsu Sugai. Association between contrast-enhanced ultrasonography and histopathological findings of the metastatic lymph nodes of patients with head and neck cancer: A preliminary study. *Oncology letters*, 15(4):4171–4176, 4 2018.

[84] Keshi Li, Yahui Liu, Shengmin Zhang, Youfeng Xu, Jianshuai Jiang, Fengying Yin, Yue Hu, Baosan Han, Shuxiong Ge, Li Zhang, and Yong Wang. Folate receptor-targeted ultrasonic PFOB nanoparticles: Synthesis, characterization and application in tumor-targeted imaging. *Int J Mol Med*, 39(6):1505–1515, 2017.

[85] J Liu, T Shang, F Wang, Y Cao, L Hao, J Ren, H Ran, Z Wang, P Li, and Z Du. Low-intensity focused ultrasound (LIFU)-induced acoustic droplet vaporization in phase-transition perfluoropentane nanodroplets modified by folate for ultrasound molecular imaging. *International Journal of Nanomedicine*, 12:911–923, 2017.

[86] Di Gao, Jinbiao Gao, Ming Xu, Zhong Cao, Luyao Zhou, Yingqin Li, Xiaoyan Xie, Qing Jiang, Wei Wang, and Jie Liu. Targeted Ultrasound-Triggered Phase Transition Nanodroplets for Her2-Overexpressing Breast Cancer Diagnosis and Gene Transfection. *Molecular Pharmaceutics*, 14(4):984–998, 4 2017.

[87] A V Namen, S Jandhyala, T Jordan, and G P Luke. Repeated Acoustic Vaporization of Perfluorohexane Nanodroplets for Contrast-Enhanced Ultrasound Imaging. *IEEE Transactions on Ultrasonics, Ferroelectrics, and Frequency Control*, 68(12):3497–3506, 2021.

[88] S Kumar, J Aaron, and K Sokolov. Directional conjugation of antibodies to nanoparticles for synthesis of multiplexed optical contrast agents with both delivery and targeting moieties. *Nature Protocols*, 3(2):314–320, 2008.

[89] Tomas Jordan, Mikaela A OâBrien, Catalina-Paula Spatarelu, and Geoffrey P Luke. Antibody-Conjugated Barium Titanate Nanoparticles for Cell-Specific Targeting. *ACS Applied Nano Materials*, 3(3):2636–2646, 3 2020.

[90] Min Joo Choi, Sitaramanjaneya Reddy Guntur, Kang I L Lee, Dong Guk Paeng, and Andrew Coleman. A Tissue Mimicking Polyacrylamide Hydrogel Phantom for Visualizing Thermal Lesions Generated by High Intensity Focused Ultrasound. *Ultrasound in Medicine & Biology*, 39(3):439–448, 2013.

[91] Rei Asami, Teiichiro Ikeda, Takashi Azuma, Shinichiro Umemura, and Kenichi Kawabata. Acoustic Signal Characterization of Phase Change Nanodroplets in Tissue-Mimicking Phantom Gels. *Japanese Journal of Applied Physics*, 49(7):07HF16, 2010.

[92] Cyril Lafon, Vesna Zderic, Misty L Noble, Jonathan C Yuen, Peter J Kaczkowski, Oleg A Sapozhnikov, Francoise Chavrier, Lawrence A Crum, and Shahram Vaezy. Gel phantom for use in high-intensity focused ultrasound dosimetry. *Ultrasound in Medicine & Biology*, 31(10):1383–1389, 2005.

[93] Jaesok Yu, Xucai Chen, Flordeliza S Villanueva, and Kang Kim. Vaporization and recondensation dynamics of indocyanine green-loaded perfluoropentane droplets irradiated by a short pulse laser. *Applied Physics Letters*, 109(24):243701, 12 2016.

[94] Danli Sheng, Liming Deng, Pan Li, Zhigang Wang, and Qunxia Zhang. Perfluorocarbon Nanodroplets with Deep Tumor Penetration and Controlled Drug Delivery for Ultrasound/Fluorescence Imaging Guided Breast Cancer Therapy. *ACS Biomaterials Science & Engineering*, 7(2):605–616, 2 2021.

[95] Lu Zhang, Tinghui Yin, Bo Li, Rongqin Zheng, Chen Qiu, Kit S Lam, Qi Zhang, and Xintao Shuai. Size-Modulable Nanoprobe for High-Performance Ultrasound Imaging and Drug Delivery against Cancer. *ACS Nano*, 12(4):3449–3460, 4 2018.

[96] Daniela Y Santiesteban, Kristina A Hallam, Steven K Yarmoska, and Stanislav Y Emelianov. Color-coded perfluorocarbon nanodroplets for multiplexed ultrasound and photoacoustic imaging. *Nano Research*, 12(4):741–747, 2019.

[97] Chengyue Li, Xiaochun Xu, Nathan McMahon, Omar Alhaj Ibrahim, Husain A Sattar, and Kenneth M Tichauer. Paired-Agent Fluorescence Molecular Imaging of Sentinel Lymph Nodes Using Indocyanine Green as a Control Agent for Antibody-Based Targeted Agents. *Contrast Media & Molecular Imaging*, 2019:7561862, 2019.

[98] Chengyue Li, Veronica C Torres, and Kenneth M Tichauer. Noninvasive detection of cancer spread to lymph nodes: A review of molecular imaging principles and protocols. *Journal of Surgical Oncology*, 118(2):301–314, 8 2018.

[99] Kimberley S Samkoe, Yeonjae Park, Kayla Marra, Eunice Y Chen, and Kenneth M Tichauer. Paired-agent imaging for detection of head and neck cancers. In *Proc.SPIE*, volume 10853, 2 2019.

[100] Naoki Nishio, Nynke S van den Berg, Brock A Martin, Stan van Keulen, Shayan Fakurnejad, Eben L Rosenthal, and Katheryne E Wilson. Photoacoustic Molecular Imaging for the Identification of Lymph Node Metastasis in Head and Neck Cancer Using an Anti-EGFR AntibodyâDye Conjugate. *Journal of Nuclear Medicine*, 62(5):648 LP – 655, 5 2021.

[101] Steven K Yarmoska, Heechul Yoon, and Stanislav Y Emelianov. Lipid Shell Composition Plays a Critical Role in the Stable Size Reduction of Perfluorocarbon Nanodroplets. *Ultrasound in medicine & biology*, 45(6):1489–1499, 6 2019.